Gerald Schwarz

Comparison of advanced MR Reconstruction Methods for Non-Contrast-Enhanced MR Angiography

Diploma Thesis

Graz University of Technology

Institute for Medical Engineering

Head: Univ.-Prof., Dipl-Ing., Dr.techn. Stollberger Rudolf

Supervisor: Univ.-Prof., Dipl-Ing., Dr.techn. Stollberger Rudolf

Graz, March 2015

Statutory Declaration

I declare that I have authored this thesis independently, that I have not used other than the declared sources/resources, and that I have explicitly marked all material which has been quoted either literally or by content from the used sources.

Graz, _____ _____

Date Signature

Eidesstattliche Erklärung[1]

Ich erkläre an Eides statt, dass ich die vorliegende Arbeit selbstständig verfasst, andere als die angegebenen Quellen/Hilfsmittel nicht benutzt, und die den benutzten Quellen wörtlich und inhaltlich entnommenen Stellen als solche kenntlich gemacht habe.

Graz, am _____ _____

Datum Unterschrift

[1] Beschluss der Curricula-Kommission für Bachelor-, Master- und Diplomstudien vom 10.11.2008; Genehmigung des Senates am 1.12.2008

Abstract

The concept of MRA summarizes many different techniques that enable the in-vivo depiction of the human vessels without the use of ionizing radiation. Dependent on the delivery of a contrast agent it can further be divided into CE-MRA and NCE-MRA. The major advantage of NCE-MRA is that there is no need for an invasive application of the intra-arterial contrast agent, with the drawback of prolonged acquisition times.

The goal of this work is to evaluate the applicability of advanced MR image reconstruction methods that allow for accelerated data acquisition. A total of four reconstruction methods combined with two undersampling schemes were tested and the specific limitations were described.

To this end selected NCE-MRA techniques for different anatomical regions were adjusted on a 3T MR system to acquire reference data on which retrospective simulation of acceleration was performed.

This work compares two methods of undersampling with four image reconstruction methods on the data of the four different selected NCE-MRA techniques and shows the limitations of the imaging methods and the advanced image reconstruction techniques.

Keywords: NCE-MRA imaging methods, advanced image reconstruction, retrospective undersampling, applicability evaluation

Contents

Abbreviations

MRA	Magnetic-Resonance-Angiography
CE-MRA	Contrast-Enhanced-Magnetic-Resonance-Angiography
NCE-MRA	Non-Contrast-Enhanced-Magnetic-Resonance-Angiography
MRI	Magnetic-Resonance-Imaging
DSA	Digital Subtraction Angiography
CT	Computed Tomography
TV	Total Variation
TGV	Total Generalized Variation
TOF	Time of Flight
QISS	Quiescent interval single shot
TSE	Turbo-spin-echo
FOV	Field of view
bSSFP	balanced Steady-State Free Precision
PC-MRA (PCA)	Phase contrast MRA
FSD	Flow-sensitive-dephasing
ASL	Arterial spin labeling
FID	Free induction decay

RARE	Rapid acquisition with relaxation enhancement
MOTSA	Multiple overlapping thin slab acquisition
TONE	Tilted optimized nonsaturating excitation
ECG	Electrocardiogram
ACS	Auto calibration-signal
IRGN	Iterative-regularized Gauss-Newton
MIP	Maximum intensity projection

List of Figures

List of Figures

1 Introduction

In the last ten years many Non-Contrast-Enhanced Magnetic Resonance Angiography (NCE-MRA) techniques were developed and implemented on clinical Magnetic Resonance (MR) scanners. In contrast to currently clinically used angiographic techniques using X-ray, such as Digital Subtraction Angiography (DSA) and Computed Tomography (CT), all MRI techniques use non ionizing radiation and are therefore applicable with minor health risks.

In addition all X-ray techniques require a contrast agent to generate sufficient contrast in image acquisition. While the use of DSA for immediate treatment of acute vessel occlusion is reasonable for , for all non acute vessel stenosis it is not. For a specific group of patients suffering from renal diseases, the risk of all imaging techniques using contrast agents bear the risk of worsening the disease by putting additional stress on the kidneys.

This leads to a favorable application of NCE-MRA on patients with renal diseases. The drawback of NCE-MRA techniques is to have a rather long acquisition time compared to all other angiographic imaging techniques. Therefore the challenge is to develop methods to accelerate measurements in order to enhance patient comfort to enable more patients to take this

examination.
For the means of accelerated measurements reconstruction techniques were developed that recover missing data after the measurement by applying advanced mathematical methods. The currently applied acceleration and data recovering methods in the clinic are GRAPPA [1] and SENSE [2], which use the properties of the data space, so called k-space, to recover missing data points using linear reconstruction methods and the additional information given by multiple receive coils (Parallel Imaging). These methods are used conservatively in clinical routine, also due to locally reduced SNR.
With the definition of the reconstruction process as an inverse problem which allows to introduce prior knowledge, a new and promising field of methods is currently worked on and consequently developed. This methods use nonlinear inversion and image based constraints, for example Tikhonov, Total Variation (TV) and higher order TGV constraints [3, 4], to reconstruct strongly accelerated MRI acquisitions.

1.1 Aim of this work

The aim of this work is to apply newly developed image reconstruction strategies that enable accelerated acquisition of NCE-MRA methods. This is achieved by measurement of fully sampled k-spaces of various NCE-MRA techniques and retrospective application of two acceleration techniques, known as undersampling, to the data. Afterwards, image reconstruction methods are applied to recover the missing data and evaluate the performance against the fully sampled *ground-truth*.

1.2 Content of this work

This work will give an overview of currently available NCE-MRA methods with more details on specifically selected modalities that were used in this work in (chapter 2). In chapter 3 the principles of image reconstruction and the advanced methods, which are used in this work, will be described.
In chapter 4 the complete work-flow used is described. This chapter is divided into two sections. The first section describes the measurement procedures used. The subsequent section describes the realized reconstruction pipeline with all features.
The results gained in this work are described and depicted in chapter 5.
In chapter 6 the gained results and limitations of this work are discussed and a outline for future work is drawn.

2 MRI Sequences

2.1 Introduction

This chapter summarizes current MRI techniques for angiography, starting with an overview of available methods in Magnetic-Resonance-Angiography (MRA). These can be distinguished in either temporally resolved, where the k-space is measured with a defined temporal resolution or not time-resolved. Here all data is measured at once or with the same temporal conditions, for example at the same state of the test persons cardiac state. The second distinguishing feature is determined by the use of a contrast agent. This class of MRA modality is called Contrast-Enhanced-Magnetic-Resonance-Angiography (CE-MRA) and the complementary class is termed Non-Contrast-Enhanced-Magnetic-Resonance-Angiography (NCE-MRA). Subsequently an overview of current methods used in clinical application is given, followed by a description of the sequences used in this work, which are only a part of the available methods shown in next section. Finally, methods of physiological triggering used with NCE-MRA are described. The chapter finishes with specification of measurements regarding combinations

of the previous described methods and site of application within the human body. This chapter describes only the used encoding methods, while the underlying physical principles of MRI-signal generation are described in [5, 6].

2.2 Current methods of Non-Contrast-Enhanced Magnetic Resonance Angiography

This part is based on the detailed summary of techniques in MRA by Wheaton et al. [7]. The sequences are sub-grouped in inflow based sequences, cardiac-phase depended methods, flow-encoding techniques, spin-labeling procedures and relaxation-based sequences. In the subsequent subsections each group of methods is explained and the their field of application in MRA as well as details on sequence design.

2.2.1 Inflow-based methods

The inflow-based methods were the first sequences to be developed and are known as Time-of-Flight (TOF) methods. This effect is created by the different excitation of stationary tissue in contrary to spins in moving blood. The reenacted exposure to saturation pulses for the imaging slab/slice saturates the spins of the stationary tissue in order to reduce the longitudinal magnetization to a reduced steady-state level, approximately to zero. These spin ensembles provide low image signal intensity, in contrary to the inflowing blood from non-saturated regions with full magnetization, which supply

high signal-intensity.
Therefore the effect is dependent of exchange of saturated blood with non-saturated blood. The replacement of blood relies on the velocity of blood flow, the repetition time (TR) and the cross-sectional area of the vessel. In case the saturated blood is not fully replaced by non-saturated blood, the volume is partially saturated and the signal of this space is dependent on the excitation flip angle and the T1 value of blood.
The sequences used to exploit this effect for the imaging of intracranial arteries are termed 3D-TOF and HOP-MRA, where the latter is an extension where two separate echos are reconstructed, a bright-blood image for fast flowing blood and a dark-blood image depicting the slow flow in the small arteries. The result is reconstructed by the difference of the two images.
Another technique used is quiescent interval single-shot (QISS). This sequence uses a presaturation RF pulse to saturate the static tissue in the FOV. After an interval, the freshly inflowing blood is recorded, using a fast 2D bSSFP sequence. The saturation is applied prior to the systole and imaging is done during diastole. Therefore the maximum inflow is achieved, example is shown in figure 2.1.

2.2.2 Cardiac-phase depended methods

This class of sequences relies on the differences between the physiological flow in arteries in systole and diastole. In the diastolic phase the flow velocity is slow ($10 - 20\ cm/s$), while in systolic phase the flow is considerably faster, $30 - 70\ cm/s$. However venous flow is almost constant and slow during

Figure 2.1. Exemplary result of a 3D-TOF sequence[7].

the cardiac cycle. With pulse sequences that are able to generate a signal sensitive to the described difference in flow velocity it is therefore possible to create a bright-artery image during diastole, when the slow blood flow does not dephase the spins sufficiently, so that the spins constitute a bright signal. A dark-artery image is acquired during systole, due to substantially dephasing of the fast blood flow. The dark-artery image sets are subtracted from the bright-artery image set to remove the static background and compute the angiogram.

One method is termed cardiac-gated 3D-Turbo-Spin-Echo. Here the gating

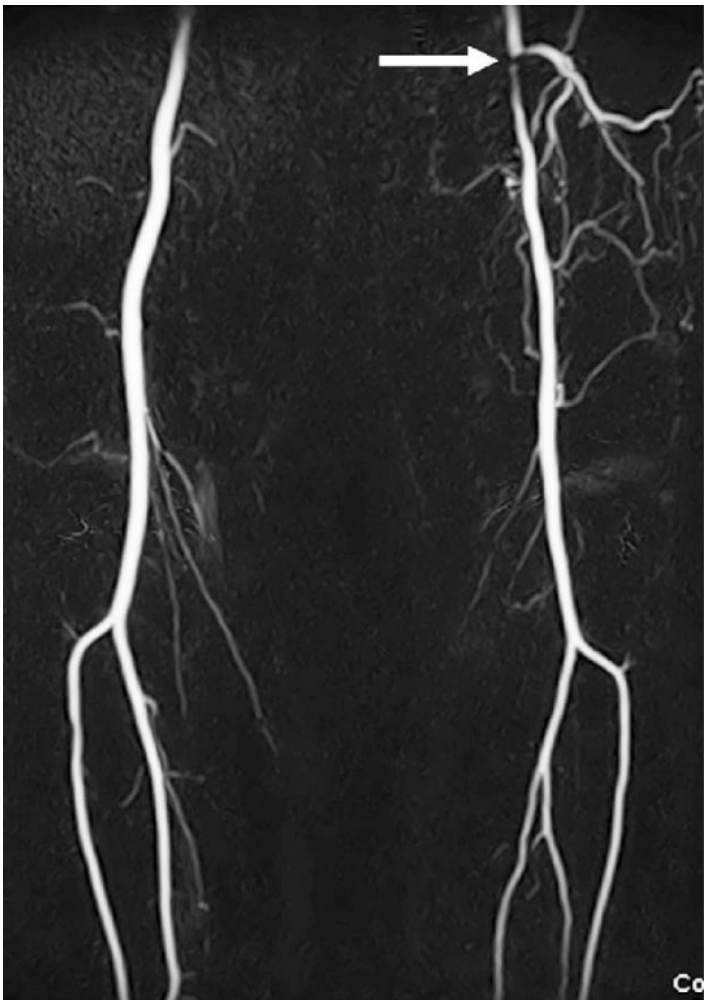

Figure 2.2. Exemplary result of a cardiac-gated 3D-TSE sequence [7].

is accomplished with the electrocardiogram or peripheral pulse signals, though individual trigger delays have to be calibrated for each patient to determine the ideal diastolic and systolic trigger times, an example is shown in figure 2.2.

2.2.3 Flow-encoding methods

Flow-encoding methods use the possibility of magnetic field gradients to encode motion or flow of spins. The spins moving in flow encoding direction of the gradient field, accumulate a phase proportional to their velocity. Bipolar gradients are commonly used for flow-encoding, and consist of two equal but opposite magnitude gradient lobes. These gradients induce a net zero phase for stationary spins in contrast to moving spins, which accumulate a net nonzero phase depending on amplitude, duration of the gradient lobes and their velocity. There are two types of sequences used.
The first is termed Phase Contrast MRA (PC-MRA). and employs the described bipolar gradients to create flow images. In contrast to many other methods, PC-MRA encodes the flow in phase and therefore phase images are reconstructed instead of magnitude images. To encode flow in one dimension two scans are needed. One with the flow-encoding bipolar gradients and one with flow-compensated gradient lobes. Subtracting the second of the first removes the background phase sufficiently. Stationary tissue is naturally suppressed in the final subtracted image due to the zero net phase of stationary tissue. An extension to three dimensional spatial encoding can be achieved by using the gradients in all three spatial directions. Even time-resolved 3D PC flow maps can be created with ECG gating, which yields the 4D PC-MRA.
The second class of sequences use flow-sensitive dephasing (FSD). FSD employs a combination of spin-echo technique, consisting of $90°$ $180°$ $-90°$-RF-pulse and bipolar gradient lobes for velocity dependent flow encoding.

This encoding step is referred as FSD module. The phase generated in flowing liquids by the bipolar gradient lobes is used for flow-dephasing instead of flow-encoding. The third RF-pulse flips the transverse magnetization in stationary tissue back to the longitudinal axis and the dephased spins in flowing liquids stay in the transverse plane and get further dephased by a trailing gradient.
The angiogram is calculated by subtracting the dark artery image from the bright artery image. The dark artery scan is obtained during systole using ECG gating with a considerably strong FSD module. The fast movement of the flowing spins during systole generates low arterial signal. The bright artery scan is obtained with no FSD module, resulting in a bright arterial signal. The subsequent readout is usually done using a flow-compensated bSSFP sequence.

2.2.4 Spin-labeling techniques

In general arterial spin-labeling techniques (ASL) use a form of selective inversion pulse to label the longitudinal magnetization of inflowing blood. The basic idea of ASL is that the longitudinal magnetization of inflowing blood differs from surrounding stationary tissue. After an inversion recovery period subsequently to the tagging, in which non-tagged blood flows into the imaging slab, the readout with a common sequence is done. Currently there are three methods available: Flow-in, flow-out and tag-alternation.
The flow-in method applies the tagging pulse to the whole imaging slab. Therefore the stationary tissue and the blood in the region of interest

are inverted. In the inversion recovery interval untagged blood enters the imaging volume, while the spins of stationary tissue and the previously existing blood are recovering to null magnetization. Consequently the slab is read out by a common fast readout sequence like bSSFP.
In the flow-out method, the tagging pulse is applied upstream of the vessel of interest. Just before the tagging pulse a nonselective inversion pulse is applied. First, the nonselective pulse inverts all longitudinal spins in stationary tissue and moving blood in the imaging volume. The second pulse restores the magnetization upstream of the imaging slab, without changing the magnetization of the stationary tissue, which stays inverted. In the inversion recovery interval the tagged blood flows from the tagging region into the imaging slab, while the magnetization of the spins in the imaging slab is recovering.
The concept of tag-alternation method requires to acquire two scans, one with spin-labeling enabled and a second without spin labeling. The tagging is applied upstream of the vessel of interest and for the final image the difference of both is calculated, which removes signal from background tissue and preexisting blood in the imaging volume and shows just the tagged spins, an example is shown in figure 2.3.

2.2.5 Relaxation-based techniques

The basis for relaxation-based techniques are the fundamental differences in relaxation properties between arterial, venous and neighboring stationary tissue. The T2 and T2* of arterial blood is longer than venous blood because

Figure 2.3. Exemplary result of a 3D-TrueFISP sequence [7].

of the increased oxygenation of hemoglobin in arteries. The high percentage of water in blood results in prolonged T1 than in adjoining stationary tissue. Therefore the arterial signal can be selectively outlined and stationary tissue and venous signal suppressed.

In order to improve background tissue suppression saturation regions, subtraction and inversion recovery methods can be used. Due to the independence of flow-velocity, vessel orientation and cardiac-cycle, these methods are referred to as flow-independent.

bSSFP sequences can be used as stand alone NCE-MRA due to the T2/T1-weighted contrast and the inherent flow-compensation. Therefore any blood

is depicted independent of its velocity, such that there is a considerable venous contamination, which can be suppressed with a T2-preparation pulse and an inversion recovery pulse. Additionally, as fat signal appears bright in bSSFP images, a form of fat suppression needs to be applied, in order enhance the background contrast of the image.
In this work four from the five promising sequences for NCE-MRA (FSD is excluded) are selected to be tested for applicability for subsampling and the reconstruction methods described in chapter 3. These four methods are cardiac-gated Turbospin-echo, 3D phase contrast, arterial spin labeling using a bSSFP readout and TOF. The following sections describe these four methods briefly.

2.3 Turbospin-Echo Sequence

This sequence is a modification of the spin echo (SE) sequence. The corresponding SE pulse diagram is shown in figure 2.4. After an initial excitation pulse of 90°, a second pulse of 180° delayed by $TE/2$ is applied. The second RF-pulse flips the dephased spins back, which rephase again afterwards. A frequency encoding gradient and a phase encoding gradient are applied just before the refocusing pulse to perform spatial encoding. The rephasing spins form an echo at the echo time TE after the excitation pulse, when the reapplied frequency encoding gradient compensated the prior gradient. This happens typically in the center of the readout gradient to avoid $T2^*$ weighting.
The two RF-pulses are mostly spatial selective in order to acquire at multi-

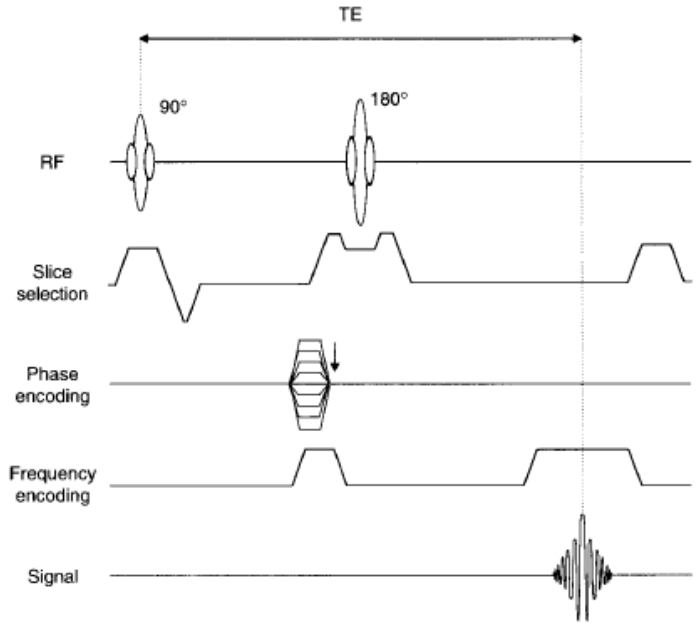

Figure 2.4. A single echo RF spin-echo pulse sequence. Crusher and spoiling gradients are indicated in the slice encoding direction. The arrow indicates different gradients for phase encoding throughout the whole acquisition of the k-space.

ple slice locations in one TR interval, using interleaving in phase encoding direction. The sequence also makes use of crusher and spoiling gradients. The crusher gradient in slice selection suppresses the FID of the 180° RF pulse and the trailing spoiler gradient dephases the remaining transverse magnetization sufficiently for the next excitation.

The further development of this basic sequence leads to the dual echo spin-echo. Here the idea is to refocus the first echo using a second 180° RF pulse, as displayed in figure 2.5. The second echo has less amplitude than the first due to the $T2$-decay, showing that the maximum echo amplitude is

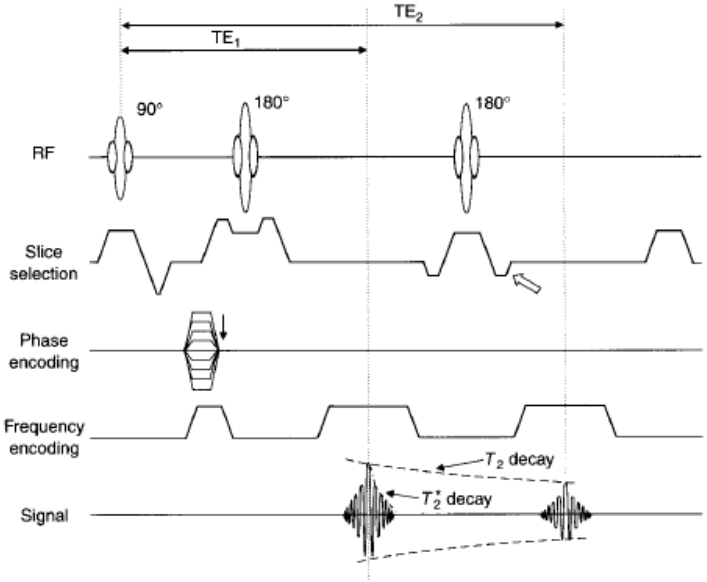

Figure 2.5. Dual echo RF spin-echo pulse sequence for variable echo acquisition. Second spin echo peaks at TE_2 and is reconstructed separately. To suppress a stimulated echo at the second 180° pulse, the amplitude of the second crusher gradient has to be different from the first set (hollow arrow).

limited by T_2-decay. The principle of multiple echoes is to encode multiple phase encoding lines in k-space in one T_R interval, using one echo per phase encoding line. This sequence is called turbo spin echo (TSE) sequence, also termed as rapid acquisition with relaxation enhancement (RARE) or fast spin echo (FSE).

The sequence starts with a slab selective 90° excitation pulse followed by a train of 180° refocusing pulses shown in figure 2.6. Identical readout gradient lobes are applied for every echo. Between excitation and the first refocusing pulse a prephasing gradient is applied to center the echo in the

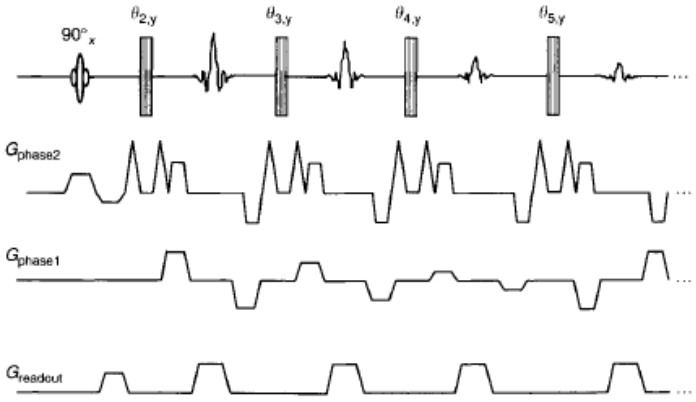

Figure 2.6. 3D TSE sequence diagram to image a volume excited with a slab selective 90°excitation. The refocusing pulses are not selective, although possible. Primary phase encoding (G_{phase1} or k_y) is achieved during the echo train and the second phase encoding (G_{phase_2} or k_z) is done conventionally, one step per T_R. Additionally, phase-rewinding is performed in the second phase-encoding step, analogous to the first encoding direction.

first readout. Prephasing for the sequential refocusing pulse is achieved with the second half of the readout gradient lobe. Phase-encoding is achieved by applying a phase-encoding gradient after every refocusing pulse just before the readout gradient lobe. After the echo and the readout gradient before the subsequently refocusing pulse, a phase-rewinding gradient is applied to ensure signal coherence. All phase-encoding and phase-rewinding gradients have typically the same duration but differ in amplitude, echo-encoding and in the sequence to acquire multiple phase-encoding lines. The phase-encoding in the second direction can be done in the conventional way by one encoding step per TR interval with the additional effort to sort the

alternating phase-encoding lines in the second phase-encoding direction.
To overcome this post processing an alternative encoding form is used, shown in figure 2.6. The gradient is expanded to use a phase-rewinding gradient lobe like in the encoding direction in order to return to the initial phase, though the amplitudes stay the same throughout one TR interval. The image shows the crusher gradients straddling each refocusing pulse separately for clarification [5]. This sequence design allows standard Fourier reconstruction of the acquired images. The speedup compared to normal SE is called turbo factor and the sequence used in this thesis has a turbo factor of 60 accelerating the measurement by factor 60.
The use of TSE in NCE-MRA was shown by [8]. The approach is to acquire two cardiac gated image slabs. The effect of fast flowing arterial blood to be imaged dark is known. Two images are acquired at two different levels of arterial flow, i.e. systolic and diastolic.
To improve depiction of small vessels a flow-spoiling gradient in readout direction is applied [9]. The additional gradient is considered to dephase the spins in smaller arteries with less flow velocity during systole substantially and has almost no effect on the slowly flowing blood during diastole. This improves the contrast of small arteries considerably, commercially available and termed as SIEMENS NATIVE SPACE.
In measurements using 3D TSE NCE-MRA the choice of the refocusing angle determines the type of arteries displayed [10]. A high flip angle ($+160°$) of the refocusing pulse constitutes a high signal in the bright artery scans and on the other hand refocus more signal of slow-flowing blood in dark artery scans. Therefore bright signal is achieved for main arteries in the

angiogram and poor signal in small arteries. Low flip angels ($< 120°$) create less signal in the main arteries of bright artery scans but smaller vessels are less affected due to the reduced flow velocity. Further the low flip angle emphasizes the flow spoiling effect of TSE, resulting in a darker arterial signal in dark artery scan.

2.4 Phase Contrast Angiography

PCA is a technique which depicts moving spins using flow-encoding magnetic gradient lobes. These gradients encode the velocity of moving spins in the volume of interest into the phase of the images. To encode the velocity linearly into the phase, bipolar gradients are used. The axis in which the gradients are applied determines the direction of flow-sensitivity. The bipolar gradient lobes can be applied to all three encoding axes, namely frequency-encoding, phase-encoding or slice-encoding axis. The gradient lobes can be accompanied by any readout sequence like gradient echo or others, as shown in figure 2.7.

Images acquired with MR and in particular gradient echo images incorporate various effects (e.g. B_0-inhomogeneity) adding phase to the desired one. To overcome all these effects, two sets of images are acquired with identical parameters besides the velocity-encoding gradient. The first set is one time flow-encoding active and the other time flow-compensation active. The image is reconstructed by calculating the complex difference of both images, leaving just the phase contribution by moving spins.

The toggling of the bipolar gradient leads to a first order moment change

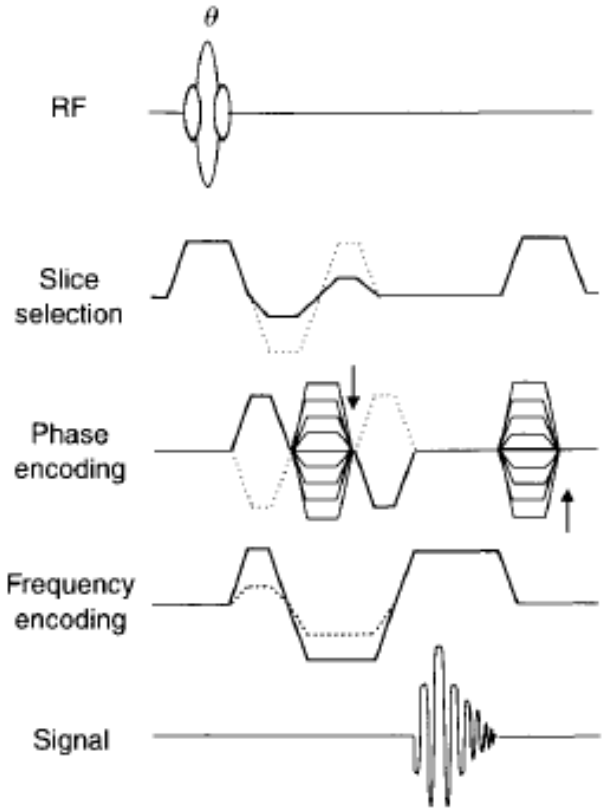

Figure 2.7. Basic PC sequence with a toggling bipolar gradient (dotted line) varying the first order moment m_1 to induce flow sensitivity along that axis, typically only one gradient per logical axis is used a time.

Δm_1, which defines the amount of velocity encoding. Therefore an additional parameter is necessary to be set prior to acquisition called aliasing velocity (VENC). This parameter is positive and inversely related to the first order moment change.

$$VENC = \frac{\pi}{|\gamma \, \Delta m_1|} \tag{2.1}$$

Units of VENC is typically stated in centimeters per second. The smaller the value of VENC, the higher the sensitivity to slower flow and vice versa. Therefore, if the VENC value is too small, flow aliasing artifacts occur and if it is too large the sensitivity is not sufficient, resulting in poor SNR in the final PC image.
The choice of VENC depends of the vessel of interest to image. Typical values can be found in table 2.1.

arterial peak flow velocities	
carotid arteries	$76cm/s$
vertebral arteries	$44cm/s$[11]
renal arteries	$80cm/s - 18cm/s$ [12]
femoral arteries	$50cm/s - 30cm/s$ [13]

Table 2.1. Overview of arterial flow velocities

Two reconstruction methods for phase contrast images are possible. Phase-difference reconstruction and complex-difference reconstruction. Phase-reconstruction is performed in image domain to specify the flow direction and the flow velocity. The phase difference of a pixel is defined by

$$\Delta\phi = \gamma\Delta m_1 v = \frac{v}{VENC}\pi \tag{2.2}$$

with the flow velocity v. Due to the range of phase-difference reconstruction is limited to $\pm\pi$ it is only possible to reconstruct flow direction with $|v| \leq VENC$, without using phase unwrapping methods. The phase differ-

ence of two pixels is calculated as:

$$\Delta\phi = \angle(Z_1 Z_2^*) = arg(Z_1 Z_2^*) = arctan\left(\frac{Im(Z_1 Z_2^*)}{Re(Z_1 Z_2^*)}\right) \tag{2.3}$$

using a 4-quadrant arctangent function.

Complex-difference reconstruction is performed by subtracting the data of the two acquisitions. For the final result a magnitude image is calculated. Due to linearity of the Fourier transform the difference can be calculated in k-space or image domain. Complex-difference in image-domain can be achieved by simply subtracting the values of the image on pixel-by-pixel basis, as shown in figure 2.8. Let Z_1 and Z_2 be the value of the complex value pixels of the reconstructed images of the two velocity-encoding gradients. The complex difference of a particular pixel can be written with

$$CD = |Z_1 - Z_2| = ||Z_1|e^{j\phi_1} - |Z_2|e^{j\phi_2}| \tag{2.4}$$

Applying the phase difference $\Delta\phi = \phi_1 - \phi_2$, $|e^{j\phi_2}| = 1$ and the law of cosines yields

$$CD = ||Z_1|e^{j\Delta\phi} - |Z_2|| = \sqrt{|Z_1|^2 + |Z_2|^2 - 2|Z_1||Z_2|\cos(\Delta\phi)} \tag{2.5}$$

It can further be assumed that the magnitude of the corresponding pixels are almost equal, $|Z_1| \approx |Z_2|$, which is often true. For the assumption $|Z_1| = |Z_2| = M$ and the trigonometric identity $1 - \cos(\Delta\phi) = 2\sin^2(x/2)$ equation 2.5 simplifies to

$$CD = \sqrt{2}M\sqrt{1 - \cos(\Delta\phi)} = 2M\left|sin\left(\frac{\Delta\phi}{2}\right)\right| \tag{2.6}$$

Using equation 2.1 the complex-difference yields

$$CD = 2M\left|\sin\left(\frac{\pi v}{2\mathrm{VENC}}\right)\right| \tag{2.7}$$

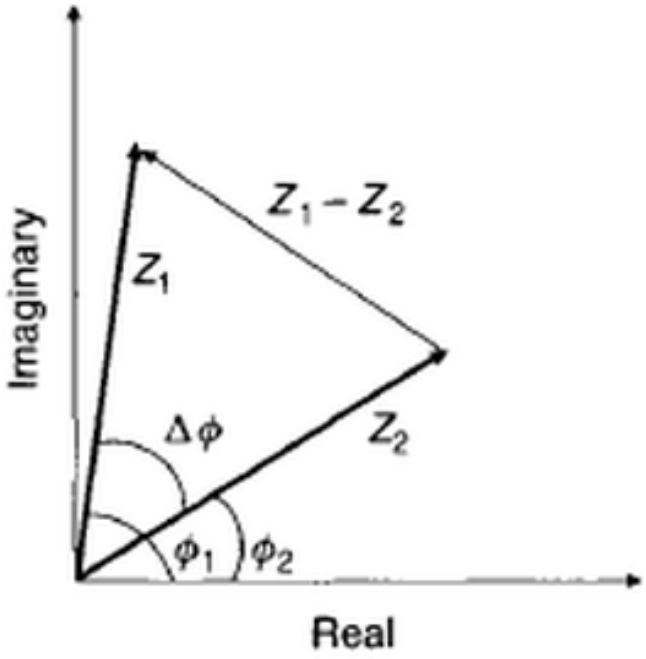

Figure 2.8. Diagram for the calculation of the complex difference in the final image. Z_1 and Z_2 are vector representations of the signals of one corresponding pair of one voxel in both images.

$$S = \sqrt{CD^2_{read} + CD^2_{ph-enc} + CD^2_{sl-enc}} \tag{2.8}$$

To achieve flow sensitivity a series of total four images needs to be acquired. One image is used as reference with flow-compensation scan while the other three encode the logical axes. The final images are calculated, determining the complex differences in each encoding axis and computing sum-of-squares of all (equation [5]).

2.5 Balanced Steady-State Free-Precision Sequence

In this chapter balanced Steady-State Free-Precision (bSSFP) sequence is specified, which is a further development of the SSFP sequence. SSFP

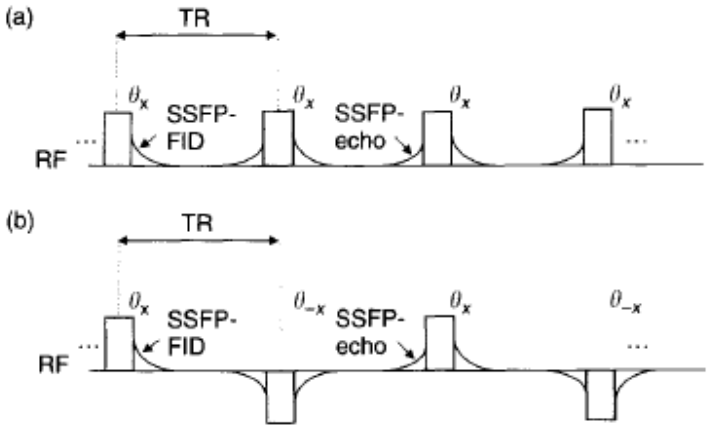

Figure 2.9. Schematic diagram of transverse steady-state of a standard RF-pulse train in (a) and a sign alternated pulse sequence in (b). The magnitude is not affected by the change of sign, but polarity. Any oscillations in FID or echo are not shown.

is a standard gradient echo sequence that produces greater signal than spoiled gradient echo, often at the cost of reduced contrast. The conditions to be met in order to achieve a steady state are as follows. First, all RF-pulses have to have the same phase in the rotating coordinate system (i.e. $\theta_x - T_R - \theta_x - T_R - \theta_x \ldots$) or a simple phase cycle, like sign alternation (i.e. $\theta_x - T_R - \theta_{-x} - T_R - \theta_x - T_R - \theta_{-x} \ldots$), referred to as phase coherent. Second, T_R needs to be less or in the range of T_2. Finally, the total

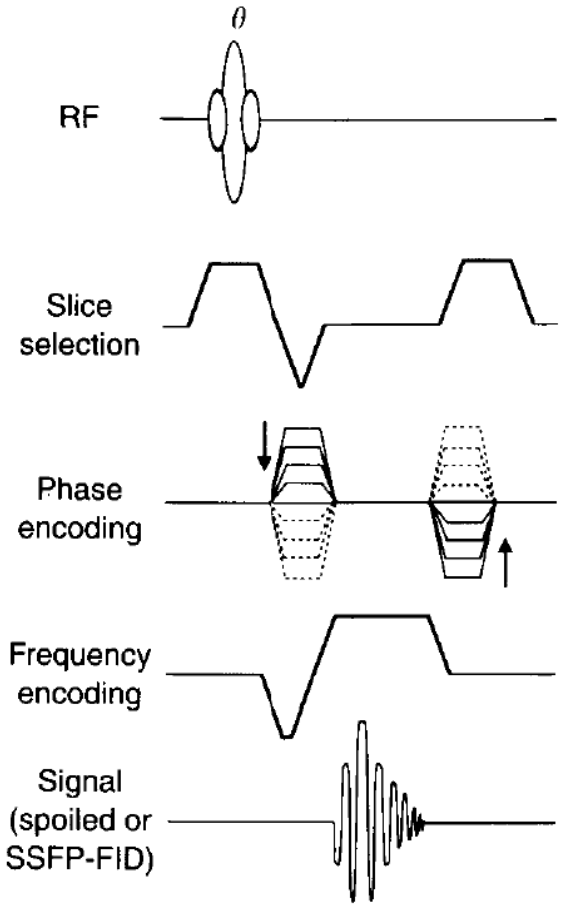

Figure 2.10. Pulse sequence used for SSFP acquisition or spoiled GRE acquisition

amount of accumulated phase of the transverse magnetization must be the same in every T_R to avoid spoiling of the steady state, which requires a phase-encoding-rewinder. When these conditions are met a steady-state for transversal and longitudinal magnetization is established, as displayed in figure 2.9. For sign alternation RF pulses the magnitude remains unchanged, but the signs are upended every TR interval (figure 2.9 b)). There occur two

detectable signals. A SSFP-echo forming just before every RF pulse and a SSFP-FID forming after every RF pulse. An actual SSFP pulse sequence is displayed in figure 2.10. For SSFP acquisitions the gradient areas on any

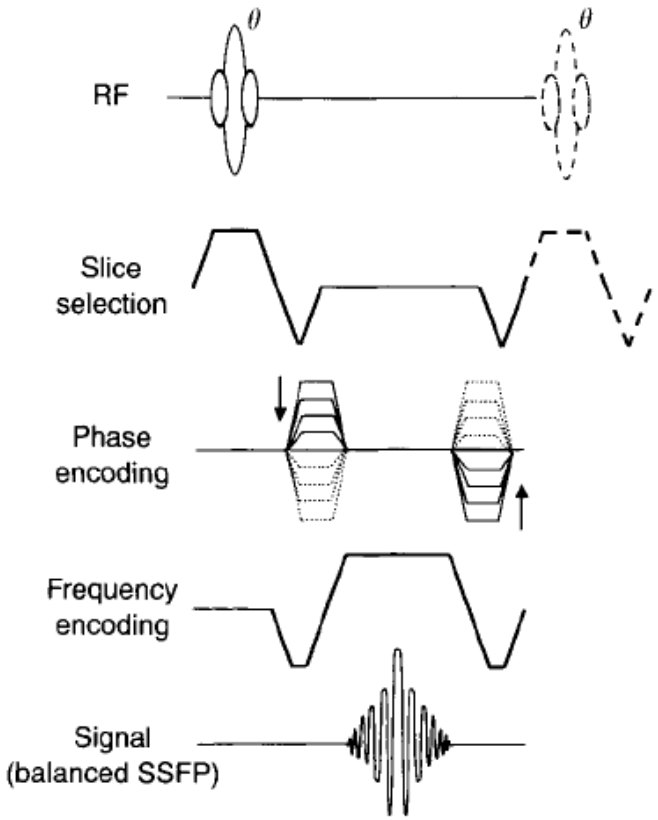

Figure 2.11. Pulse sequence used for bSSFP acquisition

axis must not differ over T_R intervals. With the introduction of an additional condition, that the net gradient areas on all axes must be zero a disparate steady-state occurs. Figure 2.11 shows RF-pulse train at steady-state. The peaks of SSFP-FID and SSFP-echo recombine simultaneously, resulting in

the rephasing at the same time TE. The final signal is the combination of two coherent signals. If the net gradients on every axis are non-zero the two SSFP-signals are non coherent and banding occurs [5].

2.6 Time-of-flight angiography

Time-of-flight (TOF) angiography is the standard method using inflow effects [5]. There are 2D-TOF methods in use that sequentially acquire a set of thin 2D Slices, without overlapping field-of-view (FOV) or with overlapping FOV. 3D-TOF acquires a bigger imaging volume than 2D-TOF with reuse of imaging gradients, which allow the use of weaker gradients. Multiple-overlapping-thin-slab-acquisition (MOTSA) is a sequential 3D-TOF method. It places multiple overlapping 3D slabs to increase SNR with the restriction of reduced amount of slices to acquire. Main disadvantage of MOTSA are slab boundary artifacts, which results in discontinuities of image sensitivity between adjacent image slabs.
TOF and CE-MRA share some common features. Both produce angiography images with a bright blood signal, both use similar pulse sequences, as a result of the demand for strongly T_1-weighted fast scans. Mostly used for acquisition are spoiled gradient echo sequences like spoiled FLASH, as displayed in figure 2.10 as well as SSFP-FID and bSSFP-echo. Spoiled sequences are preferred due to a better suppression of cerebrospinal and other fluids to be mistaken for blood.
Additionally a varying flip angle over the image slab is used. This ramp RF pulses or TONE pulses (tilted optimized nonsaturating excitation) have

a spatially varying flip angle profile ()shown in figure 2.12). It is used to equalize the signal generated by moving blood on its way through a thick slab of slices. If a constant flip angle is used the recently entered blood produces a stronger signal due to flow-related enhancement than the blood on the other of the slab. The exit-to-entrance flip-angle-ratio (for example $\alpha_{ext}/\alpha_{ent} = 40°/20° = 2$), is the ramp or TONE ratio, though by convention the nominal flip angle is the one on the center of the imaging slab (in this case $\alpha_{nom} = 30°$ for a linear ramp).

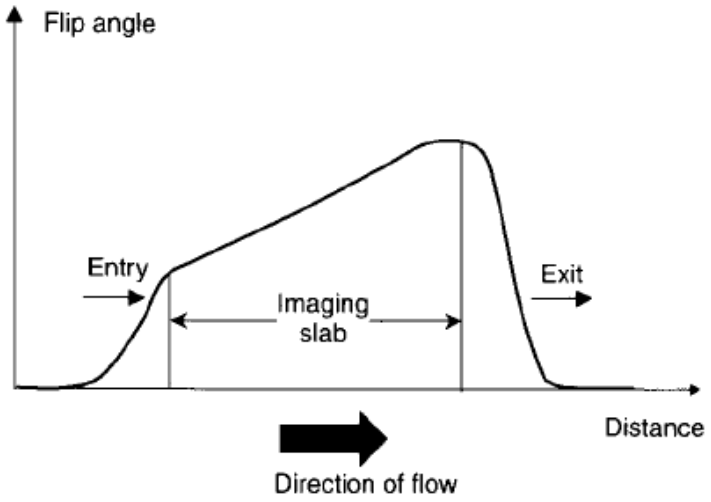

Figure 2.12. An example flip angle profile of a TONE pulse

2.7 Physiological Gating and Triggering

There are three possible methods of physiological gating and triggering for NCE-MRA: Cardiac triggering, respiratory navigators and respiratory

gating.

2.7.1 Cardiac triggering

The aim of cardiac triggering is to synchronize the sequence with the cardiac cycle of the patient, in order to reduce the artifacts arising from motion of the heart, vessels or the pulsatile flow of arteries. Ectrocardiograph monitors (ECG) are commonly used. The ECG is the surface measured voltage over time indicating the various parts of the electrical heart activity (figure 2.13). Each wave has an physiological background. The P wave shows the

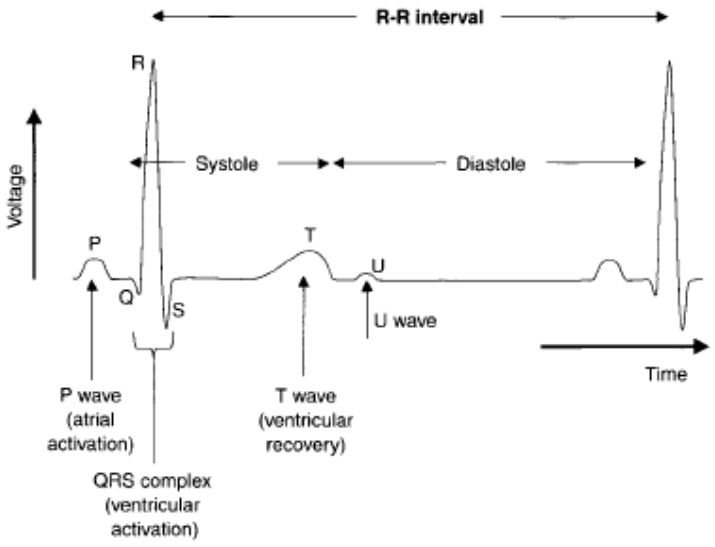

Figure 2.13. Schematic ECG waveform in one R-R-Interval

activation of the atria, coinciding with the contraction. The QRS-complex implies the activation of the ventricles and usually yields the strongest

peak in ECG. The recovery of the ventricles, referred to as repolarization, is implied by the T wave. The U wave is not detectable in every patient and interpreted as recovery of papillary muscles or the purkinje fibers [14]. The cycle can be split into two phases, the systolic phase and the diastolic phase. The systole refers to the ventricular contraction and the diastole corresponds to the dilatation of the ventricle, with the systolic phase states the peak of R wave and stops at the end of the T wave. Typically the main trigger is set to threshold the R wave peak. The electrical activity is modeled as a moving dipole in the chest.

The earliest approach was to measure the potential differences induced by the dipole on three distal body parts. Nowadays electrodes are placed close to each shoulder and one on the left lower abdomen, forming the Einthoven triangle, deriving the three Einthoven leads. Using these, the QRS-complex can be detected and used as an external triggering source [5].

2.7.2 Respiratory triggering

There are a lot of MRI artifacts due to motion during the acquisition of k-space. One method of detection are navigators, a second is respiratory gating using a pneumatic belt.

Respiration is the cyclic expansion and deflation of the lung. This is achieved by vertical movement of the diaphragm and the elevation and deflation of chest cavity to alter the diameter of the chest. Respiratory motion is shown in figure 2.14, with different phases. The cycle consists of two alternating parts, i.e. inspiration and expiration. During inspiration air is inhaled by

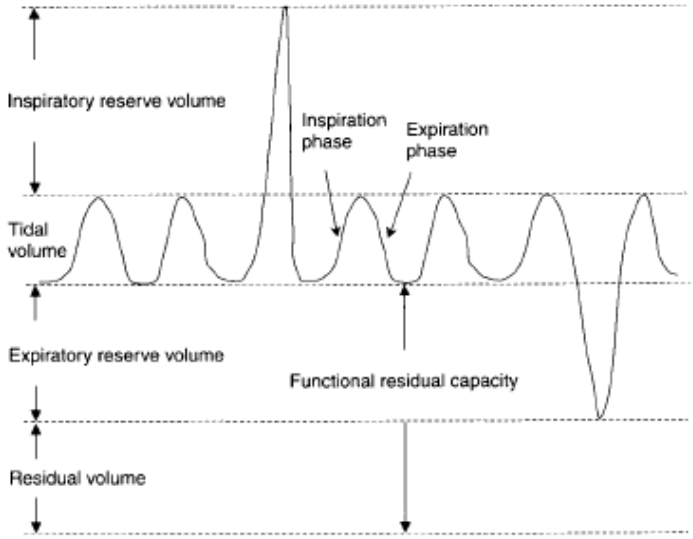

Figure 2.14. Schematic respiratory waveform showing various respiratory phases

negative alveolar pressure and followed by expiration, where air is forced out by positive pressure, compared to atmospheric pressure. Additionally an extra amount of air can be inhaled forcefully (the inspiratory reserve volume). Likewise in expiration an extra amount of air can be exhaled (the expiratory reserve volume).

The two used methods measure different motions of respiration. The pneumatic belt measures the change in diameter of the chest, resulting in pressure changes in the belt, which is detected by a pressure sensor. This allows for real-time detection of respiratory motion.

The use of the pneumatic belt allows to use the continuously measured data to set a window of the respiratory phase in which image acquisition is performed (respiratory gating). Respiratory triggering refers to data acquisi-

tion when a certain level of respiratory depth is passed in the exhaling or inhaling timing process.

The navigators on the other hand detect the motion of the diaphragm to determine the phase of respiration. Navigators measure a strongly reduced k-space to monitor movement of body parts, like the movements of the head or respiration. The navigator echoes are interlaced in the normal acquisition. The main presumption for the use of navigators is that every movement in between the navigator and the sequence is sufficiently small.

Navigators can use all forms of 1D, 2D or 3D k-space trajectories. With the simplest trajectory (1D), motion in one dimension, in readout direction of the navigator, can be performed. RF excitation of navigators is normally spatially selective and can be encoded, using simple spin-echo or gradient-echo. Often navigators do not need separate RF excitation, but can use the transverse magnetization of the regular RF pulse, before or after acquiring the image.

The data acquired with navigators can be used for either prospective or retrospective correction. Prospective gating keeps the imaging volume unchanged but gates the acquisition to keep anatomical consistency. Slice following (tracking) moves the scan volume accordingly to the detected motion, to keep the slice in nearly the same anatomic region. Phase reordering methods alter the data acquisition order in real time based on navigator data leading to a k-space data, that is more consistent regarding respiratory phase.

Numerous methods of retrospective correction exist. One is to use navigator information to correct the data during reconstruction by applying a phase

correcting factor which compensates the motion during acquisition. Another method acquires phase-encoding steps a specified number of times, interleaved with navigator measurements. Afterwards only the phase-encoding lines most consistent with specified position of the anatomy are used in the final image.
For imaging the heart a combination of respiratory and cardiac triggering is applied. First, navigators determine when the respiratory cycle is in a predefined position (usually the end-expiratory position) and consequently cardiac triggered acquisition initiates, suppressing artifacts from the movements of the heart.
In this work retrospective correction is used in order to discard images acquired in a respiratory out of the specified window.
In order to use navigators for recording of respiratory motion, the placement of the navigator is at the dome of the liver. In case one navigator is not sufficient, more navigators can be applied to correct multi dimensional motion [5].

2.8 Summary

The techniques described previously are applied to different regions of the body. TOF is applied to the head-neck region to image the carotid and cerebral arteries. Arterial spin labeling using a bSSFP readout is applied to image the renal vessels using navigator ECG triggering and respiratory gating and to the carotids using ECG-triggering. Cardiac gated TSE is applied to the femoral arteries using ECG-triggering. The PCA is used to

image the carotids and cerebral vessels as well as the renal vessels.

3 Image Reconstruction Methods

3.1 Introduction

In the previous chapter different acquisition methods for k-space data were described. This data is encoded in the Fourier space and needs to be reconstructed to form an image. This chapter describes the foundations of k-space sampling and image reconstruction. On this basis specific methods for accelerated acquisition in conjunction with advanced reconstruction algorithms used in this work are described.

3.2 Image reconstruction and spatial encoding

For image reconstruction the data is acquired in k-space (frequency space). Spatial encoding is performed asd described by the use of magnetic gradient fields. Therefore an MRI-signal can be computed as equation 3.1:

$$s(t, G_y) = \int_{-\infty}^{+\infty} \int_{-\infty}^{+\infty} \rho(x, y) e^{-\imath(\Phi(x,t)+\Phi(y,G_y))} dx dy \tag{3.1}$$

The phase term can be further denoted as:

$$\Phi(x,t) = -\gamma x \int_0^t G_x d\tau \equiv k_x x \tag{3.2}$$

$$\Phi(y,G_y) = -\gamma y \int_0^T G_y d\tau \equiv k_y x \tag{3.3}$$

leading to the fundamental MR-Signal equation

$$s(k_x,k_y) = \int_{-\infty}^{\infty}\int_{-\infty}^{\infty} \rho(x,y) e^{-\imath(k_x x + k_y y)} dx dy \tag{3.4}$$

In these equations G_x is the frequency encoding gradient, G_y the phase encoding gradient, γ the gyro-magnetic ratio, ρ the underlying spin density and T the duration of the phase encoding gradient.

Equation 3.4 is easily identified as a two dimensional Fourier transform, implying that the spin density can be reconstructed using inverse Fourier transform. k_x and k_y are the positions of the acquired samples, defined by the k-space trajectory. figure 3.1 shows four commonly used 2D k-space trajectories, with Cartesian encoding in a), radial projection in b), echo-planar in c) and spiral in d). Consequently, in order to image a volume of interest, individual slices with 2D encoding are acquired and reconstructed using equation 3.4. Using two phase encoding directions the reconstruction extents to a 3D inverse Fourier transform. The 3D approach allows more complex k-space trajectories, for example radial encoding in x,y plane and Cartesian in z plane (so called stack of stars trajectory) or full radial sampling in 3D. The use of two phase encoding directions was the prerequisite for

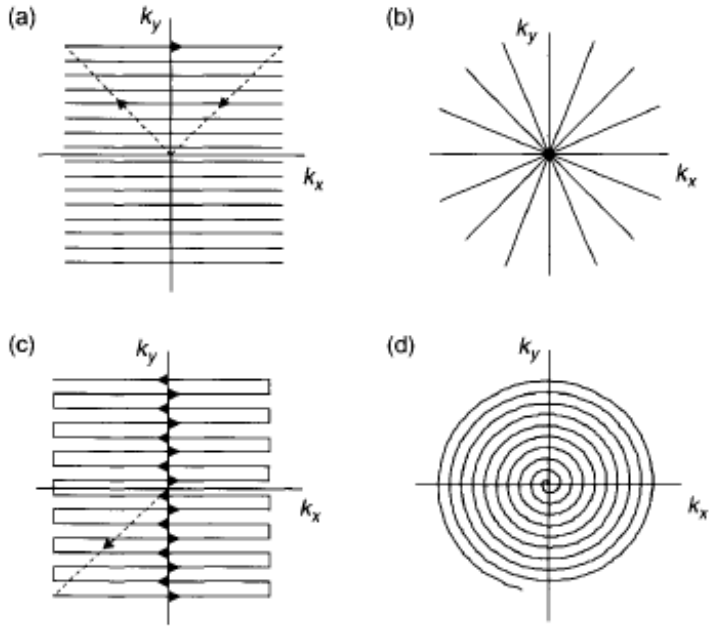

Figure 3.1. Depiction of four commonly used k-space trajectories. a) shows Cartesian trajectory for non-echo-pulse-train sequences, b) radial projection trajectory, c) echo-planar imaging and d) spiral encoding. Dashed lines show pre-phasing or re-phasing trajectories and arrows indicate direction of k-space traversal.

the field of compressed sensing (CS) im MRI and the use of randomized sampling patterns [15] (for 2D radial encoding CS is as well possible).

3.3 Parallel Imaging

For acceleration of image acquisition, the idea is to reduce the number of phase encoding steps for acquisition, conserving the image resolution. The concept of parallel imaging states that with the use of multiple receive coils

the information of the signal can be complemented [16]. The additional information provided by the use of multiple coils allows to accelerate image acquisition of k-space data, termed undersampling. Using undersampling results in aliasing artifacts introduced in the image, due to the properties of Discrete Fourier transform. In case of a Cartesian sampling trajectory this results in backfolding artifacts.

The application of phased coil arrays allowed to use the information of the spatial location of the receive coils for algorithms to reconstruct undersampled k-space data [16]. The first algorithms were SMASH[17], GRAPPA[1] and SENSE[18]. The two most used algorithms GRAPPA and SENSE are described in sections 3.3.2 and 3.3.1.

Initially phased array coils were intended to enhance SNR of MR acquisitions. An array consists of multiple small receive coils, each covering only a small part of the actual field-of-view (FOV). The signals of each receive coil are merged into a single image of the full FOV. The use of multiple receive coils can be considered in image reconstruction by expand equation 3.4 to:

$$s_k(k_x, k_y) = \int_{-\infty}^{\infty} \int_{-\infty}^{\infty} \rho(x,y) c_k(x,y) e^{-\imath(k_x x + k_y y)} dx dy \tag{3.5}$$

In equation 3.5 the signal of coil k is s_k with the respective coil sensitivity c_k. The optimal combination in terms of SNR of the receive coils is achieved with pixel by pixel summation of the signals of the individual coil elements, weighted with the respective coil sensitivity at the location of the pixel [19, 20]. The hindrance of this approach is, that the exact coil sensitivity is not available. One approach practically used is the calculation of the root of

the sum of squares of individual coil images $\hat{\rho}_k$ consequently after inverse Fourier transform. equation 3.6 describes this approach with N the total amount of coils used.

$$\hat{\rho}_{SOS} = \sqrt{\sum_{i=1}^{N} |\hat{\rho}_k|} \tag{3.6}$$

With the use of multiple receive coils, an higher SNR of the resulting image can be obtained, though the amount of data acquired with each measurement increases with the number of receive coils.

In order to reduce the amount of data that has to be processed, coil compressing strategies are applied. The strategy used in this work, is a method based on single value decomposition, as shown in [15], to reduce redundant data.

First, the MR data of a single slice is arranged in a two dimensional matrix with size $M \times N_c$, where N_c is the number of receive coils ans M the product of frequency and phase encoding steps, denoted as D. This matrix can be decomposed in the form of:

$$D = U\Sigma V^H \tag{3.7}$$

with U a unitary $M \times M$ matrix, V^* a unitary $N_c \times N_c$ (V^H representing the conjugate transpose of V) and Σ an $M \times N_c$ diagonal matrix. $\Sigma_{ii} = \sigma_1, \ldots, \sigma_{min(M,N_c)}$, representing the diagonal entries of Σ, are the singular values uniquely specified by D.

A common approach of coil compression is to truncate the singular values

after a specified threshold τ:

$$\hat{\Sigma}_{ii}^{\tau} = \begin{cases} \Sigma_{ii} & \Sigma_{ii} \geq \tau \cdot max(\Sigma_{ii}) \\ 0 & \text{otherwise} \end{cases} \tag{3.8}$$

Let Σ^{τ} be a truncation of $\hat{\Sigma}_{ii}^{\tau}$, consisting of just $M \times N_c^{\tau}$ non-zero elements and $(V^{\tau})^H$ the respective truncation, using just the upper left $N_c^{\tau} \times N_c^{\tau}$ elements of V^H, the compressed data D^{τ} is calculated using

$$D^{\tau} = U\Sigma^{\tau}(V^{\tau})^H \tag{3.9}$$

3.3.1 SENSE

The image reconstruction algorithm SENSE is applied in image space. Methods of Cartesian undersampling violate the sampling theorem [18], due to a reduced FOV and introduce periodic repetitions of the original FOV image $\hat{\rho}$. Consequently it states, that every pixel I^k of the accelerated image attained with one coil k is a superposition of R, the acceleration factor, pixel of $\hat{\rho}$, weighted by the values of the coil sensitivities C^k at the referred pixel position l:

$$I^k = \sum_{l=1}^{R} C_l^k \cdot \hat{\rho}_l \tag{3.10}$$

Index k counts from 1 to the number of coil elements, l from 1 ro R. For $N_c = 3$ and $R = 2$, all pixels from each coil are stacked in one complex signal vector $\overrightarrow{I}$ with dimension $N_c \times 1$. Equivalently for all superimposed pixels from the original FOV image $\hat{\rho}$, forming an $R \times 1$ vector $\overrightarrow{\hat{\rho}}$ and C written as $N_c \times R$ matrix containing the coil sensitivities of all coils at

superimposed positions, leading to a set of linear equations:

$$\begin{pmatrix} I_1 \\ I_2 \\ I_3 \end{pmatrix} = \begin{pmatrix} C_{11} & C_{12} \\ C_{21} & C_{22} \\ C_{31} & C_{32} \end{pmatrix} \begin{pmatrix} \hat{\rho}_1 \\ \hat{\rho}_2 \end{pmatrix} \tag{3.11}$$

This set of equations depicted in matrix notation:

$$\overrightarrow{I} = C \cdot \overrightarrow{\hat{\rho}} \tag{3.12}$$

With knowledge of the coil sensitivities matrix C, the original values of the full FOV image $\overrightarrow{\hat{\rho}}$ can be calculated by generalized inversion, like the pseudoinverse $pinv(C) = (C^H C)^{-1} C^H$:

$$\overrightarrow{\hat{\rho}} = pinv(C) \cdot \overrightarrow{I} \tag{3.13}$$

This reconstruction step is repeated for each pixels of the image with reduced FOV. Though only 1D subsampling is depicted here, it is also possible to expand the subsampling to the second phase encoding direction in 3D imaging [21].

For the application of SENSE the coil sensitivities C have to be known. In this work we use two different methods. First, a separate prescan with low spatial resolution. Second, an estimate of the coil sensitivities from image information, discussed in section 3.3.3, as implied in [18].

3.3.2 GRAPPA

A different approach is GRAPPA [1], which retrieves missing k-space data not acquired during measurement, contrary to SENSE which works in image domain. The idea of GRAPPA is that as a result fo the use of phased

array coils, each coil image contains a modulation of the underlying spin density $\hat{\rho}$ and C^k, suggesting that the acquired k-space data is a convolution of the Fourier transform of C^k and the Fourier transform of $\hat{\rho}$. This process allocates information stored in one k-space data point to its adjacent neighbors. Accordingly, by application of a weighted linear combination of contiguous samples, missing data points can be recovered. The used weights represent the influence of the coil sensitivities and are estimated prior to reconstruction. The auto calibration-signal (ACS) is used for the estimation, which is located at the center of k-space. Equivalently the formulation of the algorithm is denoted in 1D subsampling , with a single phase encoding direction, in y dimension, for simplification. An extension for 2D-GRAPPA is descried in [22].

All signals from the coils contributing to one k-space position k_y are packed in one single vector, with dimension $1 \times N_c$ denoted $\overrightarrow{\hat{s}}$. This vector is fitted to an ACS sample point $\overrightarrow{\hat{s}}^{(m)}_{acs}$ at position $k_y + m \cdot \Delta k_y$, with m running from 1 to $R - 1$:

$$\overrightarrow{\hat{s}}^{(m)}_{acs} = w^{(m)} \cdot \overrightarrow{\hat{s}} \tag{3.14}$$

The weighting matrix $w^{(m)}$ is of dimensions $N_c \times N_c$ and displaces data points in k-space by $m\Delta k_y$. A general implementation fits multiple source points of the source vector $\overrightarrow{\hat{s}}^{(src)}$ simultaneously to multiple target points $\overrightarrow{\hat{s}}^{(trg)}$. Therefore a GRAPPA reconstruction kernel is defined, consisting of $N_x \times N_y$ source points, which are fit to $R - 1$ target points for all coils concurrently. This leads to an amount of points in $\overrightarrow{\hat{s}}^{(src)}$ of $N_{src} = N_c \cdot N_x \cdot N_y$ and an amount of target points of$N_{trg} = N_c \cdot (R - 1)$. One typical

kernel size 5×5 and for example 12 ACS lines in a 256×256 image, this kernel would fit several times. Therefore the kernel is slided through the ACS block, resulting in an strongly overdetermined set of equations to be optimized, enabling a more robust result. For N_{rep} the number of repetitions of the kernel in the ACS block, the number of source points extend to a $N_{src} \times N_{rep}$ matrix, S^{src} and the number of target points to a $N_{trg} \times N_{rep}$ matrix, resulting in the weight matrix W with dimension $N_{trg} \times N_{src}$ which is calculated using:

$$S^{trg} = W \cdot S^{src} \tag{3.15}$$

$$W = S^{trg} \times pinv(S^{src}) \tag{3.16}$$

This matrix of GRAPPA coefficients is consequently used to compute the missing data points from acquired samples.

$$S^{clc} = W \cdot S^{acq} \tag{3.17}$$

The matrix S^{clc} contains all missing data points for all coils. All not acquired data points are calculated by sliding the GRAPPA kernel through all k-space positions. As a result a full k-space is regained and therefore inverse Fourier transform applied for each coil. At last all coil images are combined using one established methods, for example sum-of-squares.

3.3.3 Coil sensitivity estimation

Both methods, SENSE and GRAPPA, rely on a proper estimate of the coil sensitivity profiles of the full array, used for data acquisition. The main difference is that SENSE needs an actual estimation of the sensitivities,

usually done prior to the accelerated scan. On the contrary GRAPPA does not estimate the sensitivities directly, but encodes this information in the reconstruction coefficients. These coefficients are directly estimated using the fully sampled central k-space block (ACS). The extension of this approach for the SENSE method is called mSENSE [23]. For the reconstruction of non Cartesian sampling patterns the SENSE formulation is restated as optimization problem, called CG-SENSE [2].
Two methods of coil estimation are used in this work. The first is the proposed method by Walsh et al. [20]. The second approach for estimation of coil sensitivities was proposed by Knoll [15]. Prior to reconstruction, for each coil a quadratic regularization of the derivative is applied (so called H^1-regularization) followed by convolution with a smoothing kernel. The final estimate is calculated dividing each coil with the sum of squares image for each coil.

3.3.4 Sampling strategies

There are numerous sampling strategies for Cartesian sampling pattern like centric or elliptical acquisition. These strategies do not reduce the amount of data acquired. For reduction of data gathered two strategies are used in this work. First, equidistant subsampling and second random subsampling. To estimate coil sensitivity for image data, the sampling pattern need an ACS block in the center of k-space. Figure 3.2 show a equidistant pattern on the left (figure 3.2a) and a random on the right (figure 3.2b), with image matrix $(256, 256)$ and ACS block 24×24.

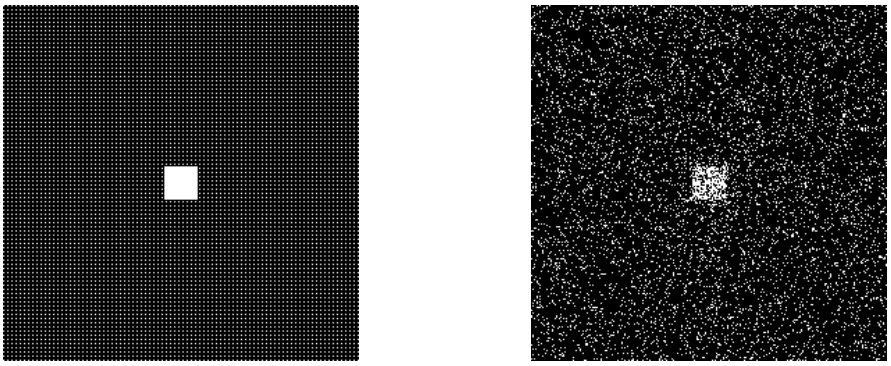

(a) equidistant pattern (b) random pattern

Figure 3.2. Depiction of two undersampling pattern applied in Cartesian acquisition, equidistant pattern on the left and random pattern on the right

3.4 Advanced reconstruction methods

3.4.1 The MRI reconstruction as inverse problem

This family of approaches is based on the formulation of image reconstruction as an inverse problem. The advantage of this formulation is that is allows the use of non-Cartesian sampling patterns and the use of various penalty terms. The so called forward problem is written like, describing the mapping of a reconstructed image to the measured k-space:

$$K\vec{u} = \vec{s} \tag{3.18}$$

with all single data points stored in $\vec{s}$, and the image to be determined $\vec{u}$, storing all image information containing N^2 pixel values, for a $N \times N$-matrix and K covering all operations performed on the original image, like undersampling or parallel imaging. For the case of undersampling,

the problem leads to a vector $\overrightarrow{s}$ smaller than $\overrightarrow{u}$ and therefore in an underdetermined problem with the need to reformulate the reconstruction as an optimization problem:

$$\overrightarrow{\hat{u}} = argmin\frac{1}{2}||K\overrightarrow{u} - \overrightarrow{s}||_2^2 \tag{3.19}$$

This optimization allows the consideration of a-priori knowledge about structure of the result of the optimization problem, compensating the lack of sufficient measurement data, with the idea of half-Fourier imaging as the first approach [24]. With the notation as an inverse problem, equation 3.19 can be extended covering the a-priori knowledge:

$$\overrightarrow{\hat{u}} = argmin\frac{1}{2}||K\overrightarrow{u} - \overrightarrow{s}||_2^2 + \sum_i \lambda_i R_i(\overrightarrow{u}) \tag{3.20}$$

In equation 3.20 R_i represent penalty terms added to the cost function of the minimization problem, commonly known as regularization.

3.4.2 Total Generalized Variation reconstruction

The main part of this chapter is based on publications by Bredies et al. [3] and Knoll et al. [25]. Total Generalized Variation (TGV) is a consequent further development of the concept of Total Variation (TV) in MRI reconstruction. TV is used for image regularization, image denoising, correction of truncation artifacts and inpainting sensitivity maps, as well as regularization method in compressed sensing framework and iterative reconstruction of undersampled radial data sets. Nonetheless, the underlying assumption of TV is that an image consists of regions that are piecewise constant. This

is violated caused by inhomogeneities in exciting B^1-field over MRI system with 3T and stronger.

The concept of Total generalized Variation introduced in [3] is a functional, that is capable of measuring image characteristics up to a specific order of differentiation. Based on the definition, usually written like:

$$\mathrm{TV}(u) = \int_{\Omega} |\nabla u| dx \tag{3.21}$$

The second-order Total Generalized Variation which is described in this chapter is based on this definition formulated as minimization problem:

$$\mathrm{TGV}^2_{\alpha}(u) = \min_{v} \alpha_1 \int_{\Omega} |\nabla u - v| dx + \alpha_0 \int_{\Omega} |\mathcal{E}(v)| dx \tag{3.22}$$

In this formulation, the minimum is determined from all complex vector fields v (including ∇u) on Ω and $\mathcal{E} = \frac{1}{2}(\nabla v + \nabla v^T)$ denoting the symmetrized derivative. With this definition a balancing between the first and second derivative can be established (ratio of α_0 and α_1). The parameters are set to $\alpha_1 = 1$ and $\alpha_0 = 2$.

The penalty terms defined in equation 3.21 and 3.22 can be readily used for regularized MRI reconstruction (3.20) yields to equation 3.23 and 3.24[15]:

$$\hat{u} = \arg\min_{v} \frac{1}{2} ||Ku - s||_2^2 + \lambda \mathrm{TV}(u) \tag{3.23}$$

$$\hat{u} = \arg\min_{v} \frac{1}{2} ||Ku - s||_2^2 + \lambda \mathrm{TGV}^2_{\alpha}(u) \tag{3.24}$$

Using this formulation the coil sensitivities are still required for the reconstruction. As the problems equation 3.23 and 3.24 state non-smooth yet convex optimization problems more elaborate numerical methods as for, e.g.

CG-SENSE need to be employed. Here we use the algorithm proposed by [26]. Following the primal-dual algorithm for the reconstruction problem is stated:

Algorithm 1 TGV reconstruction for undersampled data

procedure TGV RECONSTRUCTION(g^h)
  $u^h, \overline{u}^h \leftarrow 0, v^h, \overline{v}^h \leftarrow 0, p^h \leftarrow 0, q^h \leftarrow 0, r^h \leftarrow 0$, choose$\tau, \sigma > 0$.
  repeat
    $p^h \leftarrow \text{proj}_{P^h}(p^h + \sigma\nabla^h(\overline{u}^h - \overline{v}^h))$
    $q^h \leftarrow \text{proj}_{Q^h}(q^h + \sigma\mathcal{E}^h\overline{v}^h)$
    $r^h \leftarrow \text{prox}_2^{\sigma}(r^h + \sigma(K^h\overline{u}^h) - g^h)$
    $u^h_{old} \leftarrow u^h$
    $u^h \leftarrow u^h + \tau(div_1^h p^h - (K^h)^* r^h)$
    $\overline{u}^h \leftarrow 2u^h - u^h_{old}$
    $v^h_{old} \leftarrow v^h$
    $v^h \leftarrow v^h + \tau(p^h + \text{div}_2^h q^h)$
    $\overline{v}^h \leftarrow 2v^h - v^h_{old}$
  until convergence of u^h
  return u^h
end function

This algorithm converges for $\sigma\tau < h^2/(h^2 + \sqrt{8}h + 8)$, therefore setting $\sigma = \tau = 1/\sqrt{12}$ for convergence.

3.4.3 Iterative regularized Gauss-Newton (IRGN) Method

It was demonstrated, that non-linear inversion can be successfully applied to image reconstruction of undersampled data from multiple coils [27–29]. The key feature is the joint estimation of coil sensitivities along with the image itself, using an iteratively regularized Gauss-Newton (IRGN) method. As shown in [15] this method can be extend to use different penalty formulations like TV or TGV.

Mathematically speaking, parallel MR imaging can be denoted as a nonlinear inverse problem, with the sampling operator $\mathcal{F}_S$, specified by k-space acquisition trajectory, containing the sampling pattern in Cartesian acquisition and the Fourier transform and the accordingly acquired k-space samples $s = (s_1, \ldots, s_N)^T$ of N receive coils are given, the spin densities u and the unknown or poorly known set of coil sensitivities $c = (c_1, \ldots, c_N)^T$ have to be determined to fulfill:

$$F(u, c) := (\mathcal{F}_S(u \cdot c_1), \ldots, \mathcal{F}_S(u \cdot c_N))^T = s \tag{3.25}$$

this can bes solved using an iteratively regularized Gauss-Newton method [28, 29] by computing in each step k for a given $x^k := (u^k, c^k)$ the minimum $\delta x := (\delta u, \delta c)$ of

$$\min_{\delta x} \frac{1}{2}||F'(x^k)\delta x + F(x^k) - s||^2 + \frac{\alpha_k}{2}\mathcal{W}(c^k + \delta c) + \beta_k \mathcal{R}(u^k + \delta u) \tag{3.26}$$

for set $\alpha_k, \beta_k > 0$ and defining $x^{k+1} := x^k + \delta x, \alpha_{k+1} := q_\alpha \alpha_k$ and $\beta_{k+1} := q_\beta \beta_k$ with $0 < q_\alpha, q_\beta < 1$. $F'(x^k)$ is the Jacobian of F evaluated at x^k and the term $\mathcal{W}(c) = ||Wc||^2 = ||w \cdot \mathcal{F}c||^2$ is a penalty on the high Fourier coefficients of the sensitivities and $\mathcal{R}$ the regularization term of the image.

Initially the application of IRGN method on parallel imaging reconstruction was formulated using a conventional L^2 penalty [28] ($\mathcal{R}(u) = \frac{1}{2}||u||^2$) and the use of a TGV penalty introduced by [4] setting the penalty term to as equation 3.22

$$\beta\mathcal{R}(u) = \inf_{v} \beta||\nabla u - v|| + 2\beta||\mathcal{E}v|| \tag{3.27}$$

The algorithms used for IRGN-TGV reads as follows:

Algorithm 2 IRGN-TGV reconstruction subproblem for undersampled data

procedure TGVSOLVE(u, c, g, α, β)
  $\delta u, \overline{\delta u}, \delta c, \overline{\delta c}, \delta v, \overline{\delta v}, p, q \leftarrow 0$, choose$\tau, \sigma > 0$.
  repeat
    $p^h \leftarrow \text{proj}_\beta(p + \tau(\nabla(u + \overline{\delta u}) - v))$
    $q \leftarrow \text{proj}^2_\beta(q + \tau(\mathcal{E}v))$
    $\delta u_{old} \leftarrow \delta u, \delta c_{old} \leftarrow \delta c, \delta v_{old} \leftarrow \delta v$
    $\delta u \leftarrow \delta u - \sigma(\sum_{i=1}^{N} c_i^* \cdot \mathcal{F}_S^*(\mathcal{F}_S(u \cdot \overline{\delta c_i} + c_i \cdot \overline{\delta u}) + F(u,c) - g) - \text{div}p)$
    $\delta c \leftarrow \delta c - \sigma(u^* \cdot \mathcal{F}_S^*(\mathcal{F}_S(u \cdot \overline{\delta c_i} + c_i \cdot \overline{\delta u}) + F(u,c) - g) + \alpha W^* W(c_i + \overline{\delta c_i}))$
    $v \leftarrow v - \sigma(-p + \mathcal{E}^* q)$
    $\overline{\delta u} \leftarrow 2\delta u - \delta u_{old}$
    $\overline{\delta c} \leftarrow 2\delta c - \delta c_{old}$
    $\overline{v} \leftarrow 2v - v_{old}$
  until convergence
  return $\delta u, \delta c$
end function

4 Experiment Setup

This chapter describes the actual methods used for image acquisition, data preprocessing for the purpose of offline reconstruction and the application of the various reconstruction methods described in chapter 3.

4.1 Measurement protocols

Here, all measurements applied in order to provide for the reconstruction software described in the subsequent chapter are stated. First, the measurement schedule is described.
All measurement data is acquired using a clinical MR scanner (SIEMENS Magnetom Skyra 3T, Erlangen, Germany). All examinations were taken on voluntaries, who gave consent to be examined.

4.1.1 Cardiac-gated turbo-spin echo measurement protocol

A cardiac-gated turbo spin echo (TSE) sequence is part fo the SIEMENS protocol suite NATIVE [30], which contains a set of tailored protocols developed for contrast agent free angiography methods.

For the acquisition of peripheral angiograms the SIEMENS protocol NATIVE-SPACE 3D is used. This protocol uses cardiac gating for TSE sequences described in section 2.3 and section 2.7. This sequence is designed for application on the peripheral body parts, like upper and lower leg. The image is acquired with the following measurement protocol.

1. Prior to the examination the patient is prepared applying ECG-electrodes and deriving the ECG for trigger purposes. Additionally the required receiver-coils are mounted, using the Spine-Coil-Array and the Surface-Coil-Array.
2. Application of scouting sequences to correctly define the anatomical area.
3. After the selection of the anatomical area, definition of Field-of-View (FOV) and resolution a 2D temporal scout (CINE scout) is performed, covering the cross-section of the afferent artery, femoral artery for thigh examinations or popliteal artery for lower leg examinations, lasting for at least one R-R-interval.
4. Subsequently the time from one R-peak to minimum and maximum flow velocity is derived and the trigger is set for the TSE sequences.
5. As additional setting any form of subsampling supported (*IPAT-card*) could be specified. Common subsampling methods are described in subsection 3.3.4.

4.1.2 Renal angiography

For renal angiography the SIEMENS protocol NATIVE TrueFISP, which is part of the SIEMENS NATIVE protocol suite is used. The TrueFISP sequence uses the in-flow spin labeling method with a bSSFP readout sequence. This protocol supports ECG-triggering with respiratory navigators and respiratory triggering using the pneumatic belt, as shown in [30–32].

1. Prior to examination the ECG-electrodes or the pneumatic belt are applied on the patients chest, as well as the Spine-Coil-Array and the Surface-Coil-Array.
2. Application of scouting sequences to determine the anatomical region
3. Selection of the anatomical region and configuring the trigger-levels.
    a) For ECG-triggering with respiratory navigators, the navigators need to be placed at the right hemisphere of the liver dome. The two navigators must intersect above the expiratory position of the liver dome, defining the expiratory state. Additionally the navigators must not interfere with the kidneys or the renal arteries, since the navigators are visible in the imaging volume.
    b) For respiratory gating the respiratory belt is applied on the chest at height of the diaphragm. It has to be ensured that the belt is tight enough to cover most of the dynamic range of the pressure sensor but not so tight to exaggerate the measurement range of the sensor.
4. After setting of the trigger the imaging volume and the first inversion slab are placed. The inversion slab needs to be positioned on the top

of the kidneys or if they are not symmetrically located in transversal direction, to cover the renal arteries. The top border of the imaging slab needs to coincide with the top border of first the inversion slab.

5. With the use of ECG-triggering there are two possibilities for the setting of the inversion time (TI) for spin-labeling.
   a) One is to automatically set the TI according to the cardiac cycle time. All settings are adapted by clicking the *Capture Cycle* in the *PACE* sub-card of the *Physio*-section.
   b) The second is to set the TI manually to a higher value in order to capture sufficient inflow in the renal arteries. Common values for 3T MRI scanners range from $1200ms - 2200ms$, as shown in [31, 33].
6. Using respiratory triggering TI has to be set to values in the range of $1200ms - 2200ms$, to ensure that at least one inflow event took place during the inversion time. Also the trigger level of the respiratory cycle is set close to the end-expiratory state to reduce the movement of the kidneys during acquisition, since endexpiratory state lasts longer than the inspiratory state.
7. When setting TI longer than the R-R-interval, there has to be an additional inversion slab added to suppress the venous inflow from distal body parts. This slab is positioned distal to the first with a thickness of $100mm$ and an TI of $800ms$.
8. Finally it has to be assured that *fat-suppression* is enabled.
9. Before the actual acquisition takes place, a navigator scout is performed

to set the trigger levels of the respiratory navigator, as well as the window of acceptance.

4.1.3 Phase-contrast angiography

There is a predefined sequence protocol that allows phase contrast angiography measurements using various flow encoding velocity settings and flow encoding directions. In this protocol there exists the possibility to enable ECG-triggering for small vessels and strongly unsteady flow.

1. Initially the positioning and the definition of FOV, resolution and oversampling is performed.
2. In the *Physio*-card there first has to be decided how velocity encoding is performed
   a) One flow direction with up to three different velocities (single direction)
   b) Up to three directions with one flow encoding velocity (single velocity)
   c) Specification of different encoding velocity and direction for each slab with up to three different encoding slabs. (Free encoding)
3. After the selection of the encoding scheme flow velocities and flow directions of the blood flow have to be set. For velocity measurements phase images are preferred, though for angiograms magnitude images of the complex differences of two images are calculated (see section 2.4). For velocity determination the $VENC$ parameter should be set close

to the maximum velocity and for angiograms about the half of the maximum velocity to have a considerable amount of spins for imaging (flow velocities see table 2.1 and section 5.1.2).

4.1.4 Time-of-Flight angiography

For time-of-flight (TOF) angiography there also exist predefined sequence protocols on the MRI scanner, with preset for 2D-TOF and 3D-TOF. Using the 3D-TOF protocol there are advanced techniques predefined like TONE-pulses and MOTSA-scheme as described in section 2.6.

1. First the imaging slab has to be positioned using localizers.
2. In the *Physio*-card the parameters for the TONE-pulse with entrance and exit flip angle and the curve in between need to be set (see section 5.1.1).
3. Additionally the MOTSA-properties are defined with the number of overlapping slices.
4. At last the flow direction of the entering blood needs to be specified.

4.1.5 Summary

The four protocols described in this section are used to provide the underlying data for the reconstruction. In order to test the reconstruction methods properly regarding acceleration factor, the results of these measurements have been conducted multiple times, to ensure a sufficient quality of data. Due to the more complex and newer approach of cardiac-gated TSE

and Spin-labeling with bSSFP readout and the use of physiological trigger sources, these two sequences needed more intensive testing than PCA and TOF.

Since the general purpose of the measurements is to provide considerable data to be compared to accelerated measurements, all acquisitions have been conducted using Cartesian sampling pattern and full k-space acquisition. Possible acceleration during measurement conducted directly on the MRI scanner were not performed due to the limited post processing possibilities, accepting longer measurement times and stronger artifacts arising from patient movement and measurement restrictions.

The TOF protocol is only applied to the region of neck and head, since it was especially developed for this purpose. The cardiac-gated TSE protocol is only applied to the thigh since it can easily be extended to the lower leg and reaches a great spatial coverage. PCA is applied to the head and neck region as well as to the renal vessels. The spin labeling technique with bSSFP readout is applied to the renal vessels as well as to the head neck region.

4.2 Reconstruction pipeline

This reconstruction pipeline is implemented in MATLAB (The MathWorks, Natick, MA) with the purpose of the applying the advanced reconstruction methods described in section 3.4.2 and 3.4.3. The full set of functions implemented would exceed the limitations of this written work. Nevertheless, all used functions are provided with a CD in the back of this work. Here only

important parts of the code are displayed in order to support the description provided in text. All calculations are performed in *single* precision based on the use of 32bit analog-digital converts in the MRI system. In the control

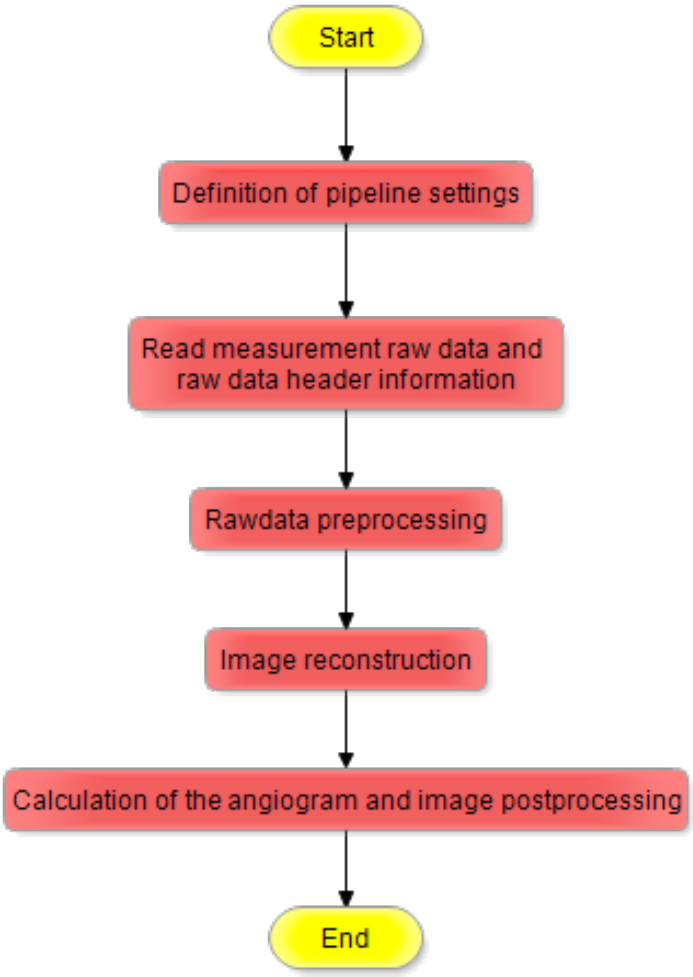

Figure 4.1. Flowchart of the general scheme for image reconstruction

file all parameters for image reconstruction, raw data preprocessing and raw data itself are defined and the main function itself is called.

In the first part of the main function the specified raw data file is read, as well as the information provided in the header of the raw data file. This is followed by all necessary preprocessing steps to ensure the same format for all steps up to come.
In the image reconstruction part the preprocessed data is handed to the implemented reconstruction algorithms.
Finally the reconstructed images are cropped to their final size and the angiograms are calculated based on the acquisition method used, schematically shown in figure 4.1.

4.2.1 Control file

All definitions for the following reconstruction pipeline are defined here, depicted as the first process step in figure 4.1.
The *file* parameter contains the raw data filename and the path of the file in reference to the current operating folder of MATLAB and the *file2* an optional coil-sensitivity scan scan performed before the actual measurement.
All parameters regarding preprocessing, image reconstruction and process parallelization are defined in the *params* variable of type *struct* with each parameter as a separate *field*.
In some measurement protocols partial Fourier acquisition or asymmetric echo is used. To recover the full k-space with the maximum in the center of the k-space, these simple acceleration techniques have to be undone. There are three ways in doing so. First is to fill the missing k-space with zeros, set with *zeroFill = 1* or using the hermitian properties of k-spaces of real

images and derive from the k-space of the other half, complex conjugate it and mirror it and insert it instead of the zeros, also referred to as hemodyne reconstruction. A different approach is to recover the missing k-space with iterative algorithms, most common projection on convex surfaces (POCS) freely available on [34], activated with *pocs_en = 1* in conjunction with the zero filled k-space.

The next set of variables define the way of undersampling used on the raw data. It is generally enabled with *subs = 1*, *sub_3d* toggles undersampling in both phase encoding directions on and off. With *subs_rand = 0* the undersampling scheme is set to equidistant undersampling using every n-th sample *stepsize = #sample* and a fully sampled center with size of #*y* and #*z* specified with *center_y_len* and *center_z_len*. Set *subs_rand = 1* a random sampling pattern is used for undersampling resulting in an acceleration factor specified in *acc = #number* and the size of center of the random pattern in *center_rand*. Additional in this part of the settings it can be selected if coil-compression is applied to the accelerated raw-data, neglecting the coils having a normed singular value less than 10% each.

The parameters *parall* defines if the parallel computing toolbox of MATLAB is used during the whole reconstruction process, with *par_fac* setting the number of parallel workers used.

The next set of parameters specify the image reconstruction process. The parameter *type* selects the type of reconstruction used, valid arguments are *'cg'*, *'tgv'* and *'irgntgv'*, all noted in *string*-type. *senseEst* selects the type of coil sensitivity estimation, available are *'walsh'*, *'h1_reg'* and *'meas'*, with selection of irgntgv this command is dispensable. In opposition the following

commands are only usable with the a prior selected *irgntgv* reconstruction type. The parameter *tvmaxits* sets the maximum steps of the Gauss-Newton algorithm. *tvstartits* sets the initial number of steps of the regularization problem in the extended IRGN algorithm. The field *irgntype* selects the type of regularization available for IRGN so far, 1 equals a TV-penalty term, 2 a TGV-penalty and 3 for Tikhonov regularization. Additionally the strength of penalizing higher spatial frequencies in reconstruction process can be set with *penalty*, where the default value is 8.
Additionally there can be a masking used for the images. This can be enabled setting *mask* = *1*. In an additional *struct*-parameter *or* all specifications for the mask are set.
Finally there is an override flag, *forced* which applies standard Fourier reconstruction to undersampled data if set. The function call is

```
fun_recon_all(file,file2,params,true,true);
```

with *file* and *file2* containing the names if the raw data, *params* containing all pipeline settings. The fourth parameter specifies if images are shown during the reconstruction process (default = false) and the fifth if the reconstructed data is saved to the hard drive (default = true).

4.2.2 Main function

The main function uses all parameters defined in the control file and pass them to the respective functions as well as providing all function calls and post processing of the given results. In figure 4.1 the second up to the

fifth process are handled by the main function. For easier recognition as reconstruction process, the second and third process in figure 4.1, read raw data and data header and raw data preprocessing, are combined to the following chapter 4.2.2.1. The fourth and fifth process are described separately.

4.2.2.1 Preprocessing

This part covers all preprocessing applied for all types of measurement data, schematically shown in figure 4.2. After initial definitions, eventually starting parallel computing and extracting the file name, the raw data from the specified file is read. For this purpose a new function was defined to manage the identification of the sequence type and the conjunction from all data pieces.
The function *readRAW_multichannel(file)* reads the raw data stored in the file with name *file*. This function uses the function *mapVBVD*, provided by the MR-IDEA user board[35] to read raw data from SIEMENS MRI scanners. There are additional parameters that simplify the read in of the raw data. All possible flags are described in the header of the function. In this work are the flag *'removeos'*, that removes the inherent frequency oversampling in MRI acquisition and the flag *'ignoreseg'*, which undoes the segmented acquisition are used. This function returns an object containing all raw data including additional information about the scan performed. When accelerated measurements were performed directly on the scanner, there exists an supplementary field, containing the reference data acquired in k-space

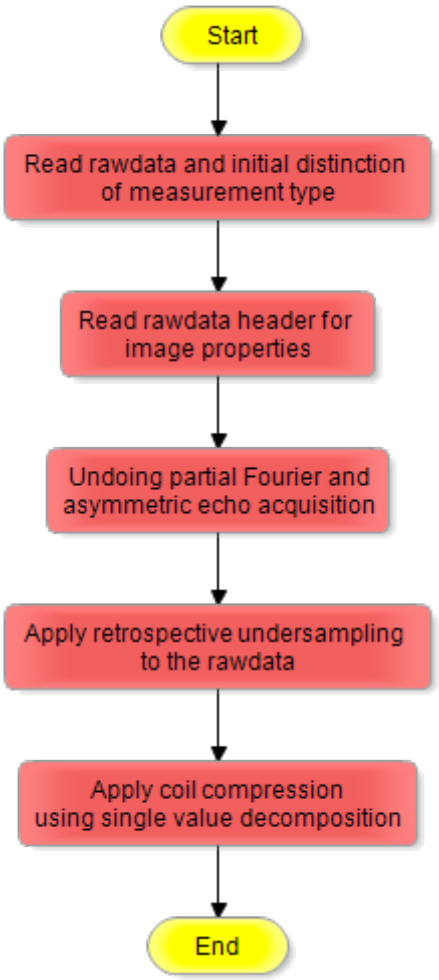

Figure 4.2. Flowchart of the preprocessing applied prior to image reconstruction

center, named *refscan*. This reference scan is inserted in the undersampled data to produce an accelerated image with fully sampled k-space center, for coil sensitivity estimation.

With the use of four different measurement protocols, there was the need to distinguish between them. The input of the protocols returns contains

four and six dimensions. All protocol have the same four dimensions: *Columns* indicating the number of frequency encoding steps, *Lines* stating the number of phase-encoding steps performed, *Parts* defining the number of slice-encoding steps in 3D imaging and *Channels* detailing the number of coils used. The simplest protocol only contains these four distinguishing dimensions, the bSSFP protocol. For the PCA one dimension is added: *Sets*, detailing the different velocity encodings used. Using a TOF protocol with MOTSA adds the dimension *Slice* and for the TSE there are two dimensions added: *Repetitions* and *Averages*. This two extra dimensions are reordered to one single dimension, such that only five dimensional matrices are handled by the reconstruction itself. Depending on the protocol used an identifier is added to specify the type of acquisition, and therefore allowing a separate calculation of the angiogram.

In the next step the necessary information of the file header is read. These informations contain resolution in all three dimensions, and the amount of actual acquired samples. Based on these values the size and resolution of the final images are computed. The computed values are *Base Resolution*, *Phase Resolution*, *Number of Slices*, *Phaseoversampling*, *Sliceoversampling* and a factor for partial Fourier, if used.

The next step is the undoing of partial Fourier acquisitions during measurement. The choice of reconstruction type is selected in the control file section 4.2.1. Following the principal procedure is described to undo partial Fourier sampling. All acquired k-space data has in 2D or 3D a maximum in the center. If the maximum of k-space data is not in the center of the volume for 3D in any dimension, the misplacement is calculated and consequently

the missing samples are inserted in each dimension accordingly to move the maximum to the center of the volume, partial Fourier acquisition in frequency encoding direction is called asymmetric echo acquisition.
Next part is the retrospective undersampling of the raw data. The two methods covered in this work were previously described in section 3.3.4. In addition to the pattern itself, the ACS-lines in the center have to be considered for equidistant undersampling, with the size of the ACS-block defined in the control file. The random sampling pattern, can be adjusted to have a fully sampled center, with the restriction of only covering the specified percentage of each dimension. To allow a limited comparison, the length of the fully sampled center was laid in phase-encoding direction and the slice encoding direction was adjusted automatically. The values of the ACS block are handed over to the coil estimation function.
Following undersampling, data reduction is performed. The reduction is achieved by compressing the coil information and neglecting the least contributing, using the technique described in section 3.3. The preliminary set for the threshold of the normed singular values is 10%.
As precaution as to not exceed the possible amount of RAM available on the workstation, the whole raw data set is temporary saved and each slab processed stand alone.
With all the previous step applied the data is ready to be handed to the reconstruction algorithms to recover the missing data.

4.2.2.2 Image Reconstruction

This chapter describes the image reconstruction process applied to the pre-processed data, schematically depicted in figure 4.3.
Prior to the actual reconstruction process the reduced sampling resolution still needs to be undone. This is achieved by simply padding the k-space on each dimension equally on both sides with zeros until the specified resolution in all three dimensions is met. This zero padding introduces the phenomena of Gibb's ringing, which can be overcome with windowing the initial k-space.
With all preprocessing applied, the reconstruction itself is computed. Depending on the selected reconstruction type, the coil sensitivities are estimated using the selected algorithm.
For the estimation of coil sensitivities based on [20], a script provided by Florian Knoll was extended to estimate 3D sensitivities. The main part is depicted in the following code example (full function *adapt_array_3D.m*):

```
for i=1:nc
  wfull(i,:,:,:)=conj(resize_M(squeeze(abs(wsmall(i,:,:,:))),[nz ny nx],...
  'bilinear').*exp(j.*resize_M(angle(squeeze(wsmall(i,:,:,:))),...
  [nz ny nx],'nearest')));
  cmap(i,:,:,:)=resize_M(squeeze(abs(cmapsmall(i,:,:,:))),[nz ny nx],...
  'bilinear').*exp(j.*resize_M(squeeze(angle(cmapsmall(i,:,:,:))),...
  [nz ny nx],'nearest'));
end
```

The second method of estimation is a H1-regularization based on the approach by [15] (full function *h1_l2_3D_pd.m*).
The third method is to calculate the sensitivities from a low resolution scan prior to the actual measurement. To gain the complex sensitivities, the individual coil is Fourier transformed, normalized into range $0 - 1$ and scaled to image size. In addition a mask can be calculated from the low resolution body coil image using the positioning information of the data files header. This can be enabled by setting the *mask* parameter in the control file (full function *getCoils.m*), all coil estimation functions are controlled with the superior function *calc_coil_sens.m*. In this work with the use of multiple slabs of the identical region in the body, coil sensitivities are just estimated prior to the reconstruction of the first imaging slab, only TOF measurements are excluded from this, due to the change of position of the imaging slab.
With the coil sensitivity estimation the actual reconstruction itself can start. Conjugated-gradient (CG) method needs three additional specification, the system matrix containing all applied modifications, like Fourier transform, undersampling pattern and gridding pattern as well as the number of maximum iterations and stopping criterion, stating the residual of the reconstruction to be minimized sufficiently.
Compared to CG-Sense, TGV reconstruction needs some different parameters. Same as CG are the transforming operators containing Fourier transform, gridding and subsampling pattern and the maximum number of iterations.
Instead of stopping criterion, the number of iterations is set to a value known to yield sufficient convergency [15]. The weighting of regularization

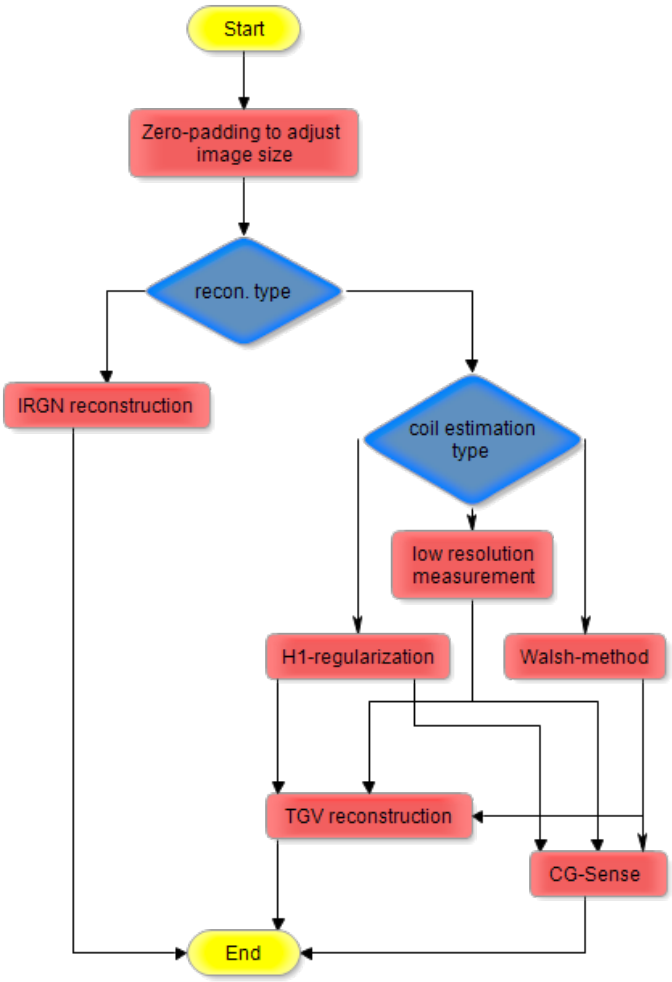

Figure 4.3. Flowchart of the reconstruction process

was investigated in [15], so the determined value in that work will be used ($\lambda = 8 \cdot 10^{-5}$).

The last reconstruction method, namely IRGN, is used with two different regularization terms. The first is Tikhonov regularization and the second TGV regularization. The weighting for regularization for Tikhonov was

set to $\alpha = 1$ and for TGV $\alpha = 1$, while the initial weighting for the coils sensitivities was set to $\beta = 1$. Like TGV and CG-Sense the function requires the system matrix consisting of the undersampling pattern, Fourier transform and gridding, but unlike CG-Sense and TGV no estimate of the coil sensitivities are needed, because they are jointly reconstructed together with the image.

4.2.2.3 Post processing

After the image reconstruction necessary post processing takes place (as depicted in figure 4.4). The first step in post processing is the discarding of the data acquired using oversampling in phase and slice direction as well as asymmetric echo acquisition in frequency encoding direction. Afterwards each acquisition has its own procedure to calculate the angiogram. For bSSFP acquisition the final image set is already the angiogram.
PCA measurements derive the angiogram by computing the magnitude of complex difference of a flow compensated and a flow encoded image slab, previously described in section 2.4. The result are three angiograms of each encoding step and are simply summed up to derive final angiogram.
For TOF measurements using the MOTSA technique the individual slabs have to be concatenated. The number of overlapping slices in each slab is defined in the data header. To create a smooth intersection a fading technique was applied. This starts with a relative maximum weighting for the first slab and amd a relative minimum weighting for the second slab. This weighting decreases linearly for the first slab and increases likewise for the

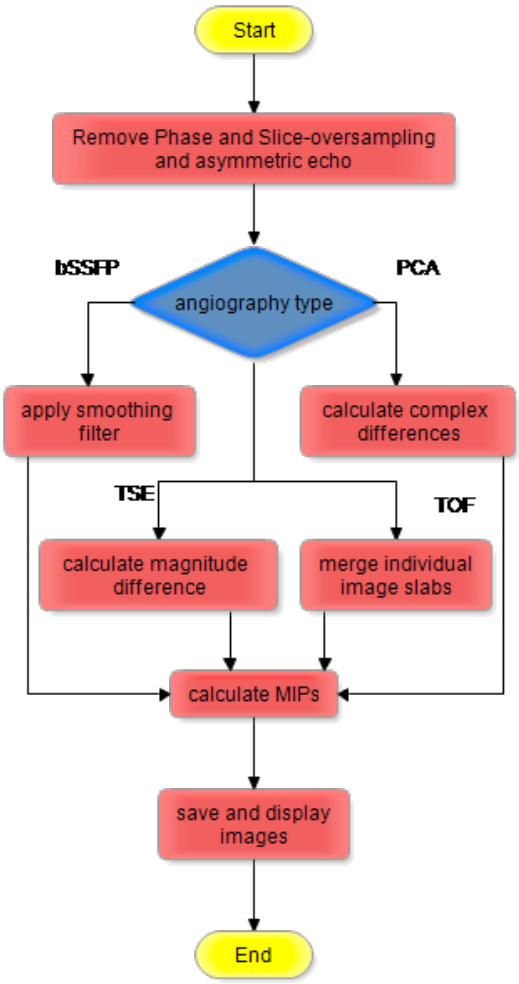

Figure 4.4. Flowchart of the image post processing

second. This method is applied for all overlapping slabs.

Cardiac-gated TSE measurements, which have by default multiple acquisitions, are first averaged in their domain. To retrieve the final result the image slab containing the fast flowing blood was to be subtracted by the one depicting the slow flowing blood.

For ease of depiction a Maximum Intensity Projection (MIP) in the dimension of interest is performed. The last step is to save all necessary information used and derived during the reconstruction process, like the initial settings, undersampling pattern, effective acceleration factor, the final images and the time computation for reconstruction.

4.2.3 Summary

The second part, the reconstruction, consists of testing two acceleration strategies, equidistant and random undersampling, using four different reconstruction methods, CG-Sense, TGV, IRGN with Tikhonov regularization and IRGN-TGV. In addition it was determined how strong actual measurements can be accelerated using Cartesian k-space trajectories for all four angiography methods.

5 Results

This chapter presents the results gained in this work. There will be a distinction between those solely gained by measurement on the MRI scanner and the results from image reconstruction. In the image reconstruction section contains a comparison of the different reconstruction results.

5.1 Image acquisition results

This section covers the image results of the actual measurements on the MRI scanner. These are grouped into the four acquisition techniques used, starting with the well developed protocols for TOF and PCA, cardiac-gated TSE and spin labeled bSSFP. The use of an low-resolution prescan to estimate coil sensitivities is limited to the TrueFISP as a result of hardware limitations, there is no prescan available for estimation for cardiac-gated TSE and PCA.

5.1.1 Time-of-flight angiography

TOF is a established technique for angiography of the head/neck region. The unfiltered results are shown in figure 5.2 containing the merged MIPs

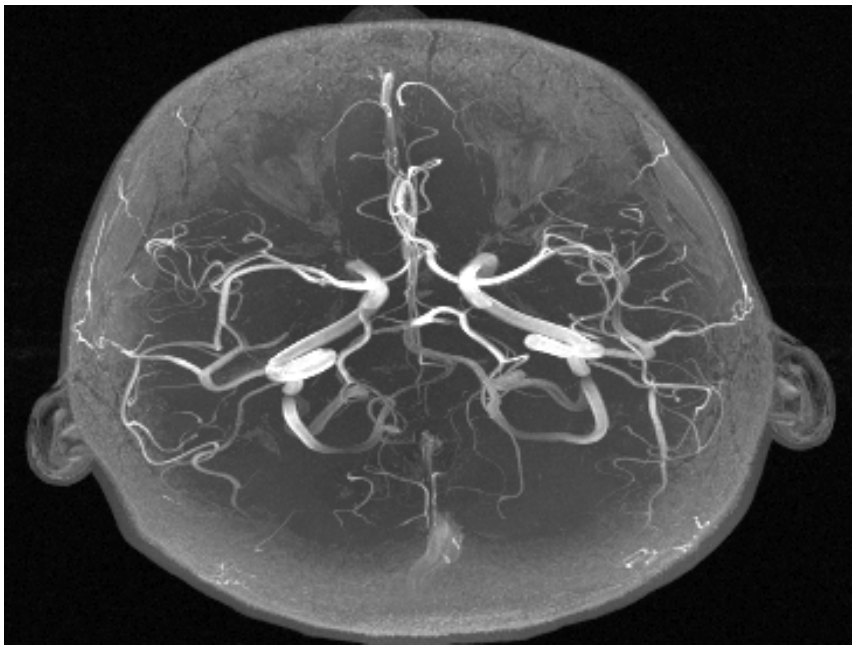

Figure 5.1. Depiction of transversal MIP of a TOF angiography using MOTSA and TONE

of whole image slab. The used sequence parameters were $T_E = 3.43ms$, $T_R = 21ms$, FOV $181.25 \times 200 \times 163.2mm$, resolution $384 \times 364 \times 204$, flip angle $\alpha = 20°$, MOTSA-overlap 15%, TONE pulse $20°$ with 3% ramp. The TOF sequence exhibits good contrast between the background tissue and the vessels. Very small vessels are as well identificable. It is clear to see where the image slabs are concatenated. The total acquisition time was for one of the four slabs 4 min10 s = 16 min 40 s with a resulting voxel size of $0.45 \times 0.55 \times 0.8mm^3$.

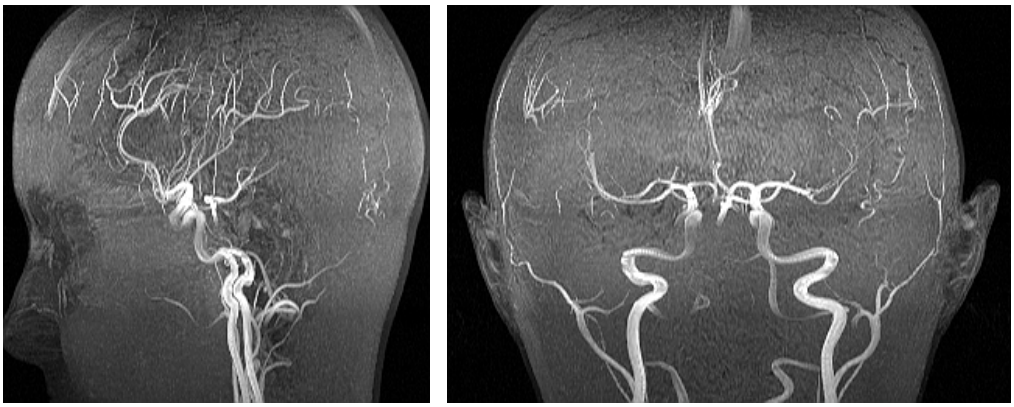

(a) sagittal MIP (b) coronary MIP

Figure 5.2. Depiction of coronary and sagittal MIP of a TOF angiography using MOTSA and TONE

5.1.2 Phase contrast angiography

PCA was applied to depict the renal vessels and the carotid and cerebral vessels. The flow velocities have been set to be about the average flow velocity in the vessels of interest. The first set of images was acquired of the head itself without the neck, as depicted in figure 5.3 and 5.4, showing all three MIPs of a PCA with FOV $240 \times 270 \times 158.4mm$, matrix size $256 \times 272 \times 176$, flip angle $\alpha = 10°$ with *VENC* $95cm/s$ in all three directions. Total acquisition time was 15 min 5 s. The second set of images, depicted in figure 5.5 and 5.6, shows all three PCA MIPs of the carotids proximal to the prior scan, with FOV $256 \times 192 \times 158.4mm$, image matrix of $256 \times 192 \times 176$, flip angle $\alpha = 10°$ and *VENC* $105cm/s$ in all three directions and took 17 min 4 s to acquire. The third possible applicable body part is the renal region, depicted in figure 5.7 and 5.8, showing all three MIPs of a PCA

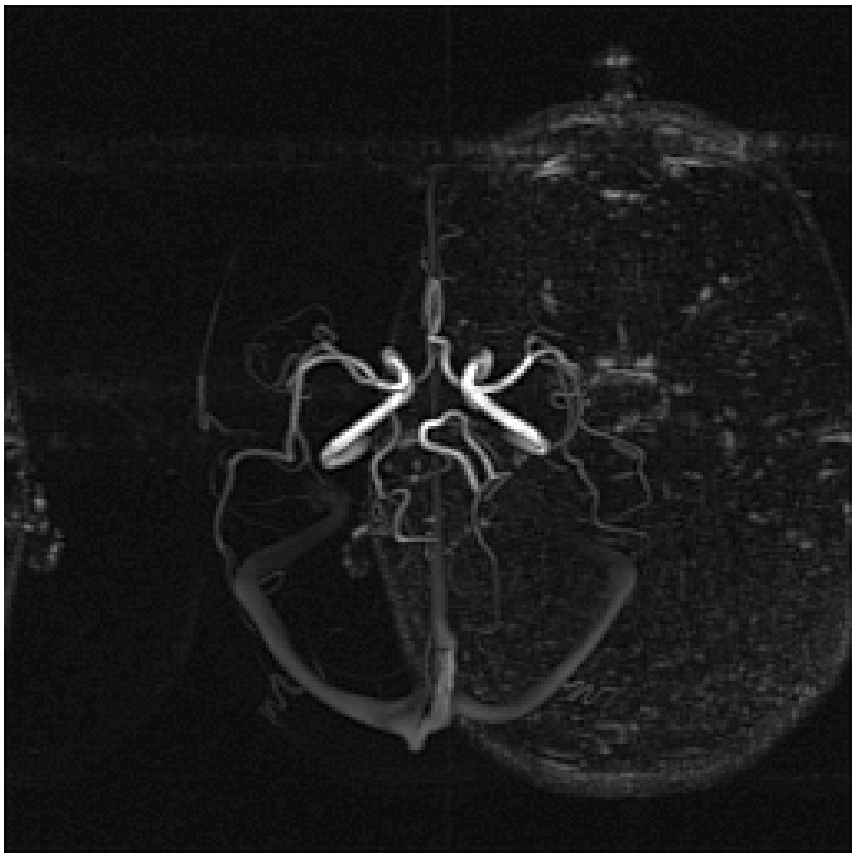

Figure 5.3. Depiction of transversal MIP of a PCA angiography of the head

with FOV $320 \times 270 \times 72mm$, image matrix of $384 \times 280 \times 80$, flip angle $\alpha = 10°$ and $VENC$ $65cm$ and $45cm$ in coronal direction and $65cm$ in sagittal direction and took 10 min 7 s to acquire.

All figures show a good resolution regarding the smaller vessels, though in figure 5.3 - 5.6 a considerably strong fat-shift is observable. In figure 5.7 and 5.8 the pulsatile flow of the arteries is observable as well as a contamination with venous blood from the distal body region.

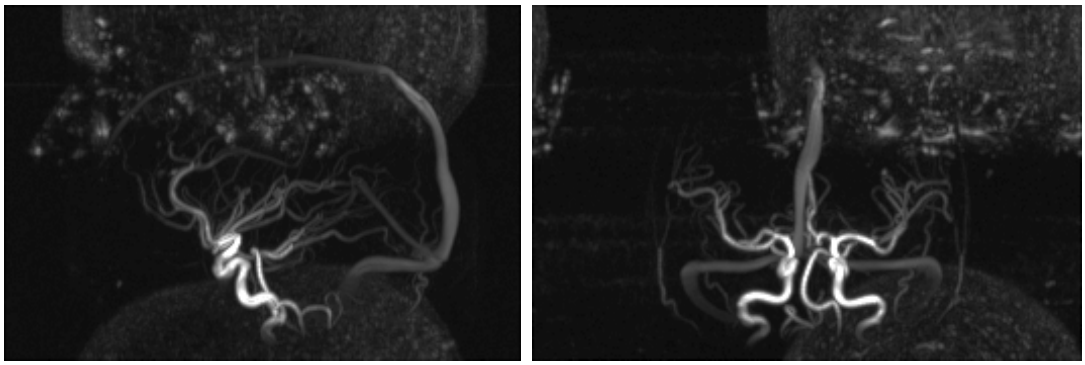

(a) sagittal MIP (b) coronary MIP

Figure 5.4. Depiction of sagittal and coronary MIP of a PCA angiography of the head

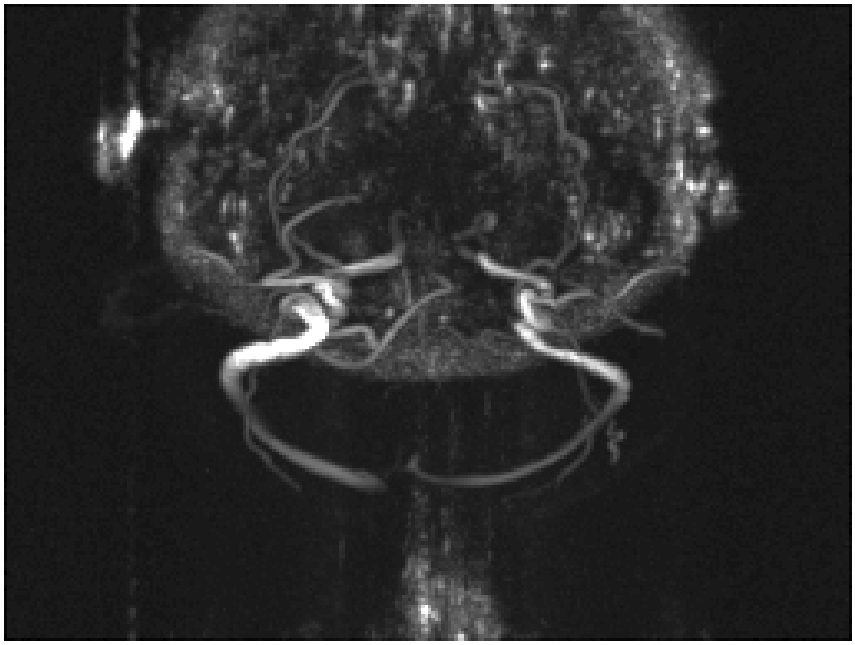

Figure 5.5. Depiction of transversal MIP of a PCA angiography of the carotids

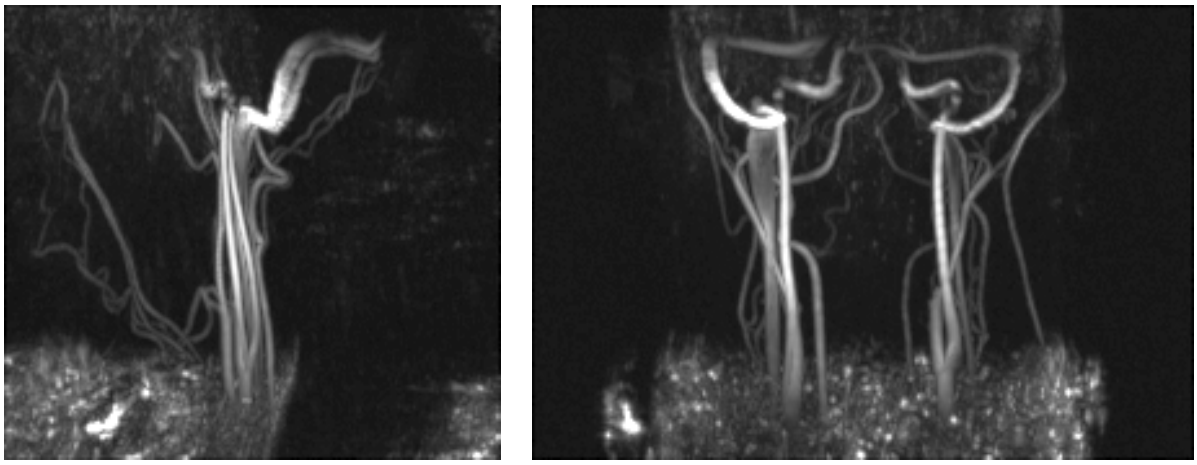

(a) sagittal MIP (b) coronary MIP

Figure 5.6. Depiction of sagittal and coronary MIP of a PCA angiography of the carotids

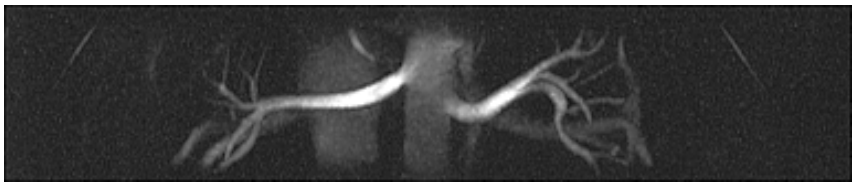

Figure 5.7. Depiction of coronal MIP of a PCA angiography of the renal vessels

5.1.3 Cardiac-gated turbo-spin-echo

The cardiac-gated TSE is applied to the upper leg of the body only, but performed with different cardiac trigger delays to depict the venous and the arterial vessels separately. The venous flow weighted image is depicted in figure 5.9. Image parameters were FOV $400 \times 400 \times 72mm$, image matrix $384 \times 384 \times 72$, flip angle $\alpha = 135°$, cardiac trigger delays $230ms$ and $120ms$ and an acquisition time of 23 min 58 s.

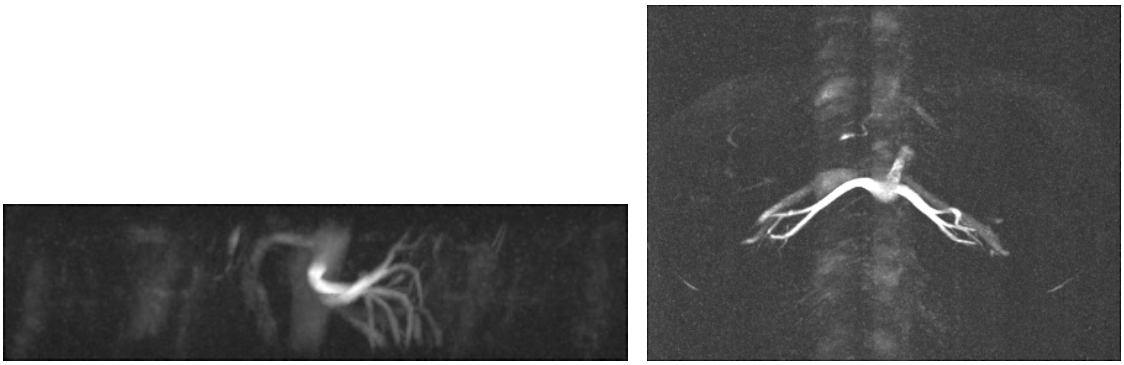

(a) sagittal MIP (b) transversal MIP

Figure 5.8. Depiction of sagittal and transversal MIP of a PCA angiography of the renal vessels

The arterial flow weighted image is shown in figure 5.10. Image parameters are FOV $393 \times 370 \times 96mm$, image matrix $340 \times 320 \times 96$, flip angle $\alpha = 135°$, cardiac trigger delays $280ms$ and $0ms$ and an acquisition time of $18m$ $56s$. Due to the great coverage of the body further views would only show a mixture of both upper legs.

5.1.4 Spin labeling with bSSFP readout (TrueFISP)

The spin labeling technique was developed to image the renal vessels, which are usually moving due to respiration. The images are acquired using 1D MR navigator based gating in combination with ECG-triggering in the first set and respiratory gating in the second. Additionally the sequence was applied to the head/neck region using ECG-triggering solely.
For navigator-gating and ECG-triggering only the transversal MIP of the full slab is depicted figure 5.11. The sagittal and coronal MIPs would only show

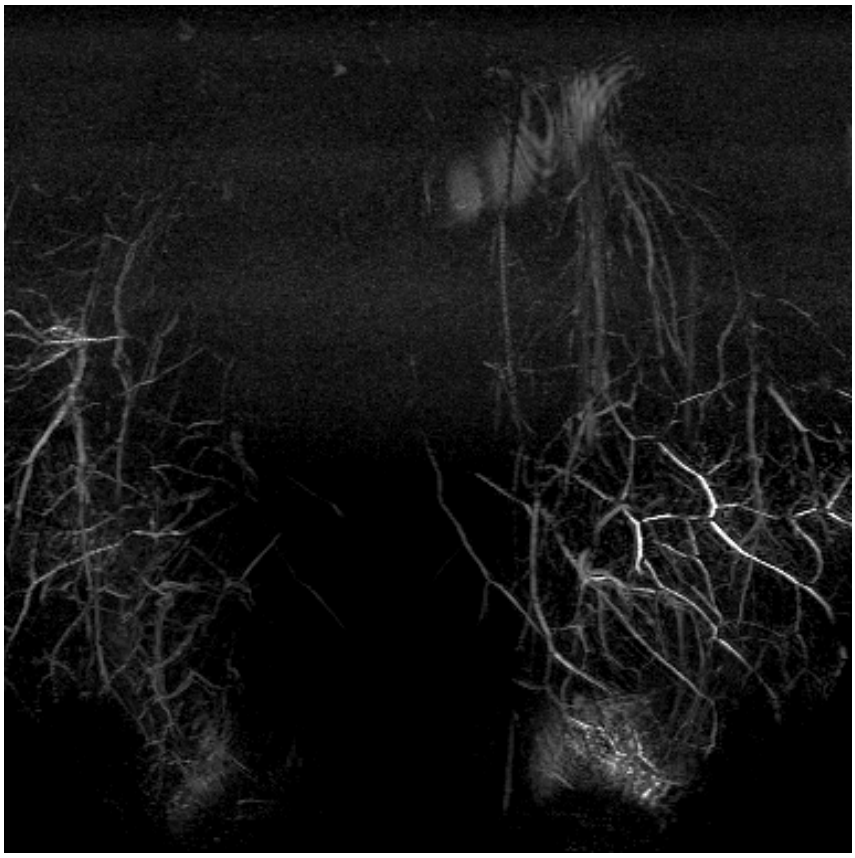

Figure 5.9. Depiction of coronal MIP of a cardiac-gated TSE angiography of the femoral venous vessels

the surrounding fat tissue and are excluded. To compensate for this effect a mask was applied to eliminate the surrounding tissue. The corresponding results are depicted in figure 5.12 and 5.13. The sequence parameters were FOV $272 \times 340 \times 51.2mm$, image matrix $320 \times 400 \times 64$, flip angle $\alpha = 90°$, inversion time of the imaging slab $TI_1 = 1200ms$ and TI of the inversion slab distal to the first $TI_2 = 800ms$ with a total acquisition time of 6 min 54 s. The

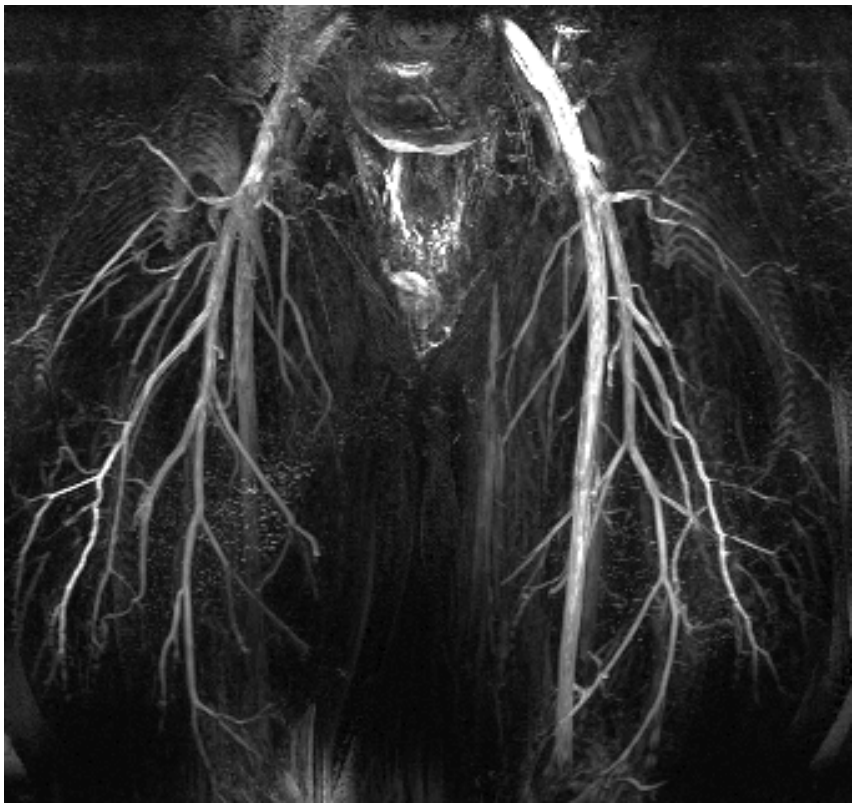

Figure 5.10. Depiction of coronal MIP of a cardiac-gated TSE angiography of the femoral arterial vessels

second set of images depicts the renal vessels using a respiratory gating with a respiratory belt. The resulting MIPs of the full image slab in transversal direction is displayed in figure 5.14. In order to improve the contrast the region of the vessels was cropped. The results are displayed in figure 5.15 and 5.16. The sequence parameters were FOV $240 \times 320 \times 70.4mm$, image matrix $192 \times 256 \times 64$, flip angle $\alpha = 90°$, inversion time of the imaging slab $TI_1 = 1200ms$ and inversion time of the second inversion slab distal

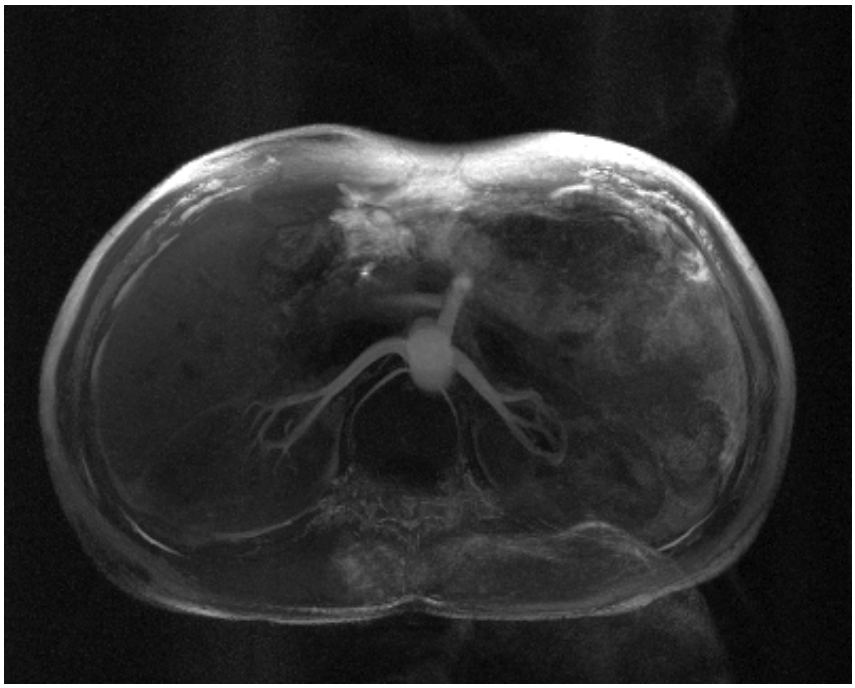

Figure 5.11. Depiction of transversal MIP of a navigator-gated ECG-triggered TrueFISP angiography of the renal vessels

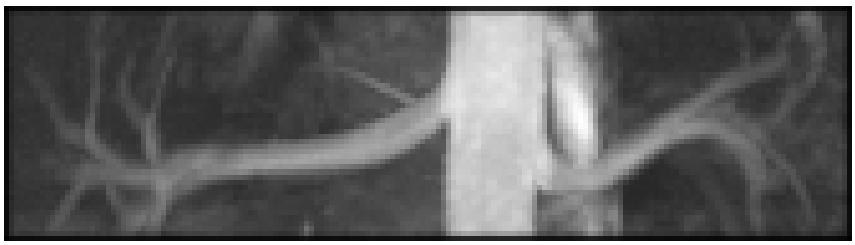

Figure 5.12. Depiction of coronal MIP of a navigator-gated ECG-triggered TrueFISP angiography of the renal vessels with mask applied

to the first $TI_2 = 800ms$ with an acquisition time of 7 min 4 s. Finally, the TrueFISP sequence was applied to image the neck part together with the

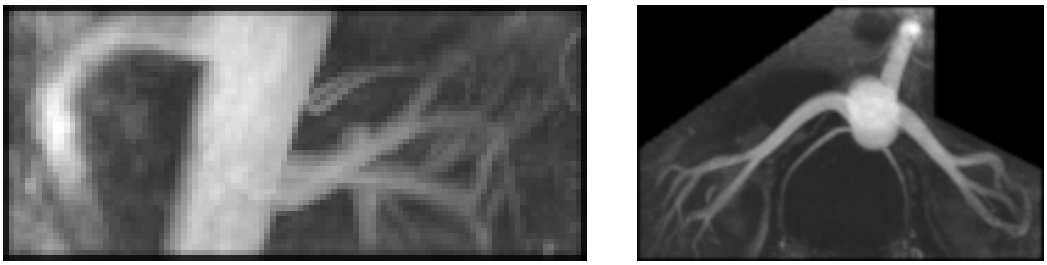

(a) sagittal MIP (b) transversal MIP

Figure 5.13. Depiction of sagittal and transversal MIP of a navigator-gated ECG-triggered TrueFISP angiography of the renal vessels with mask applied

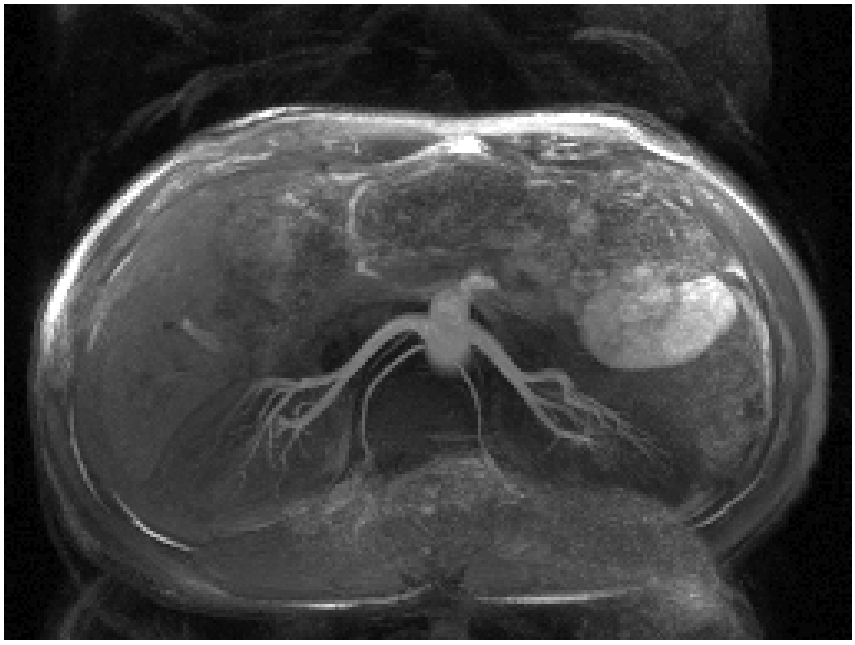

Figure 5.14. Depiction of transversal MIP of a respiratory-gated TrueFISP angiography of the renal vessels

carotid arteries.

The sequence parameters were FOV $256 \times 285 \times 79.2mm$, image matrix

Figure 5.15. Depiction of coronal MIP of a respiratory-gated TrueFISP angiography of the renal vessels with mask applied

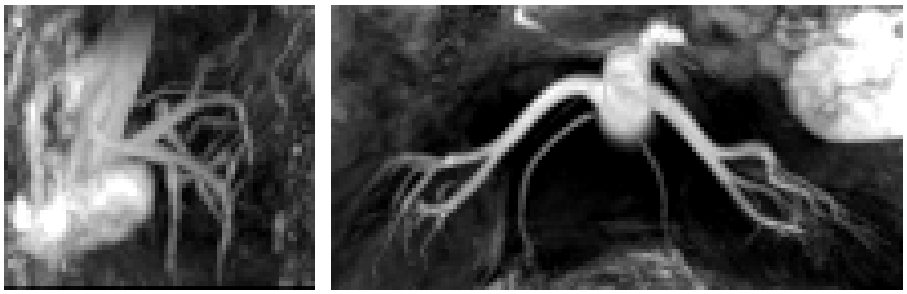

(a) sagittal MIP (b) transversal MIP

Figure 5.16. Depiction of sagittal and transversal MIP of a respiratory-gated TrueFISP angiography of the renal vessels with mask applied

$288 \times 320 \times 88$, flip angle $\alpha = 90°$, inversion time of the imaging slab $TI_1 = 1800ms$ and inversion time of the second inversion slab distal to the first $TI_2 = 800ms$ with an acquisition time of 6 min 12 s.

Given these results retrospective undersampling is not applied to every modality depicted here. The undersampling and advanced reconstruction

was applied to respiratory-gated and navigator-gated TrueFISP, to both cardiac-gated TSEs, to the PCA of the head and kidneys and to TOF data.

5.2 Image reconstruction results

For all corresponding data presented in section 5.1 undersampling with an equidistant sampling pattern and a random sampling pattern was performed. Image reconstruction was carried out with the four different reconstruction algorithms described in chapter 3.

5.2.1 Navigator-gated TrueFISP

The results of retrospective undersampling of navigator-gated ECG-triggered TrueFISP using a 3×3 pattern with a ACS block of 24×12 are shown in figure 5.17 *b*. The corresponding acceleration factors are $R = 8.01$ for equidistant unsersampling and $R = 8$ for random undersampling using a 24×8 ACS block (figure 5.18 *b*).

5.2.2 Respiratory-gated TrueFISP

The results for retrospective undersampling of respiratory-gated TrueFISP using a 3×3 subsampling pattern with a ACS block of 24×12 are shown in figure 5.19 *b*. The corresponding acceleration factor $R = 7.25$ for equidistant unsersampling and $R = 8$ for random undersampling using a 24×8 ACS block (figure 5.20 *b*).

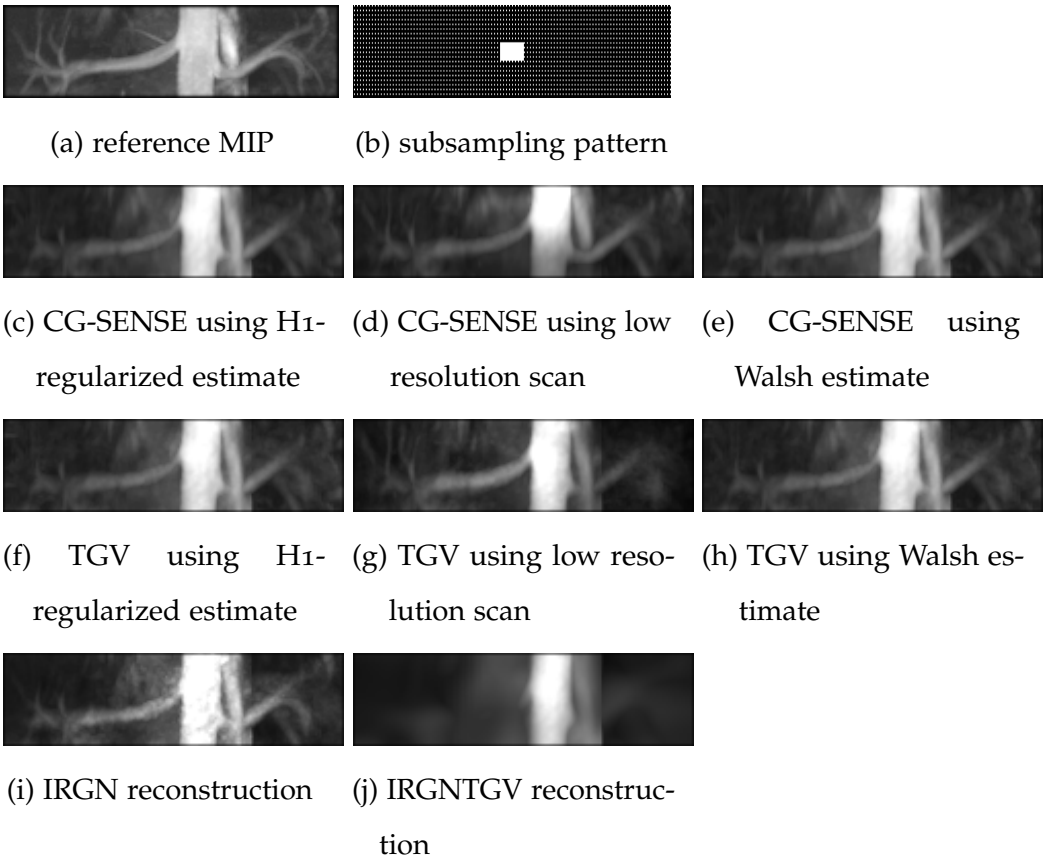

(a) reference MIP (b) subsampling pattern

(c) CG-SENSE using H1-regularized estimate (d) CG-SENSE using low resolution scan (e) CG-SENSE using Walsh estimate

(f) TGV using H1-regularized estimate (g) TGV using low resolution scan (h) TGV using Walsh estimate

(i) IRGN reconstruction (j) IRGNTGV reconstruction

Figure 5.17. Depiction of all reconstruction methods for equidistant subsampling for navigator-gated ECG-triggered TrueFISP data using a 3×3-pattern with ACS-block of 24×12 for a total acceleration factor of $R = 8.01$. In the top row the original images are displayed on the left, while in the middle the undersampling pattern used. In the second row the CG-Sense reconstruction, with H1-regularization of the coil-sensitivities in the left column, coil-sensitivity estimation from low-resolution scan in the middle column and with "Walsh"-estimation in the right column. The third row shows the TGV reconstructions using the same coil-estimations like for CG-Sense. The fourth left row shows the IRGN reconstruction using Tikhonov regularization and in the middle IRGNTGV reconstruction.

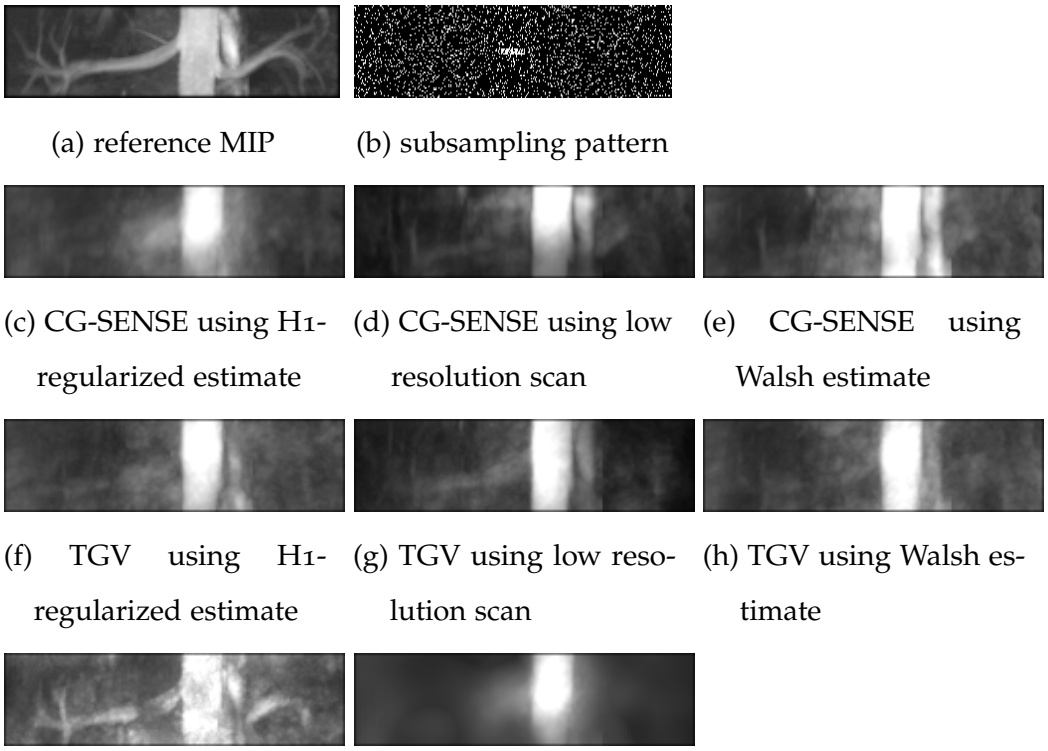

(a) reference MIP (b) subsampling pattern

(c) CG-SENSE using H1-regularized estimate (d) CG-SENSE using low resolution scan (e) CG-SENSE using Walsh estimate

(f) TGV using H1-regularized estimate (g) TGV using low resolution scan (h) TGV using Walsh estimate

(i) IRGN reconstruction (j) IRGNTGV reconstruction

Figure 5.18. Depiction of all reconstruction methods for random subsampling for navigator-gated ECG-triggered TrueFISP data using a random-pattern with ACS-block of 24×8 for a total acceleration factor of $R = 8$. In the top row the original images are displayed on the left, while in the middle the undersampling pattern used. In the second row the CG-Sense reconstruction, with H1-regularization of the coil-sensitivities in the left column, coil-sensitivity estimation from low-resolution scan in the middle column and "Walsh"-estimation in the right column. The third row shows the TGV reconstructions using the same coil-estimations like for CG-Sense. The fourth left row shows the IRGN reconstruction using Tikhonov regularization and in the middle IRGNTGV reconstruction.

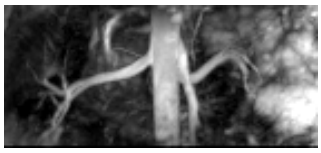

(a) reference MIP

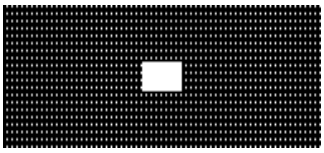

(b) subsampling pattern

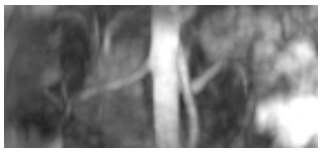

(c) CG-SENSE using H1-regularized estimate

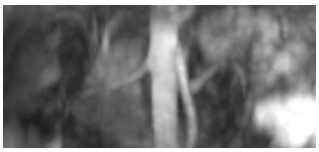

(d) CG-SENSE using low resolution scan

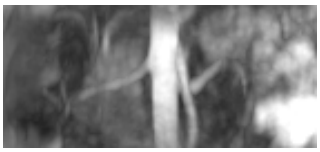

(e) CG-SENSE using Walsh estimate

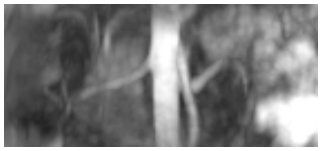

(f) TGV using H1-regularized estimate

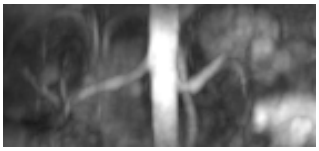

(g) TGV using low resolution scan

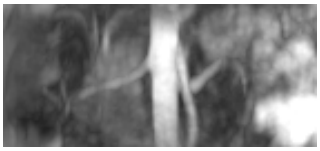

(h) TGV using Walsh estimate

(i) IRGN reconstruction

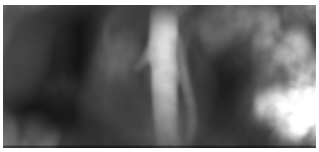

(j) IRGNTGV reconstruction

Figure 5.19. Depiction of all reconstruction methods for equidistant subsampling for respiratory-gated TrueFISP data using a 3×3-pattern with ACS-block of 24×12 for a total acceleration factor of $R = 7.25$. In the top row the original images are displayed on the left, while in the middle the undersampling pattern used. In the second row the CG-Sense reconstruction, with H1-regularization of the coil-sensitivities in the left column, coil-sensitivity estimation from low-resolution scan in the middle column and with "Walsh"-estimation in the right column. The third row shows the TGV reconstructions using the same coil-estimations like for CG-Sense. The fourth row shows the IRGN reconstruction using Tikhonov regularization (left) and in the middle IRGNTGV reconstruction.

(a) reference MIP

(b) subsampling pattern

(c) CG-SENSE using H1-regularized estimate

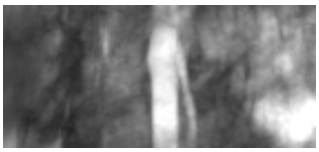

(d) CG-SENSE using low resolution scan

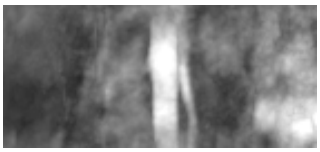

(e) CG-SENSE using Walsh estimate

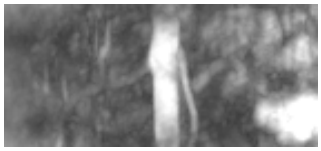

(f) TGV using H1-regularized estimate

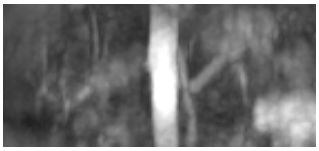

(g) TGV using low resolution scan

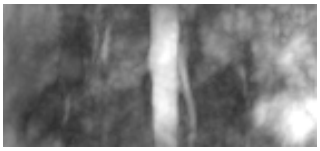

(h) TGV using Walsh estimate

(i) IRGN reconstruction

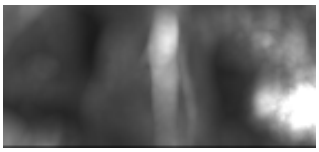

(j) IRGNTGV reconstruction

Figure 5.20. Depiction of all reconstruction methods for random subsampling for respiratory-gated TrueFISP data using a random-pattern with ACS-block of 24×8 for a total acceleration factor of $R = 8$. In the top row the original images are displayed on the left, while in the middle the undersampling pattern used. In the second row the CG-Sense reconstruction, with H1-regularization of the coil-sensitivities in the left column, coil-sensitivity estimation from low-resolution scan in the middle column and with "Walsh"-estimation in the right column. The third row shows the TGV reconstructions using the same coil-estimations like for CG-Sense. The fourth row shows the IRGN reconstruction using Tikhonov regularization (left) and in the middle IRGNTGV reconstruction.

5.2.3 Renal PCA

Figures 5.21 and 5.22 show the results of retrospective undersampling and image reconstruction of renal PCA data. In figure 5.21 an equidistant 3×3 pattern with a ACS block of 24×12 was used (figure 5.21 b) which results in an acceleration factor of $R = 7.75$. The pattern for random undersampling uses a ACS block of 24×8(depicted in figure 5.22 *b*) which yields an acceleration factor of $R = 8$.

5.2.4 Cerebral PCA

In figures 5.23 - 5.26 the results of image reconstruction for cerebral angiography are depicted. In figures 5.23 and 5.24 the results for equidistant subsampling are shown using a 3×3 pattern with an ACS block of 24×12. This results in a total acceleration factor of $R = 8$. In figures 5.25 and 5.26 the results for random subsampling are shown with an ACS block of 24×12. This results in a total acceleration factor of $R = 8$.

5.2.5 TOF

The results for image reconstruction of retrospective undersampled TOF angiography are shown in figure 5.27 - 5.30. Figures 5.27 and 5.28 show the image reconstruction results using a random undersampling pattern. The equidistant pattern uses a 24×12 ACS block and the random pattern a 24×8 ACS block resulting in a acceleration factor of $R = 7.5$ and $R = 8$ respectively.

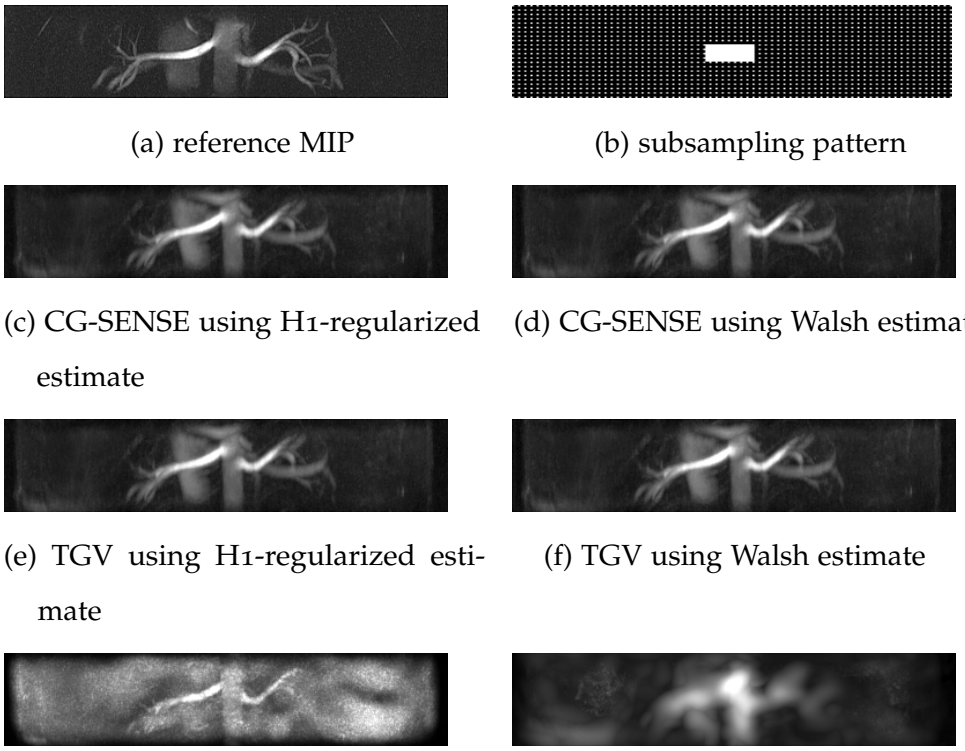

(a) reference MIP

(b) subsampling pattern

(c) CG-SENSE using H1-regularized estimate

(d) CG-SENSE using Walsh estimate

(e) TGV using H1-regularized estimate

(f) TGV using Walsh estimate

(g) IRGN reconstruction

(h) IRGNTGV reconstruction

Figure 5.21. Depiction of all reconstruction methods for equidistant subsampling for renal PCA data using a equidistant-pattern with ACS-block of 24×12 for a total acceleration factor of $R = 7.75$. In the top row the original images are displayed on the left, while the undersampling pattern used in the middle. In the second row the CG-Sense reconstruction, with H1-regularization of the coil-sensitivities in the left column and "Walsh"-estimation in the right column. The third row shows the TGV reconstructions using the same coil-estimates like for CG-Sense. The fourth row shows the IRGN reconstruction using Tikhonov regularization (left) and on the right IRGNTGV reconstruction.

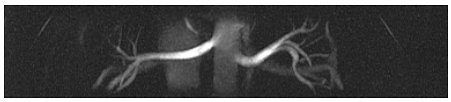

(a) reference MIP

(b) subsampling pattern

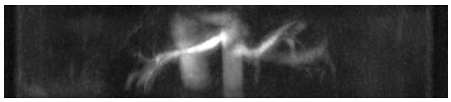

(c) CG-SENSE using H1-regularized estimate

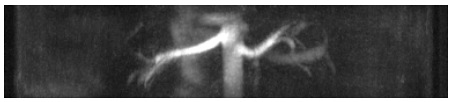

(d) CG-SENSE using Walsh estimate

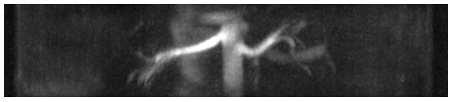

(e) TGV using H1-regularized estimate

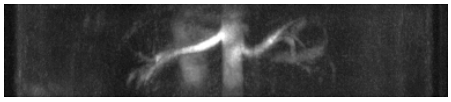

(f) TGV using Walsh estimate

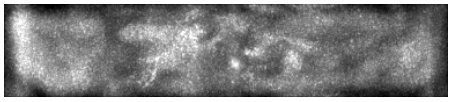

(g) IRGN reconstruction

(h) IRGNTGV reconstruction

Figure 5.22. Depiction of all reconstruction methods for random subsampling for renal PCA data using a random-pattern with ACS-block of 24×8 for a total acceleration factor of $R = 8$. In the top row the original images are displayed on the left, while the undersampling pattern used in the middle. In the second row the CG-Sense reconstruction, with H1-regularization of the coil-sensitivities in the left column and with "Walsh"-estimation in the right column. The third row shows the TGV reconstructions using the same coil-estimations like for CG-Sense. The fourth row shows the IRGN reconstruction using Tikhonov regularization (left) and in the middle IRGNTGV reconstruction.

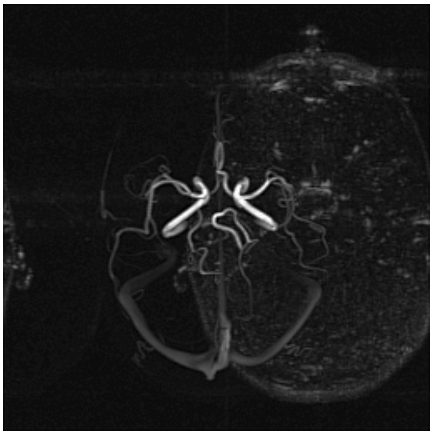

(a) reference MIP

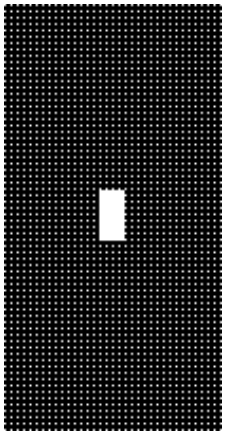

(b) subsampling pattern

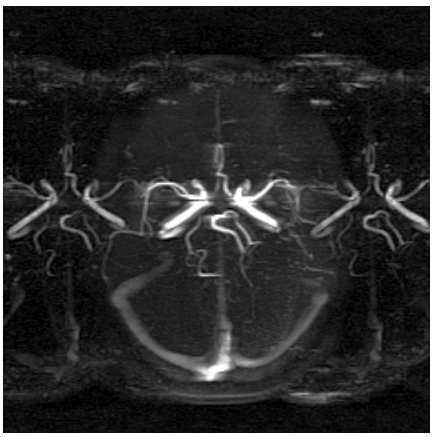

(c) CG-SENSE using H1-regularized estimate

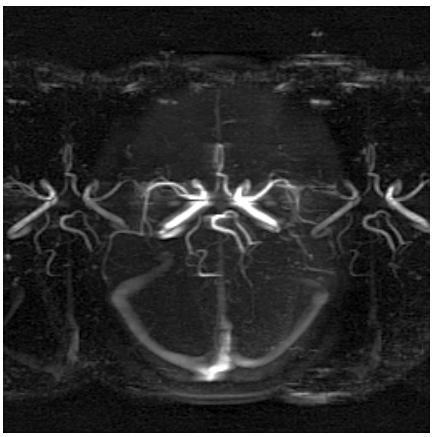

(d) CG-SENSE using Walsh estimate

Figure 5.23. Depiction of the first set of reconstruction methods for equidistant subsampling for cerebral PCA data using a equidistant-pattern with ACS-block of 24×12 for a total acceleration factor of $R = 8$. In the top row the original images are displayed on the left, while the undersampling pattern used on the right. In the second row the CG-Sense reconstruction, with H1-regularization of the coil-sensitivities in the left column and with "Walsh"-estimation in the right.

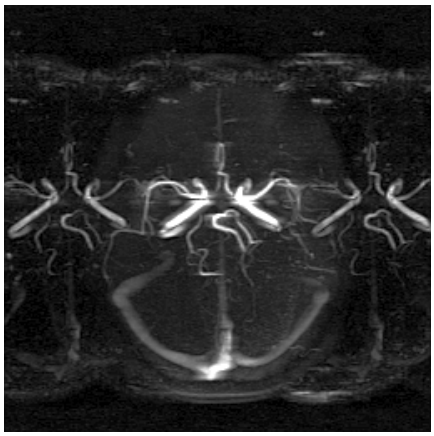

(a) TGV using H1-regularized estimate

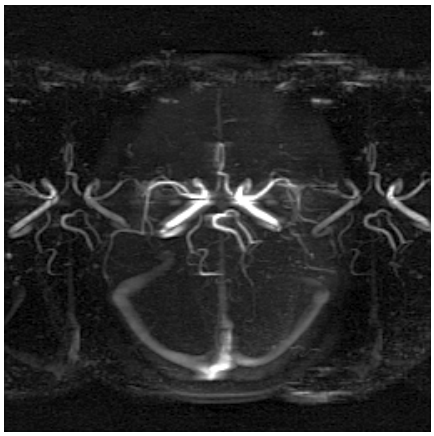

(b) TGV using Walsh estimate

(c) IRGN reconstruction

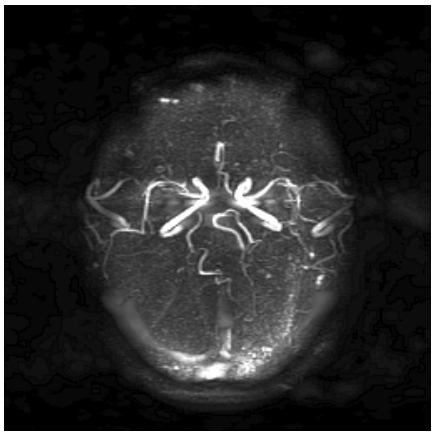

(d) IRGNTGV reconstruction

Figure 5.24. Depiction of the second part of reconstruction methods on equidistant subsampling for cerebral PCA data using a equidistant-pattern with ACS-block of 24×12 for a total acceleration factor of $R = 8$. The top row shows the TGV reconstructions with H1-regularization of the coil-sensitivities on the left and with the Walsh coil-estimate on the right. The bottom row shows the IRGN reconstruction using Tikhonov regularization (left) and on the right IRGNTGV reconstruction.

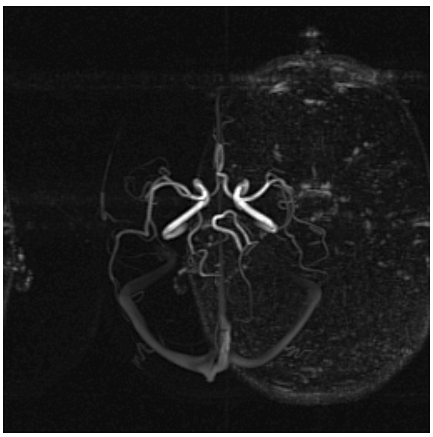

(a) reference MIP

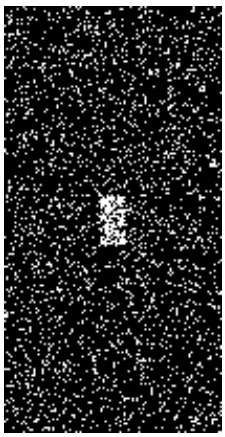

(b) subsampling pattern

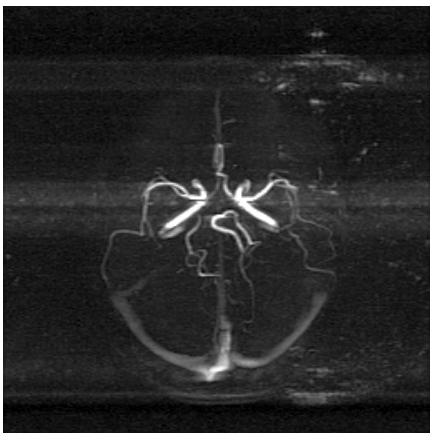

(c) CG-SENSE using H1-regularized estimate

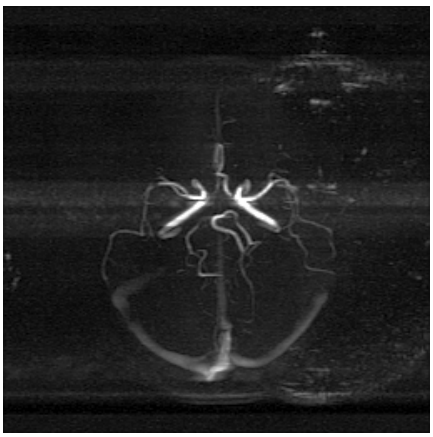

(d) CG-SENSE using Walsh estimate

Figure 5.25. Depiction of the first set of reconstruction methods for random subsampling for cerebral PCA data using a random-pattern with ACS-block of 24×8 for a total acceleration factor of $R = 8$. In the top row the original image are displayed on the left, while the undersampling pattern used on the right. In the second row the CG-Sense reconstruction with H1-regularization of the coil-sensitivities in the left column and with "Walsh"-estimation in the right.

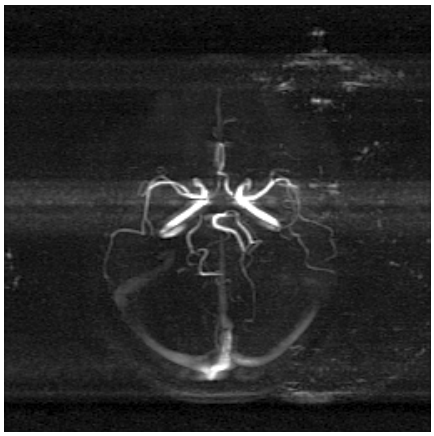

(a) TGV using H1-regularized estimate

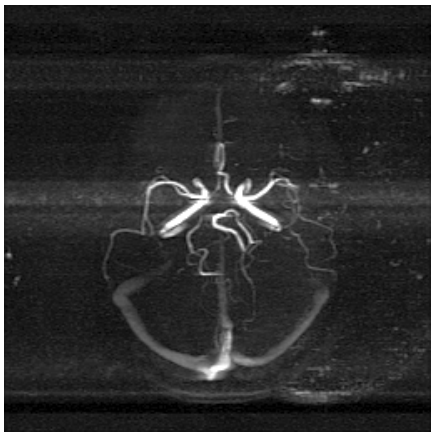

(b) TGV using Walsh estimate

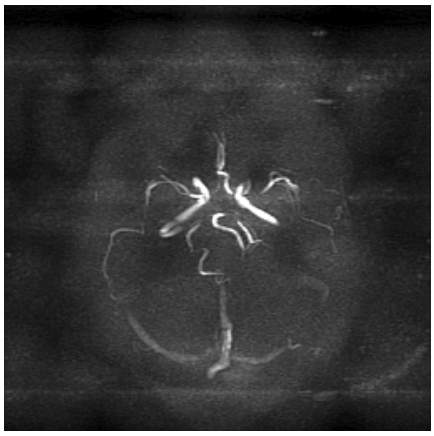

(c) IRGN reconstruction

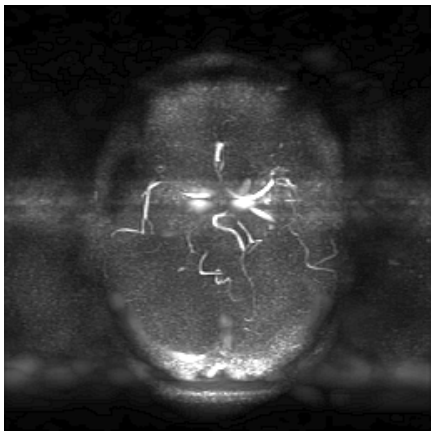

(d) IRGNTGV reconstruction

Figure 5.26. Depiction of the second part of reconstruction methods for random subsampling for cerebral PCA data using a random-pattern with ACS-block of 24×8 for a total acceleration factor of $R = 8$. The top row shows the TGV reconstructions with H1-regularization of the coil-sensitivities on the left and in the right column with the "Walsh" coil-estimate. The bottom row shows the IRGN reconstruction using Tikhonov regularization (left) and on the right IRGNTGV reconstruction.

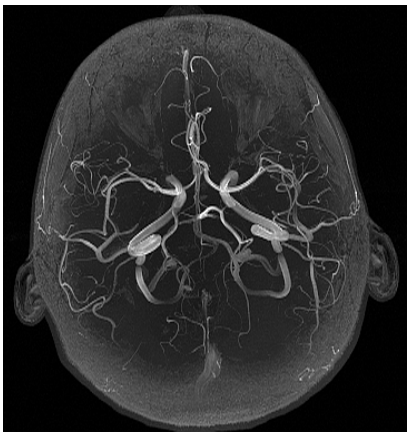

(a) reference MIP

(b) subsampling pattern

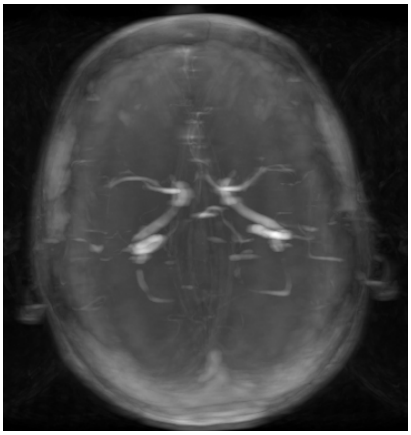

(c) CG-SENSE using H1-regularized estimate

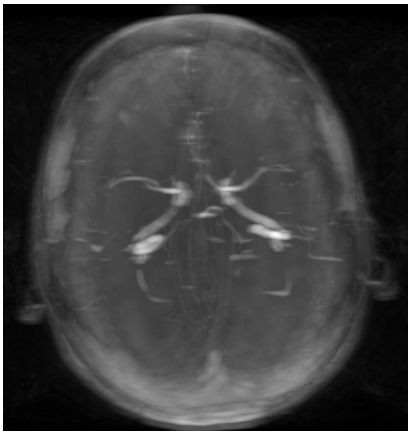

(d) CG-SENSE using Walsh estimate

Figure 5.27. Depiction of the first part of reconstruction methods for equidistant subsampling for cerebral TOF data using a equidistant-pattern with ACS-block of 24×12 for a total acceleration factor of $R = 7.5$. In the top row the original image are displayed on the left, while the undersampling pattern used on the right. In the second row the CG-Sense reconstruction, with H1-regularization of the coil-sensitivities in the left column and with "Walsh"-estimation in the right column.

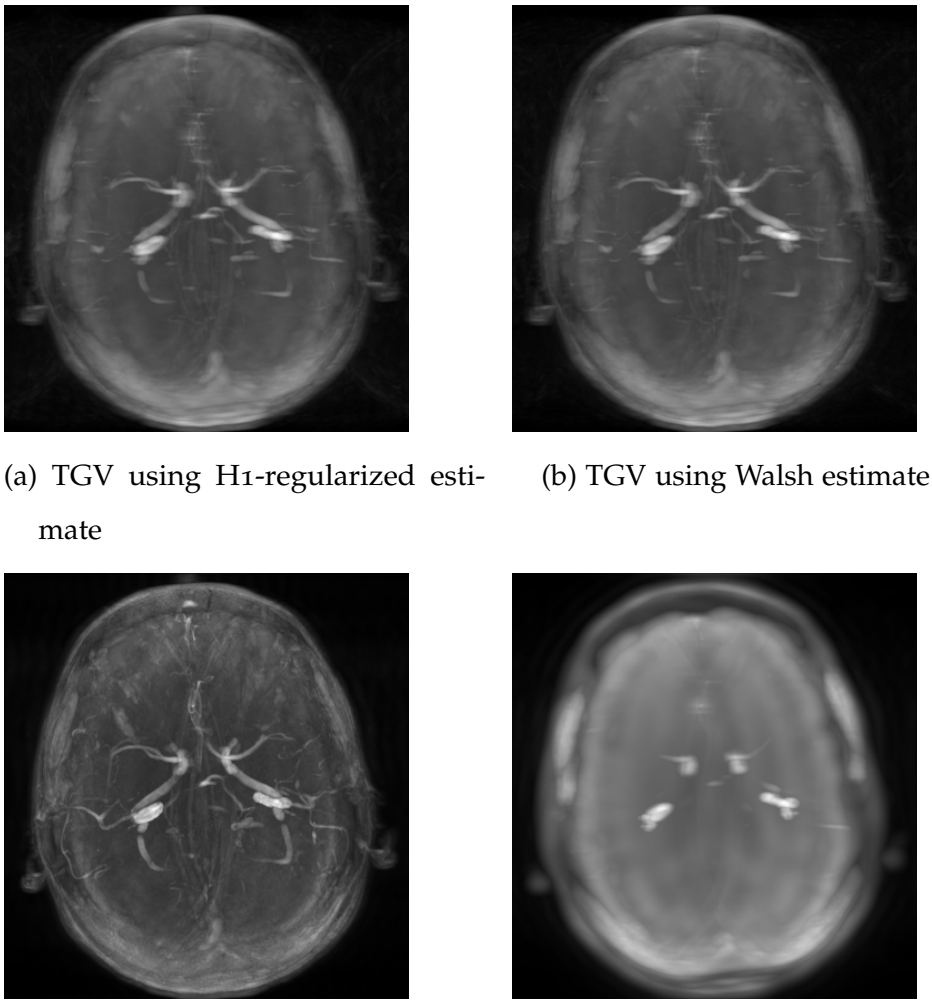

(a) TGV using H1-regularized estimate

(b) TGV using Walsh estimate

(c) IRGN reconstruction

(d) IRGNTGV reconstruction

Figure 5.28. Depiction of the second part of reconstruction methods for equidistant subsampling for cerebral TOF data using a equidistant-pattern with ACS-block of 24×12 for a total acceleration factor of $R = 7.5$. The top row shows the TGV reconstruction with H1-regularization of the coil-sensitivities on the left and with the Walsh coil-estimate on the right. The bottom row shows on the left IRGN reconstruction using Tikhonov regularization (left) and on the right IRGNTGV reconstruction.

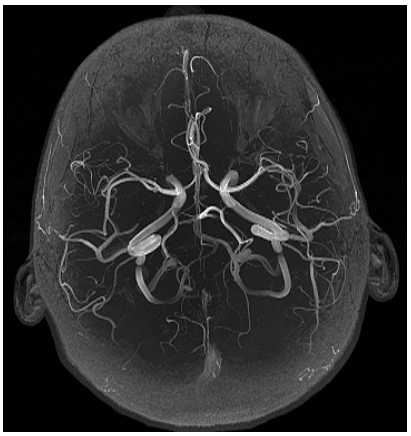

(a) reference MIP

(b) subsampling pattern

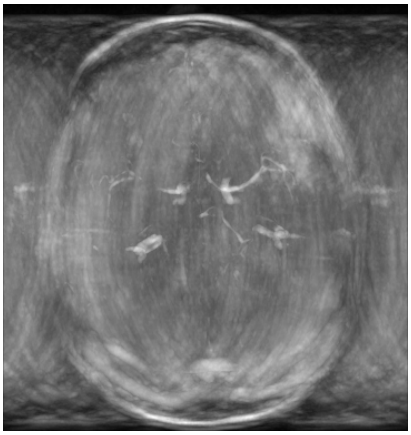

(c) CG-SENSE using H1-regularized estimate

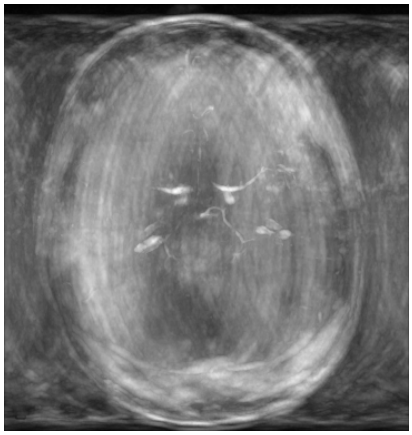

(d) CG-SENSE using Walsh estimate

Figure 5.29. Depiction of the first set of reconstruction methods for random subsampling for cerebral TOF data using a random-pattern with ACS-block of 24×8 for a total acceleration factor of $R = 8$. In the top row the original images are displayed on the left, while the undersampling pattern used on the right. In the second row the CG-Sense reconstruction with H1-regularization of the coil-sensitivities in the left column and with "Walsh"-estimation in the right column.

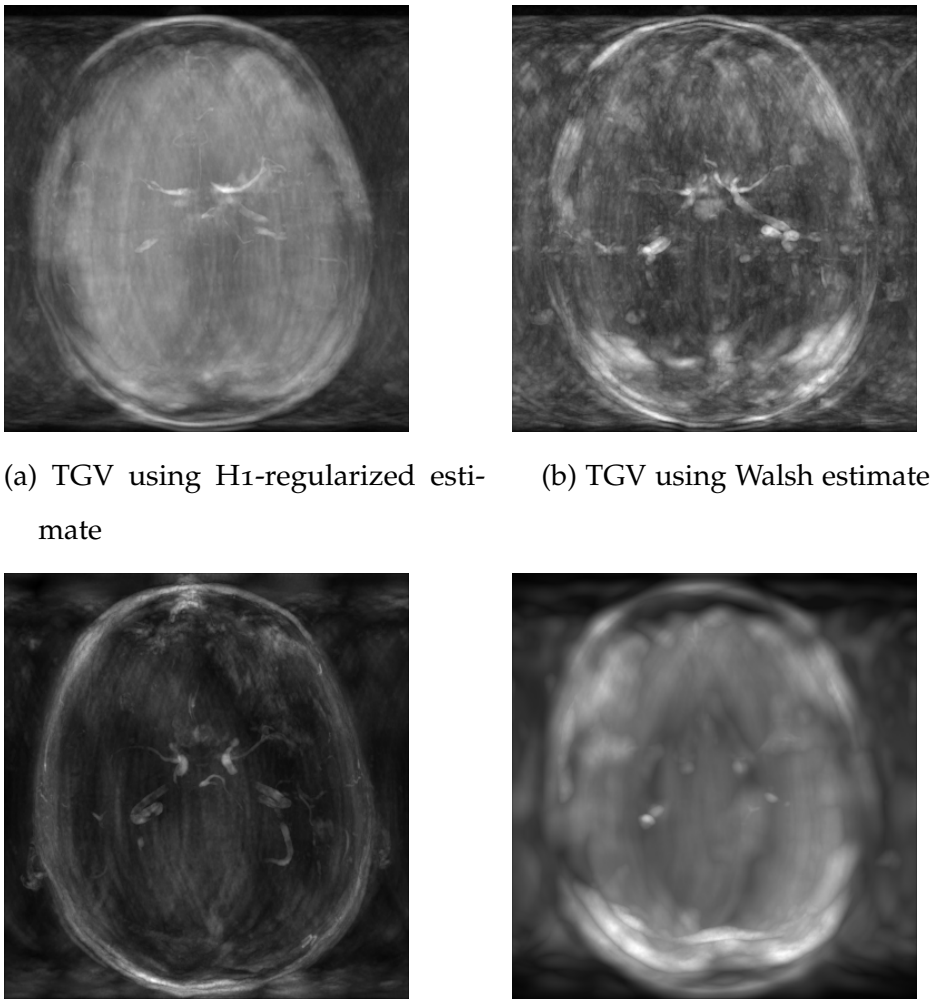

(a) TGV using H1-regularized estimate

(b) TGV using Walsh estimate

(c) IRGN reconstruction

(d) IRGNTGV reconstruction

Figure 5.30. Depiction of the second part of reconstruction methods for random subsampling for cerebral TOF data using a random-pattern with ACS-block of 24×8 for a total acceleration factor of $R = 8$. The top row shows the TGV reconstructions with H1-regularization of the coil-sensitivities on the left and on the right with the "Walsh" coil-estimate. The bottom row shows on the left IRGN reconstruction using Tikhonov regularization and on the right IRGNTGV reconstruction

5.2.6 Femoral cardiac-gated TSE

As described in subsection 5.1.3 it is possible to depict venous and arterial angiograms using cardiac-gated TSE. Therefore acceleration is applied to both imaging modalities.

Venous phase triggered

Figures 5.31 - 5.34 show the image reconstruction results of venous phase triggered cardiac-gated TSE. In figure 5.31 and 5.32 the results, using a equidistant subsampling pattern with a 24×12 ACS block and partial Fourier acquisition (set on the scanner) are displayed. The corresponding acceleration factor is $R = 10$. The results using a random pattern are shown in figures 5.33 and 5.34. The ACS block used was 24×8 with partial Fourier acquisition enabled, which results in an acceleration factor of $R = 10$.

Arterial phase triggered

In figures 5.35 - 5.38 the image reconstruction results of arterial phase triggered cardiac-gated TSE are shown. Figures 5.35 and 5.36 display the results of image reconstruction with equidistant undersampling with an ACS block of 24×12 and partial Fourier acquisition (acceleration factor of $R = 10$). The results of image reconstruction using a random sampling pattern with an ACS block of 24×8 and partial Fourier are shown in figures 5.37 and 5.38. The corresponding acceleration factor is $R = 10$.

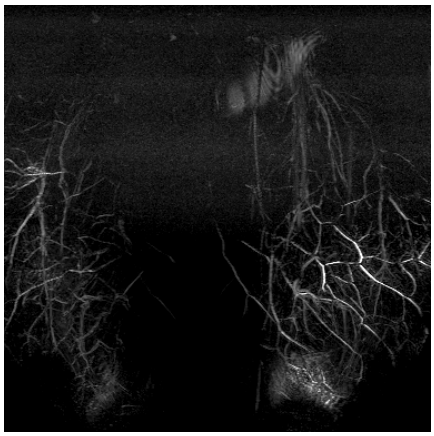

(a) reference MIP

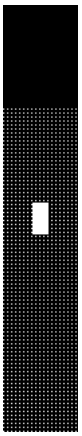

(b) subsampling pattern

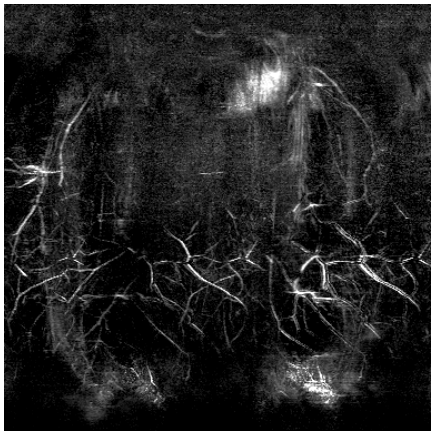

(c) CG-SENSE using H1-regularized estimate

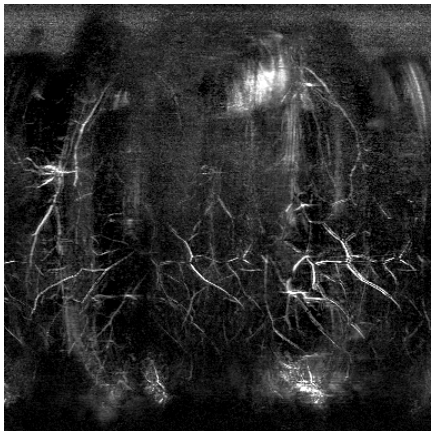

(d) CG-SENSE using Walsh estimate

Figure 5.31. Depiction of the first part of reconstruction methods for equidistant subsampling for cardiac-gated TSE data using an equidistant undersampling-pattern with an ACS-block of 24×12 and partial Fourier acquisition for a total acceleration factor of $R = 10$. Top row shows the original image on the left and the undersampling pattern used on the right. The second row shows the CG-Sense reconstruction with H1-regularization of the coil-sensitivities in the left column and with "Walsh"-estimation in the right column.

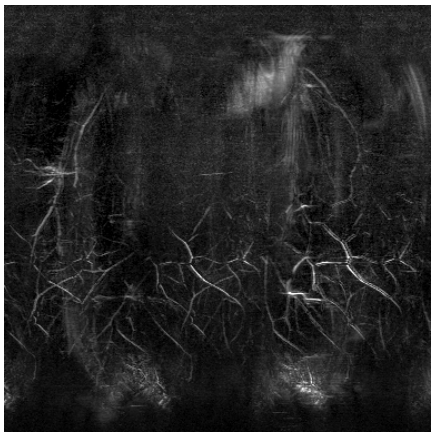

(a) TGV using H1-regularized estimate

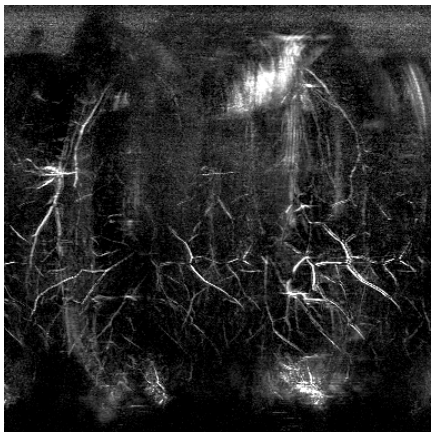

(b) TGV using Walsh estimate

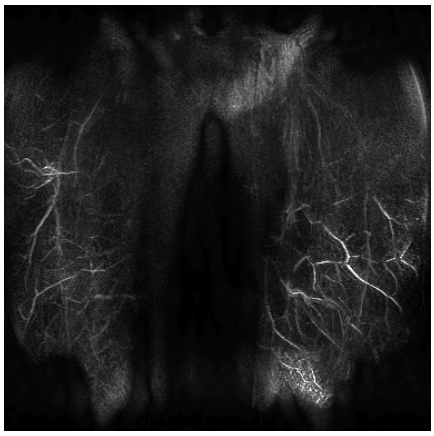

(c) IRGN reconstruction

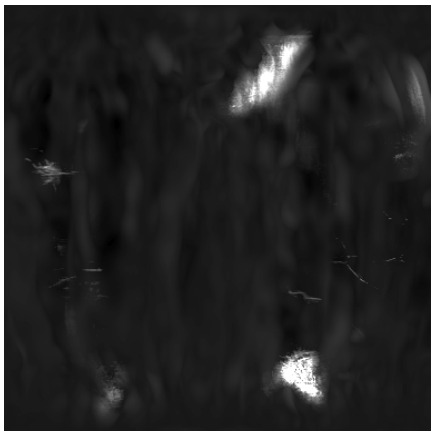

(d) IRGNTGV reconstruction

Figure 5.32. Depiction of the second part of reconstruction methods for equidistant subsampling for cardiac-gated TSE data using an equidistant undersampling-pattern with an ACS-block of 24×12 and partial Fourier acquisition for a total acceleration factor of $R = 10$. Top row shows the TGV reconstructions using the same coil-estimations like for CG-Sense. The second row shows the IRGN reconstruction using Tikhonov regularization (left) and IRGNTGV reconstruction on the right.

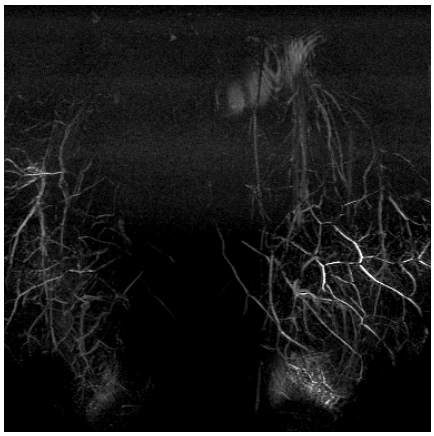

(a) reference MIP

(b) subsampling pattern

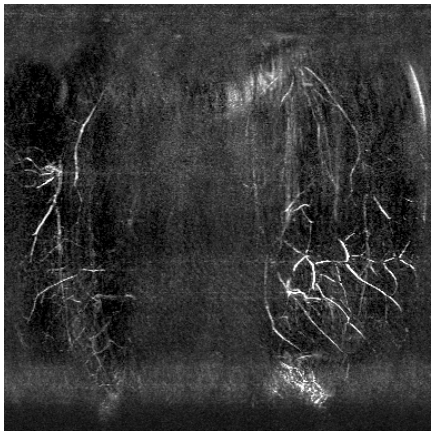

(c) CG-SENSE using H1-regularized estimate

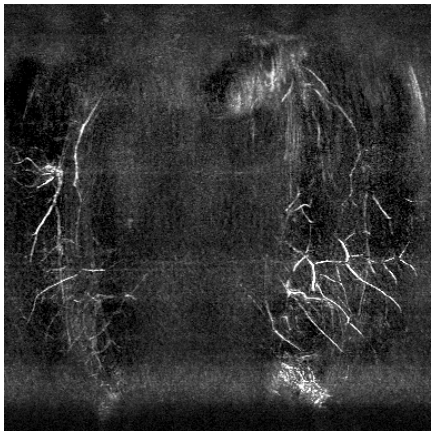

(d) CG-SENSE using Walsh estimate

Figure 5.33. Depiction of the first part of all reconstruction methods for random subsampling for cardiac-gated TSE data using a random undersampling-pattern with an ACS-block of 24×8 and partial Fourier acquisition for a total acceleration factor of 10. Top row shows the original image on the left and the undersampling pattern used on the right. The second row shows the CG-Sense reconstruction, with H1-regularization of the coil-sensitivities in the left column and with "Walsh"-estimation in the right column.

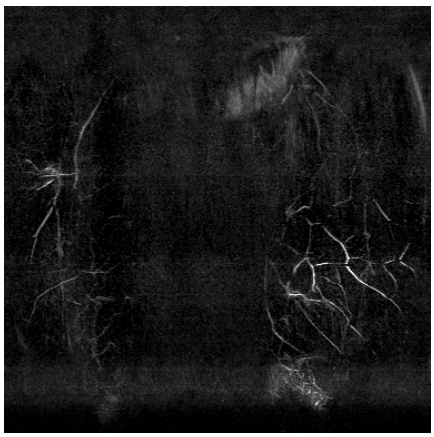

(a) TGV using H1-regularized estimate

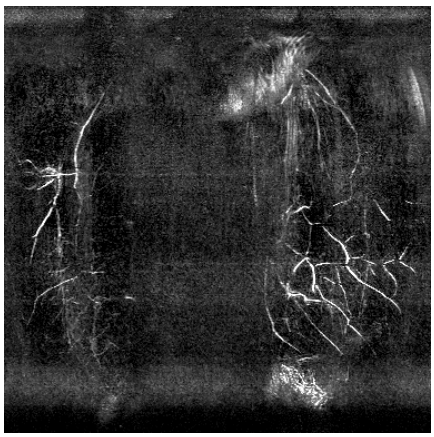

(b) TGV using Walsh estimate

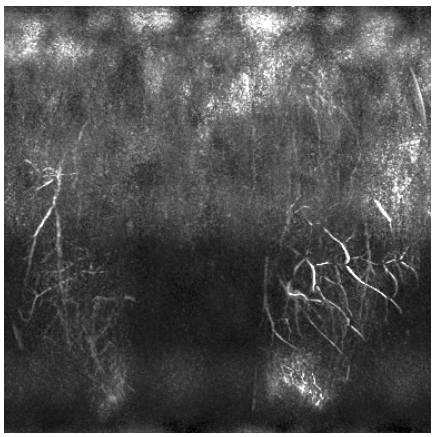

(c) IRGN reconstruction

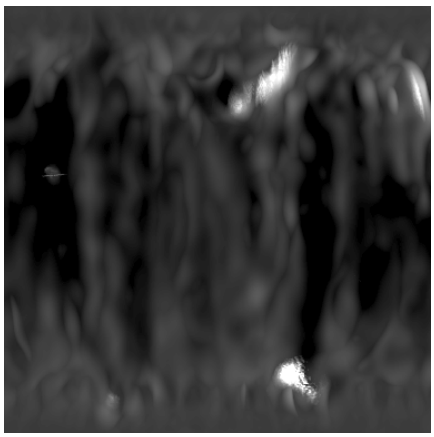

(d) IRGNTGV reconstruction

Figure 5.34. Depiction of the second part of all reconstruction methods for random subsampling for cardiac-gated TSE using a random undersampling-pattern with ACS-block of 24×8 and partial Fourier acquisition for a total acceleration factor of $R = 10$. Top row shows the TGV reconstructions using the same coil-estimations like for CG-Sense. The second row shows the IRGN reconstruction using Tikhonov regularization (left) and on the right IRGNTGV reconstruction.

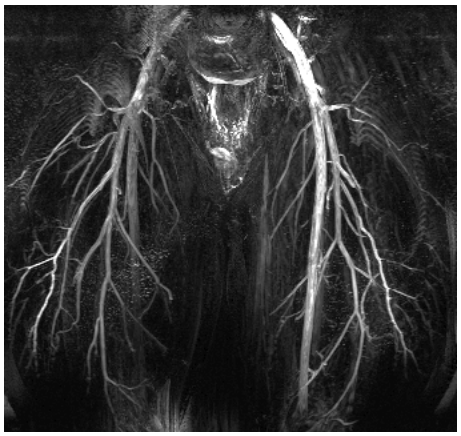

(a) reference MIP

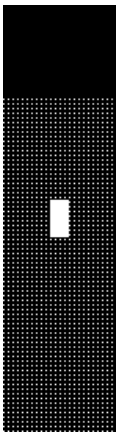

(b) subsampling pattern

(c) CG-SENSE using H1-regularized estimate

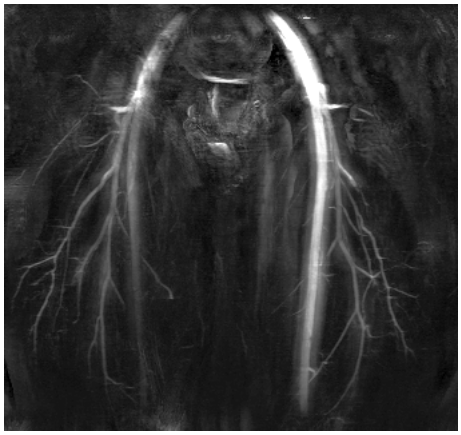

(d) CG-SENSE using Walsh estimate

Figure 5.35. Depiction of the first part of all reconstruction methods for equidistant subsampling for cardiac-gated TSE data using an equidistant undersampling-pattern with an ACS-block of 24×12 for a total acceleration factor of $R = 10$. Top row shows the original image on the left and the undersampling pattern used on the right. The second row shows the CG-Sense reconstruction, with H1-regularization of the coil-sensitivities in the left column and with "Walsh"-estimation in the right column.

(a) TGV using H1-regularized estimate

(b) TGV using Walsh estimate

(c) IRGN reconstruction

(d) IRGNTGV reconstruction

Figure 5.36. Depiction of the second part of all reconstruction methods for equidistant subsampling for cardiac-gated TSE data using an equidistant undersampling-pattern with ACS-block of 24×12 for a total acceleration factor of $R = 10$. Top row shows the TGV reconstructions using the same coil-estimations like for CG-Sense. The second row shows the IRGN reconstruction using Tikhonov regularization (left) and IRGNTGV reconstruction on the right.

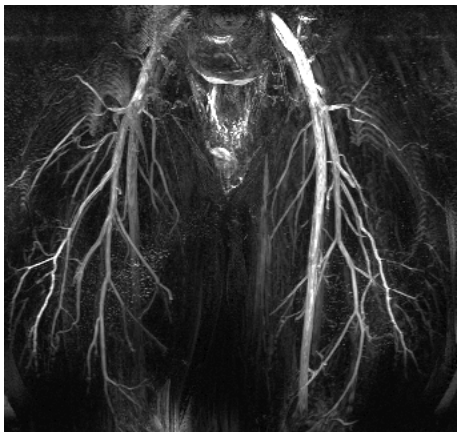

(a) reference MIP

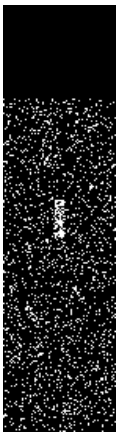

(b) subsampling pattern

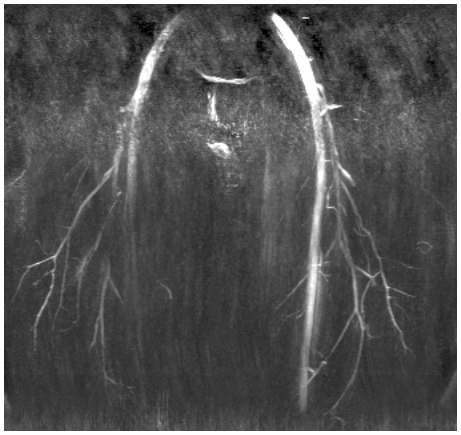

(c) CG-SENSE using H1-regularized estimate

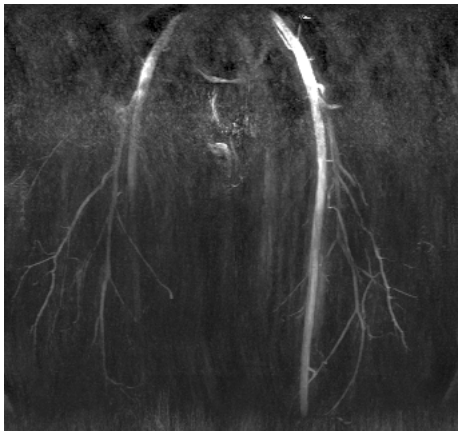

(d) CG-SENSE using Walsh estimate

Figure 5.37. Depiction of the first part of all reconstruction methods for random subsampling for cardiac-gated TSE data using a random undersampling-pattern with an ACS-block of 24×12 for a total acceleration factor of $R = 10$. Top row shows the original image on the left and the undersampling pattern used on the right. The second row shows the CG-Sense reconstruction, with H1-regularization of the coil-sensitivities in the left column and with "Walsh"-estimation in the right column.

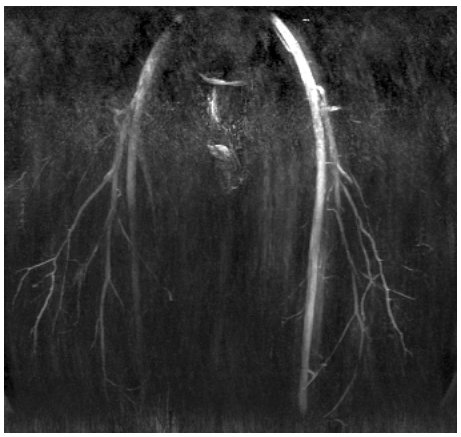

(a) TGV using H1-regularized estimate

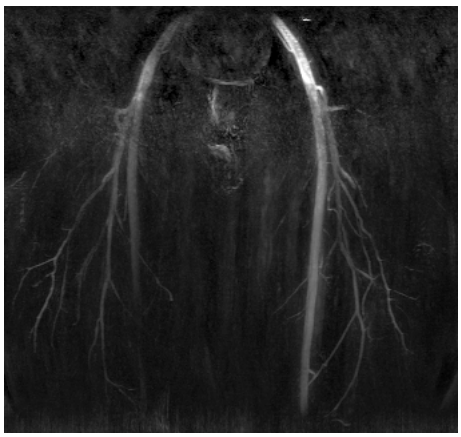

(b) TGV using Walsh estimate

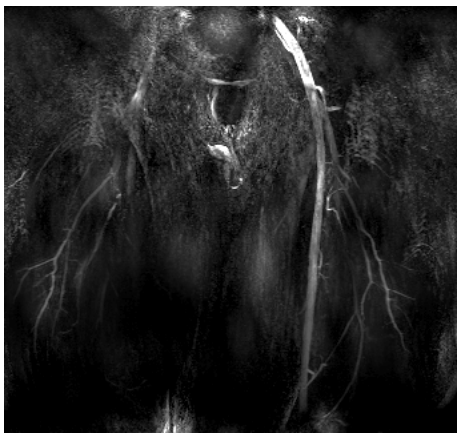

(c) IRGN reconstruction

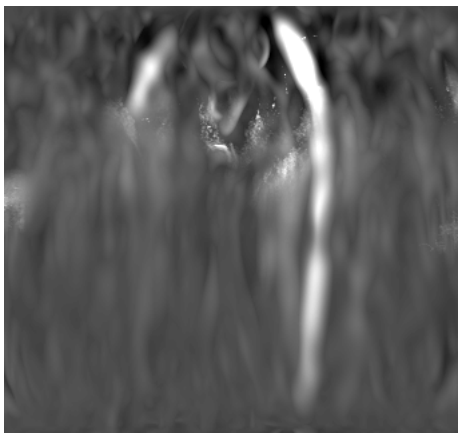

(d) IRGNTGV reconstruction

Figure 5.38. Depiction of the second part of all reconstruction methods for random subsampling for cardiac-gated TSE data using a random undersampling-pattern with an ACS-block of 24×12 for a total acceleration factor of $R = 10$. Top row shows the TGV reconstructions using the same coil-estimations like for CG-Sense. The second row shows the IRGN reconstruction using Tikhonov regularization (left) and IRGNTGV reconstruction on the right.

5.3 Reconstruction times

For comparison of the reconstruction methods the time needed for computation was recorded. Tables 5.1 and 5.2 summarize the computation times for reconstruction and auxiliary computation times. To compute the total reconstruction times, using TGV or CG-Sense, the time for coil estimation has to be added respectively. This times are valid for one time coil-estimation (except TOF) and reconstruction of all image slabs (TrueFISP contain one each, the other four each). The differences for the TrueFISP sequence are due to a different amount of receiver coils.

Sequence	CG-Sense	TGV	IRGN	IRGN-TGV
nav. TrueFISP	1*min* 8.2*s*	1*h* 11*min* 8*s*	1*h* 21*min* 59*s*	3*h* 8*min* 11*s*
resp. TrueFISP	24.24*s*	46*min* 31*s*	53*min* 23*s*	56*min* 47*s*
cerebral PCA	9*min* 24*s*	5*h* 57*min* 49*s*	11*h* 14*min* 3*s*	18*h* 54*min* 21*s*
renal PCA	7*min* 7*s*	4*h* 8*min* 13*s*	5*h* 55*min* 1*s*	7*h* 43*min* 15*s*
cerebral TOF	2*min* 6*s*	5*h* 3*min* 1*s*	5*h* 18*min* 4*s*	15*h* 65*min* 45*s*
venous TSE	8*min* 54.4*s*	16*h* 44*min* 9*s*	17*h* 39*min* 47*s*	1*d* 19*h* 52*min* 58*s*
arterial TSE	9*min* 8.2*s*	12*h* 49*min* 25*s*	19*h* 29*min* 23*s*	1*d* 18*h* 11*min* 14*s*

Table 5.1. Computation times of actual reconstruction operations (CG-Sense, TGV, IRGN nad IRGN-TGV) for all sequences tested with retrospective undersampling. With nav. TrueFISP naming the navigator-gated TrueFISP, resp. TrueFISP the respiratory-gated TrueFISP and TSE cardiac-gated TSE

Based on the results in table 5.1 and 5.2, it can be said that IRGN-TGV reconstruction takes by far the most computation time, followed by IRGN

Sequence	Preproc.	Postproc.	Walsh est.	H1-est.	Meas.
nav. TrueFISP	48.7*s*	1*min* 33.75*ms*	1*min* 14.56*s*	37*min* 13*s*	5*min* 1*s*
resp. TrueFISP	20.81*s*	33.55*ms*	28.38*s*	10*min* 44*s*	2*min* 15*s*
cerebral PCA	1*min* 36.38*s*	614.1*ms*	1*min* 18.55*s*	10*min* 14*s*	-
renal PCA	1*min* 40.6*s*	367.29*ms*	142.5*s*	32*min* 3*s*	-
cerebral TOF	1*min* 43.4*s*	470*ms*	4*min* 42*s*	1*h* 57*min* 24*s*	-
venous TSE	2*min* 43.5*s*	643.6*ms*	5*min* 18.2*s*	1*h* 14*min* 44*s*	-
arterial TSE	1*min* 28.3*s*	674.6*ms*	6*min* 55.41*s*	1*h* 9*min* 39*s*	-

Table 5.2. Computation times of auxiliary operations (preprocessing, post processing and coil-estimation, Walsh and H1) for all sequences tested with retrospective undersampling. With nav. TrueFISP naming the navigator-gated TrueFISP, resp. TrueFISP the respiratory-gated TrueFISP and TSE cardiac-gated TSE

and TGV. Regarding coil estimation H1-regularization takes much longer time than Walsh estimation or computing the prescan.

5.4 Extended image reconstruction

Based on the results of section 5.2 image reconstruction of cardiac-gated TSE and PCA with a random undersampling pattern and an higher acceleration factor $R = 20$ and $R = 16$ respectively. The reconstruction methods applied are CG-Sense and TGV with ”Walsh”-estimation of the coil sensitivities.

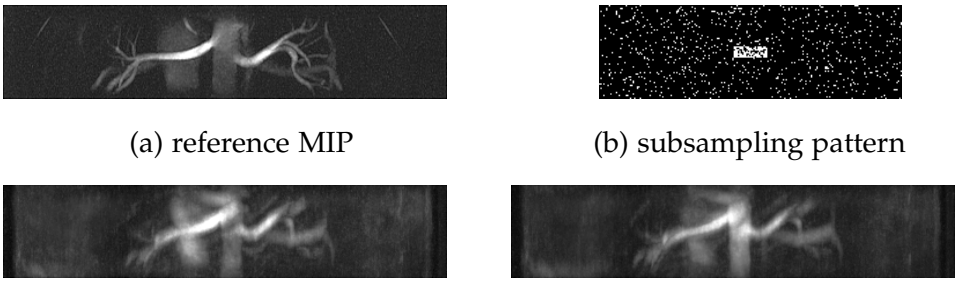

(a) reference MIP (b) subsampling pattern

(c) CG-SENSE using Walsh estimate (d) TGV using Walsh estimate

Figure 5.39. Depiction of CG-Sense and TGV image reconstruction of renal PCA data using a random undersampling pattern, which results in an acceleration factor of $R = 16$. In the top row the initial image on the left and the undersampling pattern used on the right are displayed. The second row shows on the left the CG-Sense reconstruction using a ”Walsh”-estimation of the coil sensitivities and on the right the TGV reconstruction using the same coil estimate.

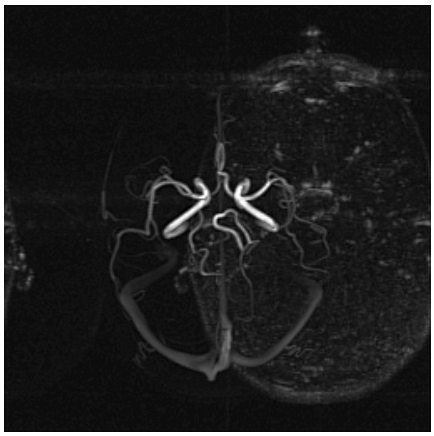

(a) reference MIP

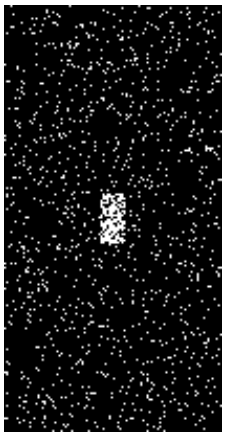

(b) subsampling pattern

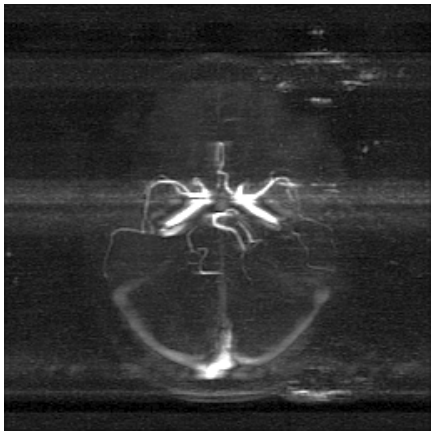

(c) CG-SENSE using Walsh estimate

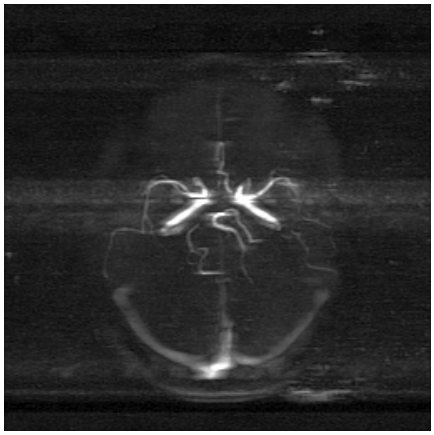

(d) TGV using Walsh estimate

Figure 5.40. Depiction of CG-Sense and TGV image reconstruction of cerebral PCA data using a random undersampling pattern, which results in an acceleration factor of $R = 16$. In the top row the initial image on the left and the undersampling pattern used on the right are displayed. The second row shows on the left the CG-Sense reconstruction using a "Walsh"-estimation of the coil sensitivities and on the right the TGV reconstruction using the same coil estimate.

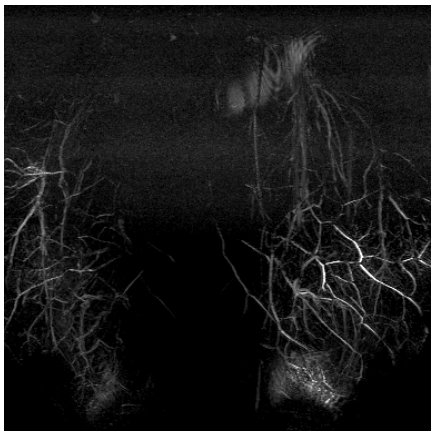

(a) reference MIP

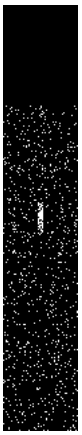

(b) subsampling pattern

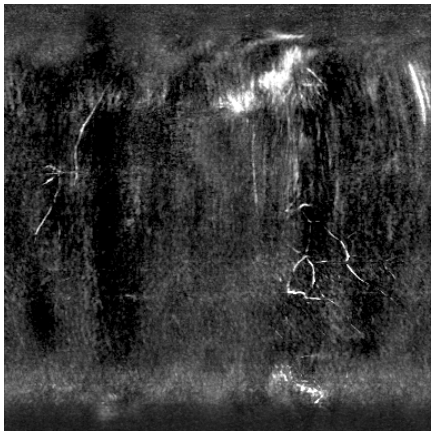

(c) CG-SENSE using Walsh estimate

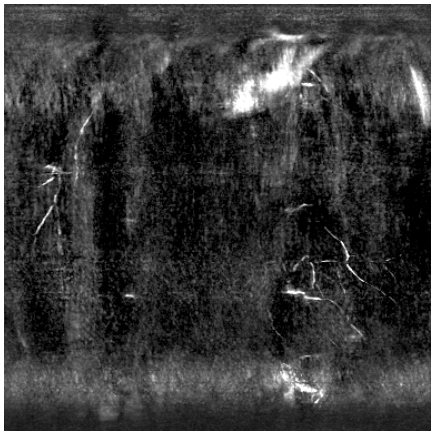

(d) TGV using Walsh estimate

Figure 5.41. Depiction of CG-Sense and TGV image reconstruction of venous phase triggered cardiac-gated TSE data, using a random undersampling pattern, which results in an acceleration factor of $R = 16$. In the top row the initial image on the left and the undersampling pattern used on the right are displayed. The second row shows on the left the CG-Sense reconstruction using a "Walsh"-estimation of the coil sensitivities and on the right the TGV reconstruction using the same coil estimate.

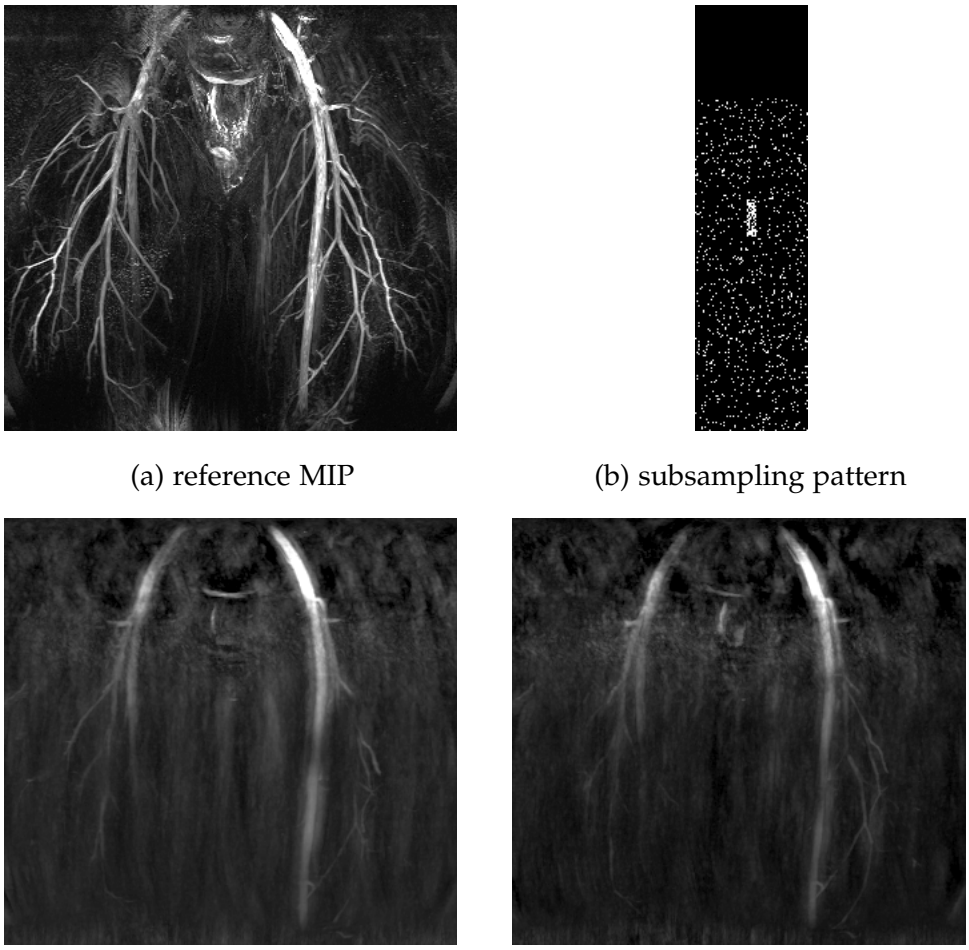

(a) reference MIP (b) subsampling pattern

(c) CG-SENSE using Walsh estimate (d) TGV using Walsh estimate

Figure 5.42. Depiction of CG-Sense and TGV image reconstruction of arterial phase triggered cardiac-gated TSE data, using a random undersampling pattern, which results in an acceleration factor of $R = 16$. In the top row the initial image on the left and the undersampling pattern used on the right are displayed. The second row shows on the left the CG-Sense reconstruction using a "Walsh"-estimation of the coil sensitivities and on the right the TGV reconstruction using the same coil estimate.

6 Discussion

In this section the results presented in chapter 5 are discussed. The first section covers the image acquisition and the second the image reconstruction of retrospective undersampled data.

6.1 Image acquisition

TOF angiography

The results of TOF angiography show good contrast to the background (figure 5.1 and 5.2). There are discontinuities observable which occur as a result of the concatenation of four image slabs to one final image slab.
The results gained are similar to the state-of-the-art as well as the reconstruction results gained on the scanner reconstructed by SIEMENS. In addition, the implemented method for the merge of the overlapping image slabs shows good results, although in literature the end slices are typically discarded and no averaging is performed.

PCA

PCA shows good results for cerebral vessels with proper suppression of the venous signal and background tissue (figure 5.3 and 5.4). On the contrary PCA yields a strong venous overlay for imaging of the carotids , although background suppression is excellent as well. Therefore the carotid images were not part of the retrospective undersampling and image reconstruction. In figure 5.7 and 5.8 the MIPs of renal PCA are shown. In the coronal MIP (figure 5.7) there is a strong overlay of venous blood observable. Figure 5.8 show clear artifacts caused by pulsatile flow in the main artery.
The results obtained are similar to state-of-the-art results as well as offline reconstruction gained a similar outcome compared to on site reconstruction.

Cardiac-gated TSE

Both MIPs, triggered for venous and arterial phase, show a good contrast of the vessels and a good background suppression (figure 5.9 and 5.10). In both images it is observable that the vessels of the left leg constitute more signal than the right leg, due to B_1-inhomogeneities. In addition, a difference between the images in the proximal part is clear caused by the different excitation used for the image, slab-selective in 5.9 and non-selective in 5.10, as described in [7].
The results obtained using offline reconstruction are similar to the on site reconstructed images and are in terms of quality similar to the state-of-the-art.

TrueFISP

The two trigger methods show distinct outcome for renal acquisition, but took about the same acquisition time. The overall transversal MIPs show considerable less signal constitution by the vessels as for the abdominal fat-tissue, although fat-suppression was enabled. The retrospective use of image masks in order to reduce the image to the partial volume containing the vessels is applied to achieve proper fat-suppression (figure 5.11 to 5.16). Although navigator gating (figure 5.11) or respiratory gating (figure 5.16) is used ghosting artifacts are observable in both images.

The depiction of the carotid vessels does not show excellent contrast like PCA of TOF acquisitions and covers a smaller imaging volume. Additionally, background suppression is not good as well. The reason for this is the use of a inversion time which does not match T_1 for the surrounding tissue.

The challenge of this application is, in case of navigator gated TrueFISP, to calibrate the navigator sufficiently. Additionally the use of inversion times longer than one RR-interval results in discarding almost every second image and therefore increases the acquisition time dramatically. In case of respiratory gating the inversion times need to be greater than the RR-interval to capture at least one inflow event. However, due to prolonged T_I-time venous inflow from outside the first inversion slab enters the imaging slab and overlays the arterial signal. Following this protocol has a lot of interconnected parameters and it is challenging to obtain good results.

A solution to this problem may be a change in the protocol setup. Enhanced background suppression could be achieved using the flow-out spin labeling

approach and can further be enhanced using the tag alternation approach. Additionally the original sequence can be improved by determining the best inversion time for every body region applied with a 2D inversion recovery bSSFP. Furthermore a better fat suppression needs to be realized for an improved result. Another option is to set the imaging slab inside the body and compensate with full phase oversampling.
For all sequences are an increased number of artifacts due to patient motion and a change of the physiological signals observable, which results in an alteration of the trigger threshold, due to the long acquisition times.

6.2 Image reconstruction

There were general limitations observed during this work. First, the reconstruction algorithms do not converge for 2D partial Fourier acquisitions preferably used with TSE protocol. However 1D partial Fourier acquisition as well as asymmetric echo acquisition successfully reconstructed. Asymmetric echo acquisition is an optional acquisition parameter available for PCA and TrueFISP protocol and a preset for TOF acquisition. The presented reconstruction pipeline can handle partial Fourier acquisition, however full Fourier acquisition yields the best results. For retrospective undersampling the missing k-space data is filled with zeros in order to avoid retrospective undersampling on already reconstructed data.
All reconstruction algorithms had problems with convergence, when the data reconstructed has an odd number of image samples in one of the image volume dimensions, like phase-encoding direction.

Navigator gated ECG-triggered TrueFISP

Given the results in figures 5.17 and 5.18 the best outcome of image reconstruction of equidistant undersampling is generated using either CG-Sense or TGV with low-resolution prescan or IRGN as method of choice. For the random undersampling pattern the best result was obtained using IRGN, although it lost a considerable amount of information. IRGN-TGV yields for both methods the most insufficient result.

Respiratory gated TrueFISP

The results of respiratory gated TrueFISP show slight improvement compared with navigator gated TrueFISP, but still remain insufficient (figures 5.19 and 5.20). There is no clear best reconstruction method selectable, only IRGN-TGV reconstruction fails completely.

Renal PCA

Given the artifacts of pulsatile motion (figures 5.7 and 5.8), the reconstruction using a separate approach of coil estimation and image reconstruction yield very good results. On the contrary the joint reconstruction approach, using IRGN and IRGN-TGV, yield insufficient results. In comparison of random to equidistant undersampling, reconstruction from random undersampling yields improved resolution of the small vessels (see 5.21 and 5.22).

Cerebral PCA

The results of cerebral PCA image reconstruction, shown in figures 5.23 to 5.26, indicate good outcome. For equidistant undersampling back folding artifacts are observable, with the least impact for IRGN and IRGN-TGV reconstruction (see figures 5.23 and 5.24). Random subsampling removes back folding artifacts entirely. The best small vessel resolution and background suppression are achieved with a separated coil estimation approach. In addition TGV yields minor improved results compared to CG-Sense, regardless of the chosen coil estimation method (see figures 5.25 and 5.26).

Cerebral TOF

The results of image reconstruction for cerebral TOF are shown in figures 5.27 to 5.30. Reconstruction with random undersampling pattern resulted in an insufficient outcome for all tested reconstruction methods regardless if the joint approach was used or not (see figures 5.29 and 5.30). However, for equidistant undersampling the joint approach IRGN yields the best outcome but compared with the initial result a strong difference is apparent. This is most likely caused by asymmetric echo acquisition inherently enabled in the TOF protocol.

Venous phase cardiac-gated TSE

Venous phase cardiac-gated TSE with equidistant undersampling pattern has the same problem with back folding artifacts like PCA in the image

reconstruction with separately estimated coil-sensitivities. The joint reconstruction approach IRGN can reconstruct the image properly, though a decreased background suppression is observable. IRGN-TGV does not yield a proper image quality (see figures 5.31 and 5.32). The application of random undersampling pattern yields no back folding artifacts in the final images and a image comparable quality with the initial image, using any reconstruction approach with separately estimated coil-sensitivities. The IRGN appraoch yields a proper result for the vessels but exhibits increased noise in the proximal part of the image. IRGN-TGV yields no proper result (see figures 5.33 and 5.34).

Arterial phase cardiac-gated TSE

The results for equidistant undersampled image reconstruction show no back folding artifacts in all reconstructed images (see figures 5.35 and 5.36), in contrast to the venous phase image. CG-Sense and TGV exhibits good results with a good depiction of small vessels. IRGN reconstruction show considerable enhanced noise and IRGN-TGV yield no proper result at all. The reconstructed image from randomly undersampled initial data show better results, compared to equidistant undersampling. Additionally TGV based reconstruction yields the best result regardless of the coil estimation method. IRGN shows similar noisy figures like in equidistant undersampled data and IRGN-TGV depicts another insufficient outcome.

Conclusion

The sequence protocols tested yield good results for the well established PCA and TOF methods, as well as for the cardiac-gated TSE. As described earlier optimization of the TrueFISP protocol required longer training to gain data that was usable for the retrospective undersampling and reconstruction. Further proposed adjustments should yield enhanced quality.
Comparing the undersampling pattern applied, random sampling yielded better results in all test cases than the equidistant pattern and is therefore favorable to be used, which is also consistent with compressed sensing theory as the aliasing artifacts are more incoherently distributed.
In this work all sequences were adjusted to sample the full k-space to compare fully and retrospectively undersampled data. This was (partly) overcome by repeated measurements and patient training. A comparison with undersampled data acquired was not performed.
Given the results of CG-Sense image reconstruction with coil estimation proposed by Walsh et al. [20] as state-of-the-art method of accelerated reconstruction, TGV yields similar results but no obvious differences regardless of the estimation method, as well as IRGN. Only the results of IRGN-TGV were in almost all tested applications of insufficient reconstruction quality compared to all other methods and therefore is not applicable for the given problem (Cartesian sampling pattern). In contrast to the classical Sense approach, which struggles with acceleration factors grater three, CG-Sense and TGV obtain good results for an acceleration factor of $R = 16$ applied to PCA data (figures 5.39 and 5.40). The reconstruction results for cardiac-gated

TSE are, in the case of venous phase triggered, insufficient for arterial phase triggered still acceptable. The acceleration factor for cardiac-gated TSE was $R = 20$ due to the inherent partial Fourier acquisition.
Additionally it can be observed that the resulting angiograms of difference approach (cardiac-gated TSE and PCA) yields by far a better outcome than protocols relying on sequence contrast.
In all tested sampling pattern the choice of coil estimation method was of minor importance since no preferable method was observable in all experiments performed.
All tested reconstruction methods were able to reconstruct data with partial Fourier acquisition and one the of two proposed undersampling pattern. The combination of partial Fourier acquisition with one of the proposed sampling pattern yielded in less sufficient outcome than with the pattern used solely.

6.3 Limitations of this work

This section covers the restrictions under which this work was performed.

1. There were only four types of sequence protocols used (PCA, TOF, cardiac-gated TSE and TrueFISP). However there is a promising protocol described in section 2.2 named flow-sensitive-dephasing. The exemplary work and results are given in [36].
2. The acquisition pattern for all acquisitions on site were Cartesian. In [15] it was shown that TGV and IRGN-TGV yield excellent results

with radial sampling pattern.

3. This work focused on image reconstruction and no accelerated acquisitions on a scanner were performed and protocols developed by SIEMENS were used.
4. The reconstruction pipeline was only implemented in MATLAB but for clinical application the reconstruction times need to be drastically decreased, for example with implementation on graphics hardware using CUDA.

Future work

1. Implement the reconstruction pipeline in graphics card hardware CUDA
2. Perform measurements using the sampling pattern tested
3. Adapt the sampling trajectories to radial or stack-of-stars
4. Enhance fat-suppression on the TrueFISP sequence with sequence adaption
5. Perform scans without partial Fourier or asymmetric echo acquisition
6. Test for higher acceleration factors

Bibliography

[1] Griswold MA, Jakob PM, Heidemann RM, Nittka M, Jellus V, Wang J, Kiefer B, and Haase A. "Generalized autocalibrating partially parallel acquisitions (GRAPPA)." Magn. Reson. Med. 2002; 47(6): 1202–1210.

[2] Pruessmann KP, Weiger M, Börnert P, and Boesiger P. "Advances in sensitivity encoding with arbitrary k-space trajectories." Magn. Reson. Med. 2001; 46(4): 638–651.

[3] Bredies K, Kunisch K, and Pock T. "Total Generalized Variation." SIAM J. Imaging Sci. 2010; 3(3): 492–526.

[4] Knoll F, Clason C, Bredies K, Uecker M, and Stollberger R. "Parallel imaging with nonlinear reconstruction using variational penalties." Magn. Reson. Med. 2012; 67(1): 34–41.

[5] Bernstein MA, King KF, and Zhou XJ. *Handbook of MRI Pulse Sequences*. Elsevier, 2004. 1042 pp.

[6] Haacke EM, Brown RW, Thompson MR, and Venkatesan R. *Magnetic resonance imaging - principles and sequence design*. 1999.

[7] Wheaton AJ and Miyazaki M. "Non-contrast enhanced MR angiography: Physical principles." J. Magn. Reson. Imaging 2012; 36(2): 286–304.

[8] Miyazaki M, Sugiura S, Tateishi F, Wada H, Kassai Y, and Abe H. "Non-contrast-enhanced MR angiography using 3D ECG-synchronized half-Fourier fast spin echo." J. Magn. Reson. Imaging 2000; 12(5): 776–783.

[9] Nakamura K, Miyazaki M, Kuroki K, Yamamoto A, Hiramine A, and Admiraal-Behloul F. "Noncontrast-enhanced peripheral MRA: Technical optimization of flow-spoiled fresh blood imaging for screening peripheral arterial diseases." Magn. Reson. Med. 2011; 65(2): 595–602.

[10] Storey P, Atanasova IP, Lim RP, Xu J, Kim D, Chen Q, and Lee VS. "Tailoring the flow sensitivity of fast spin-echo sequences for noncontrast peripheral MR angiography." Magn. Reson. Med. 2010; 64(4): 1098–1108.

[11] Oktar SO, Yücel C, Karaosmanoglu D, Akkan K, Ozdemir H, Tokgoz N, and Tali T. "Blood-Flow Volume Quantification in Internal Carotid and Vertebral Arteries: Comparison of 3 Different Ultrasound Techniques with Phase-Contrast MR Imaging." AJNR Am J Neuroradiol 2006; 27(2): 363–369.

[12] Kumano Y, Ishii M, Nishida H, Sakamoto M, Sasaki K, Kawauchi A, and Mitamura K. "Measurement of renal arterial blood flow velocity by Doppler ultrasonography in chronic liver disease." Hepatology Research 1999; 15(3): 201–214.

[13] Fronek A, Coel M, and Berstein EF. "Quantitative ultrasonographic studies of lower extremity flow velocities in health and disease." Circulation 1976; 53(6): 957–960.

[14] Pérez Riera AR, Ferreira C, Filho CR, Ferreira M, Meneghini A, Uchida A, Schapachnik E, Dubner S, and Zhang L. "The enigmatic sixth wave of the electrocardiogram: the U wave." Cardiol J 2007; 15(5): 408–421.

[15] Knoll F. "Constrained MR Image Reconstruction of Undersampled Data from Multiple Coils." dissertation. Institute of Medical Engineering, Graz University of Technology, 2011.

[16] "Nuclear magnetic resonance (NMR) imaging with multiple surface coils." US4825162 A. Roemer B and Edelstein WA. U.S. Classification 324/318, 324/312; International Classification G01R33/3415; Cooperative Classification G01R33/3415; European Classification G01R33/3415. 1989.

[17] Sodickson DK and Manning WJ. "Simultaneous acquisition of spatial harmonics (SMASH): Fast imaging with radiofrequency coil arrays." Magn. Reson. Med. 1997; 38(4): 591–603.

[18] Pruessmann KP, Weiger M, Scheidegger MB, and Boesiger P. "SENSE: sensitivity encoding for fast MRI." 1999.

[19] Bydder M, Larkman D, and Hajnal J. "Combination of signals from array coils using image-based estimation of coil sensitivity profiles." Magn. Reson. Med. 2002; 47(3): 539–548.

[20] Walsh DO, Gmitro AF, and Marcellin MW. "Adaptive reconstruction of phased array MR imagery." Magn. Reson. Med. 2000; 43(5): 682–690.

[21] Weiger M, Pruessmann KP, and Boesiger P. "2D sense for faster 3D MRI." MAGMA 2002; 14(1): 10–19.

[22] Blaimer M, Breuer FA, Mueller M, Seiberlich N, Ebel D, Heidemann RM, Griswold MA, and Jakob PM. "2D-GRAPPA-operator for faster 3D parallel MRI." Magn. Reson. Med. 2006; 56(6): 1359–1364.

[23] Wang J, Kluge T, Nittka M, Jellus V, Kuehn B, and Kiefer B. "Parallel acquisition techniques with modified SENSE reconstruction mSENSE." Proceedings of the First Wurzburg Workshop on Parallel Imaging 2001; 29.

[24] Margosian P, Schmitt F, and Purdy D. "Faster MR imaging: imaging with half the data." 1986; 1(6): 195–197.

[25] Knoll F, Bredies K, Pock T, and Stollberger R. "Second order total generalized variation (TGV) for MRI." Magn. Reson. Med. 2011; 65(2): 480–491.

[26] Chambolle A and Pock T. "A First-Order Primal-Dual Algorithm for Convex Problems with Applications to Imaging." J Math Imaging Vis 2010; 40(1): 120–145.

[27] Bauer F and Kannengiesser S. "An alternative approach to the image reconstruction for parallel data acquisition in MRI." Math. Meth. Appl. Sci. 2007; 30(12): 1437–1451.

[28] Uecker M, Hohage T, Block KT, and Frahm J. "Image reconstruction by regularized nonlinear inversion—Joint estimation of coil sensitivities and image content." Magn. Reson. Med. 2008; 60(3): 674–682.

[29] Uecker M, Karaus A, and Frahm J. "Inverse reconstruction method for segmented multishot diffusion-weighted MRI with multiple coils." Magn. Reson. Med. 2009; 62(5): 1342–1348.

[30] Siemens. *syngo MR D13 Gebrauchsanweisung - Vascular*. 2010.

[31] Rick M, Kaarman N, Weale P, and Schmitt P. "How I do it: Non Contrast-Enhanced MR Angiography (syngo NATIVE)." MAGNETOM Flash 2009.

[32] Deng J, Messina M, McNeal G, Bi X, Reilly B, Bero S, Giri S, and Rigsby CK. "How I do it: Renal Non-Enhanced MR Angiography (syngo NATIVE TrueFISP) in Pediatric Patients." MAGNETOM Flash 2014.

[33] Atanasova IP, Lim RP, Guo H, Kim D, Storey P. McGortey K, Laine A, and Lee VS. "Non-contrast inversion recovery balacend SSFP MRA of the abdominal aorta at 3T: Predicting optimal inversion times by blood velocity measurement." Proc. Intl. Soc. Mag. Reson. Med 2010.

[34] *MRI Partial Fourier reconstruction with POCS*. 2012. URL: `http://de.mathworks.com/matlabcentral/fileexchange/39350-mri-partial-fourier-reconstruction-with-pocs`.

[35] *mapVBVD - Reading data from SIEMENS rawdata files*. 2014. URL: `www.mr-idea.com`.

[36] Fan Z, Saouaf R, Liu X, Bi X, and Li D. "Non-Contrast MR Angiography: Flow-Sensitive Dephasing (FSD)-Prepared 3D Balanced SSFP." MAGNETOM Flash 2013-03; 53: 2–7.